

INFORMATION TO USERS

This reproduction was made from a copy of a document sent to us for microfilming. While the most advanced technology has been used to photograph and reproduce this document, the quality of the reproduction is heavily dependent upon the quality of the material submitted.

The following explanation of techniques is provided to help clarify markings or notations which may appear on this reproduction.

1. The sign or "target" for pages apparently lacking from the document photographed is "Missing Page(s)". If it was possible to obtain the missing page(s) or section, they are spliced into the film along with adjacent pages. This may have necessitated cutting through an image and duplicating adjacent pages to assure complete continuity.
2. When an image on the film is obliterated with a round black mark, it is an indication of either blurred copy because of movement during exposure, duplicate copy, or copyrighted materials that should not have been filmed. For blurred pages, a good image of the page can be found in the adjacent frame. If copyrighted materials were deleted, a target note will appear listing the pages in the adjacent frame.
3. When a map, drawing or chart, etc., is part of the material being photographed, a definite method of "sectioning" the material has been followed. It is customary to begin filming at the upper left hand corner of a large sheet and to continue from left to right in equal sections with small overlaps. If necessary, sectioning is continued again—beginning below the first row and continuing on until complete.
4. For illustrations that cannot be satisfactorily reproduced by xerographic means, photographic prints can be purchased at additional cost and inserted into your xerographic copy. These prints are available upon request from the Dissertations Customer Services Department.
5. Some pages in any document may have indistinct print. In all cases the best available copy has been filmed.

**University
Microfilms
International**

300 N. Zeeb Road
Ann Arbor, MI 48106



Order Number 1332466

Sensor modeling and image restoration for a CCD pushbroom imager

Li, Wai-Mo, M.S.

The University of Arizona, 1987

U·M·I
300 N. Zeeb Rd.
Ann Arbor, MI 48106



PLEASE NOTE:

In all cases this material has been filmed in the best possible way from the available copy. Problems encountered with this document have been identified here with a check mark .

1. Glossy photographs or pages _____
2. Colored illustrations, paper or print _____
3. Photographs with dark background _____
4. Illustrations are poor copy _____
5. Pages with black marks, not original copy _____
6. Print shows through as there is text on both sides of page _____
7. Indistinct, broken or small print on several pages _____
8. Print exceeds margin requirements _____
9. Tightly bound copy with print lost in spine _____
10. Computer printout pages with indistinct print _____
11. Page(s) _____ lacking when material received, and not available from school or author.
12. Page(s) _____ seem to be missing in numbering only as text follows.
13. Two pages numbered _____. Text follows.
14. Curling and wrinkled pages _____
15. Dissertation contains pages with print at a slant, filmed as received _____
16. Other _____

U·M·I



SENSOR MODELING AND IMAGE RESTORATION
FOR A CCD PUSHBROOM IMAGER

by

Wai-Mo Li

A Thesis Submitted to the Faculty of the
DEPARTMENT OF ELECTRICAL AND COMPUTER ENGINEERING
In Partial Fulfillment of the Requirements
For the Degree of
MASTER OF SCIENCE
WITH A MAJOR IN ELECTRICAL ENGINEERING

In the Graduate College

THE UNIVERSITY OF ARIZONA

1 9 8 7

STATEMENT BY AUTHOR

This thesis has been submitted in partial fulfillment of requirements for an advanced degree at The University of Arizona and is deposited in the University Library to be made available to borrowers under rules of the Library.

Brief quotations from this thesis are allowable without special permission, provided that accurate acknowledgement of source is made. Requests for permission for extended quotation from or reproduction of this manuscript in whole or in part may be granted by the head of the department or the Dean of the Graduate College when in his or her judgement the proposed use of the material is in the interests of scholarship. In all other instances, however, permission must be obtained from the author.

SIGNED: Li Wai Ho

APPROVAL BY THESIS DIRECTOR

This thesis has been approved on the date shown below:

R. A. Schowengerdt
R. A. Schowengerdt
Associate Professor Office of
Arid Lands Studies, Electrical
& Computer Engineering, Optical
Sciences

12/8/87
Date

ACKNOWLEDGEMENT

This thesis was written to cover the research in my graduate work. I would like to thank the U.S. Geological Survey, EROS Data Center for supporting my research. More importantly, I gratefully acknowledge my thesis and research advisor Dr. Robert Schowengerdt, whose guidance, comments and suggestions were invaluable. In addition, I like to express my gratitude to Dr. Robert Schowengerdt for reading my initial portions of the manuscript and making many helpful suggestions regarding organization and terminology. Without his patience and assistance, this thesis would not have reached the final draft.

TABLE OF CONTENTS

	page
LIST OF ILLUSTRATIONS.....	vii
LIST OF TABLES.....	xi
ABSTRACT.....	xii
CHAPTER	
1. INTRODUCTION.....	1
2. CHARGE-COUPLED DEVICES	6
2.1 Description of Basic Linear Array CCD Operation.....	7
2.1.1 Buried-channel CCD.....	9
2.2 Optical Imaging with Charge- Coupled Devices.....	11
2.2.1 Principles of CCD imaging.....	11
2.2.2 Basic properties of CCD image sensors.....	14
2.3 Analysis of Noise in CCD Devices.....	16
2.4 Charge Transfer Efficiency.....	19
2.5 Derivation of MTF and PTF for a CCD.....	23
2.5.1 Frequency domain approach.....	23
2.5.2 Spatial domain approach.....	27
3. THE SPOT SATELLITE SYSTEM AND SYSTEM MODELING.....	32
3.1 General Description of SPOT System.....	33
3.1.1 HRV detection unit.....	35
3.1.2 The SPOT CCD system.....	37
3.2 SPOT Image Formation System.....	38
3.2.1 Imaging subsystem.....	38

TABLE OF CONTENTS--(continued)

3.3	SPOT Modeling.....	41
3.3.1	Image forming optics.....	43
3.3.2	Scanning aperture.....	44
3.3.3	Electronic filters	46
3.3.4	Sampling integration.....	48
3.4	Panchromatic Band Model.....	51
3.5	Multispectral Band Model.....	51
4.	IMAGE SAMPLING AND RESTORATION.....	67
4.1	Image Sampling and Restoration Systems.....	67
4.1.1	Sampling subsystem.....	67
4.1.2	Restoration subsystem.....	68
4.2	The Linear Inverse and Wiener Filters.....	68
4.2.1	Scene autocorrelation model.....	74
4.2.2	Noise power spectrum.....	75
4.3	The effect of sampling.....	76
4.4	Restoration kernel window.....	78
5.	SYSTEM PERFORMANCE TESTING.....	81
5.1	Frequency Increment and Sampling Interval.....	81
5.2	Autocorrelation and Power Spectrum of scene.....	83
5.2.1	Measurement of the autocorrelation function.....	86
5.2.2	Effects of parameters on Wiener filter equation.....	89
5.3	Windowing.....	92
5.4	Edge Simulation and Resampling.....	96
5.5	Image Testing.....	111
6.	SUMMARY AND CONCLUSIONS.....	119
APPENDIX A:	MTF AND PTF DERIVATIONS OF CCD IN FREQUENCY DOMAIN.....	123

TABLE OF CONTENTS--(continued)

APPENDIX B: MTF AND PTF DERIVATIONS OF CCD IN SPATIAL DOMAIN.....	125
REFERENCES.....	127

LIST OF ILLUSTRATIONS

Figure	page
2.1 Three-phase CCD.....	8
2.2 Basic principles of CCD imaging.....	13
2.3 Noise sources in a system using a CCD.....	17
2.4 Equivalent circuit of input of charge to a potential well.....	17
2.5 MTF and PTF versus relative frequency response for various amounts of loss.....	24
2.6 Schematic representative of three- phase charge-transfer shift registers.....	28
2.7 Illustration of an n-stage register.....	28
3.1 Nadir viewing of SPOT.....	34
3.2 Sensor scanning methods.....	36
3.3 Description with explicit sample- scene phase (u,v).....	39
3.4 Optics MTFs of different systems.....	45
3.5 IFOV MTFs of different systems.....	47
3.6 Electronic MTFs of different systems.....	49
3.7 Electronic PTFs of different systems.....	50

LIST OF ILLUSTRATIONS--(continued)

3.8	Separate components in along-track direction.....	52
3.9	Separate components in across-track direction.....	53
3.10	System line spread function of SPOT in along-track direction.....	54
3.11	System line spread function of SPOT in across-track direction.....	55
3.12	Different dimensions of IFOV and optics between Panchomatic and Multispectral bands.....	57
3.13	Overall system TF in band 1 (across-track direction).....	58
3.14	Overall system TF in band 2 (across-track direction).....	59
3.15	Overall system TF in band 3 (across-track direction).....	60
3.16	Overall system TF in band 1 (along-track direction).....	61
3.17	Overall system TF in band 2 (along-track direction).....	62
3.18	Overall system TF in band 3 (along-track direction).....	63
3.19	Overall system TFs for different systems (across-track direction).....	65
3.20	Overall system TFs for different systems (along-track direction).....	66
4.1	A 2-D comb function.....	69
5.1	The SLSF (Pan, along-track direction).....	84

LIST OF ILLUSTRATIONS--(continued)

5.2	Illustration of the relationship between sampling interval and frequency increment of a signal.....	85
5.3	The autocorrelation function of a SPOT image (Phoenix).....	88
5.4	The autocorrelation function of SLSF (Pan, across-track direction).....	90
5.5	The changes of restoration TF caused by the variations of scene variance	93
5.6	The changes of restoration TF caused by the variations of autocorrelation half-width.....	94
5.7	The RLSF (Pan, along-track direction) without windowing.....	95
5.8	The restoration TF with windowing (Pan, across-track direction).....	97
5.9	The procedure for image simulation.....	100
5.10	The original scene of size 1X1024, edge at center.....	101
5.11	The SLSF (Pan, along-track direction).....	103
5.12	The processed image with size 1X896.....	104
5.13	The correction of a distorted image by an interpolation function $r(x,y)$	105
5.14	The bilinear and bicubic resampling functions.....	106

LIST OF ILLUSTRATION--(continued)

- 5.15 The resampled edge by using the
resampling function PCC ($\alpha=-1$).....107
- 5.16 The changes of the MSE by varying
alpha in PCC.....109
- 5.17 The changes of the MSE by using
different resampling functions.....110
- 5.18 The edge response of different
resampling functions.....112
- 5.19 Display the first case result.....114
- 5.20 The result from the first case
is averaged within
0.5 cycle/pixel.....115
- 5.21 The result from the second case
is averaged within
0.5 cycle/pixel.....116
- 5.22 The result from the third case
is averaged within
0.5 cycle/pixel.....117

LIST OF TABLES

Table	page
2.1 Advantages and disadvantages of BCCD relative to SCCD.....	12
2.2 Expressions for noise sources associated with focal-plane arrays.....	20
2.3 Principal noise sources in a typical CCD image sensor.....	21
5.1 The variations of the autocorrelation HW across a SPOT image (Phoenix).....	91
5.2 The changes in power of the restoration TF by varying the kernel size of window.....	98

ABSTRACT

Following the development of detector technology, remote sensing image detection is being implemented with charge-coupled devices (CCD), which have promising features. The French SPOT system is the first civilian satellite sensor employing a CCD in its detection unit. In order to obtain the system transfer function (TF), a linear system model is developed in the across- and along-track directions.

The overall system TF, including pixel sampling effects, is then used in the Wiener filter function to derive an optimal restoration function. A restoration line spread function (RLSF) is obtained by the inverse Fourier transform of the Wiener filter and multiplied with a window function.

Simulation and empirical tests are described comparing the RLSF to standard kernels used for image resampling for geometric correction. The RLSF results in superior edge enhancement as expected.

CHAPTER 1

INTRODUCTION

With the advent of electronic technology, a new kind of detector has been introduced for remote sensing in recent years. This new type of detector is a charge-coupled device (CCD) implemented in a linear array, acting as an analog shift register. CCDs may be used as a memory devices, a function that has been employed to store data in computers. The operation of CCDs in imaging utilizes the flow of charge along the shift registers. Initially, charge packets are generated by absorption of photons, and then flow along the registers by manipulation of potential wells above each register at appropriate clocking, and finally to the output via an amplifier.

This kind of technique for image generation is called "push-broom" scanning as adopted in the SPOT satellite system, a project designed and planned by France in cooperation with two European countries (Belgium and Sweden). In comparison, the Landsat series systems, like

the multispectral spectral scanner (MSS) and thematic mapper (TM), as well as the advanced very high resolution radiometer (AVHRR), use another technique called "whisk-broom" scanning to generate images. A "whisk-broom" sensor scans a detector orthogonal to the orbit direction, and has limited resolution because of limited integration time resulting from required high scan speeds.

The advantages of "pushbroom" array CCD detectors for remote sensing imaging are light weight, small size, less power consumption, high signal-to-noise ratio, and precise geometrical characteristics. In Chapter 2, we discuss the basic operation of a linear array CCD, such as the one in the SPOT system. The factors that define the performance of CCDs as image sensors, resolution, sensitivity and dynamic range, are discussed in detail. When discussing the performance of a detector, noise must be taken into account. Thus, in Chapter 2, different sources of noise are explained briefly and typical values of noises occurring in CCD detectors are tabulated. Lastly, the CCD transfer function (TF) is derived by two approaches.

After discussing CCD operation and characteristics in Chapter 2, we concentrate on how to model a CCD system.

The SPOT system has certain special features that differentiate it from the other satellite systems such as MSS, TM, or AVHRR. In Chapter 3, general information on the SPOT system is presented, specifically the detection unit high resolution visible (HRV) instrument, which can image in multispectral or panchromatic modes. Lastly, the Fairchild CCD 122H used in SPOT-1 is discussed.

The next topic is the modeling program, which has been used previously to model the Landsat and AVHRR systems. In the across-track direction (orthogonal to the direction of orbit), the SPOT system model includes several components: optics TF, instantaneous field of view (IFOV) and electronic filter TF. In the along-track direction (the satellite orbit), we have the following components: optics TF, IFOV and integration time TF. These factors resemble the components of the Landsat and AVHRR systems but occur in different directions relative to the satellite track. The system model results in transfer functions for each band in both along- and across-track directions.

In Chapter 4, two topics are covered, image sampling and restoration. Image sampling included in the modeling results in a more degraded system than we would normally have. The image restoration filter that we

employ is the Wiener filter, which minimizes the mean square error between the restored and original scene. Even though the system includes the sampling component, making the whole system more degraded, it is treated as a linear effect and the Wiener filter can partially restore the image towards the original scene.

Given the system transfer function and Wiener filter in the frequency domain, the line spread function (LSF) of each may be obtained by an inverse Fourier transform. In image processing, the impulse response of the linear system to a point source is the point spread function (PSF) and the impulse response to a line source is the line spread function (LSF). Before the restoration line spread function (RLSF) is applied to a degraded image, a window is used to shape the high oscillation components. The window function and its parameters are discussed at the end of Chapter 4 and in Chapter 5.

Chapter 5 discusses several parameters that affect the overall system performance and covers testing that is relevant to our system modeling. They are: the choice of frequency or spatial increment, the effect on the Wiener filter by a change of parameters, the derivation of the optimal parameters used in the RLSF window, and the verification of the restoration TF by image testing.

Finally, a summary and conclusions are presented in Chapter 6. The major conclusions are that the SPOT system can be successfully modeled with linear system components and an effective RLSF can be derived for enhancing SPOT imagery.

Chapter 2

CHARGE-COUPLED DEVICES

When considering the space applications of any imaging instrument, device reliability, weight, size and power consumption are of primary importance. In all these respects, photosensitive charge-coupled device (CCD) sensors are superior to electron tube-type imaging instruments and, in fact, to almost any other type of imaging instrument suitable for remote sensing applications.

The major advantage of the charge transfer principle as applied to image sensing is that all charge packets can be detected at a single small output, while electrodes are still pulsed to transfer charge packets to the output. Increased signal-to-noise ratio is the result because of increased integration time available. In addition, CCDs have a wide spectral range, and precise geometrical characteristics. Among the photosensitive CCDs available today, linear-arrays are especially suitable for observation of the earth from orbit. In this chapter, linear-array CCDs are discussed in detail.

2.1 Description of Basic Linear Array CCD Operation

Basically, a charge-coupled device is a metal-oxide-semiconductor (MOS) structure (Fig.2.1) which can collect and store minority-carrier charge packets in localized potential wells at the Si-SiO₂ interface. The CCD can transfer charge packets in discrete-time increments via the controlled movement of potential wells. The charge packets can then be detected at the output via capacitive coupling. Thus, a CCD acts as an analog shift register composed of three sections: (1) The input section contains a source of minority carriers whose potential can be controlled, and an input gate to control the flow of charge from the source diffusion into the first potential. (2) The transfer section contains a series of electrodes that control the potential at the Si-SiO₂ interface. When the voltages on the electrodes are properly manipulated, the potential wells are moved towards the output, and the charge packets follow. (3) The output section is a reverse biased p-n junction capacitance whose voltage is changed when a charge packet arrives. The diode is then reset via a switch to prepare for the next packet to be transferred. This node is typically connected to a MOS amplifier.

As an imager, scene information is entered into the

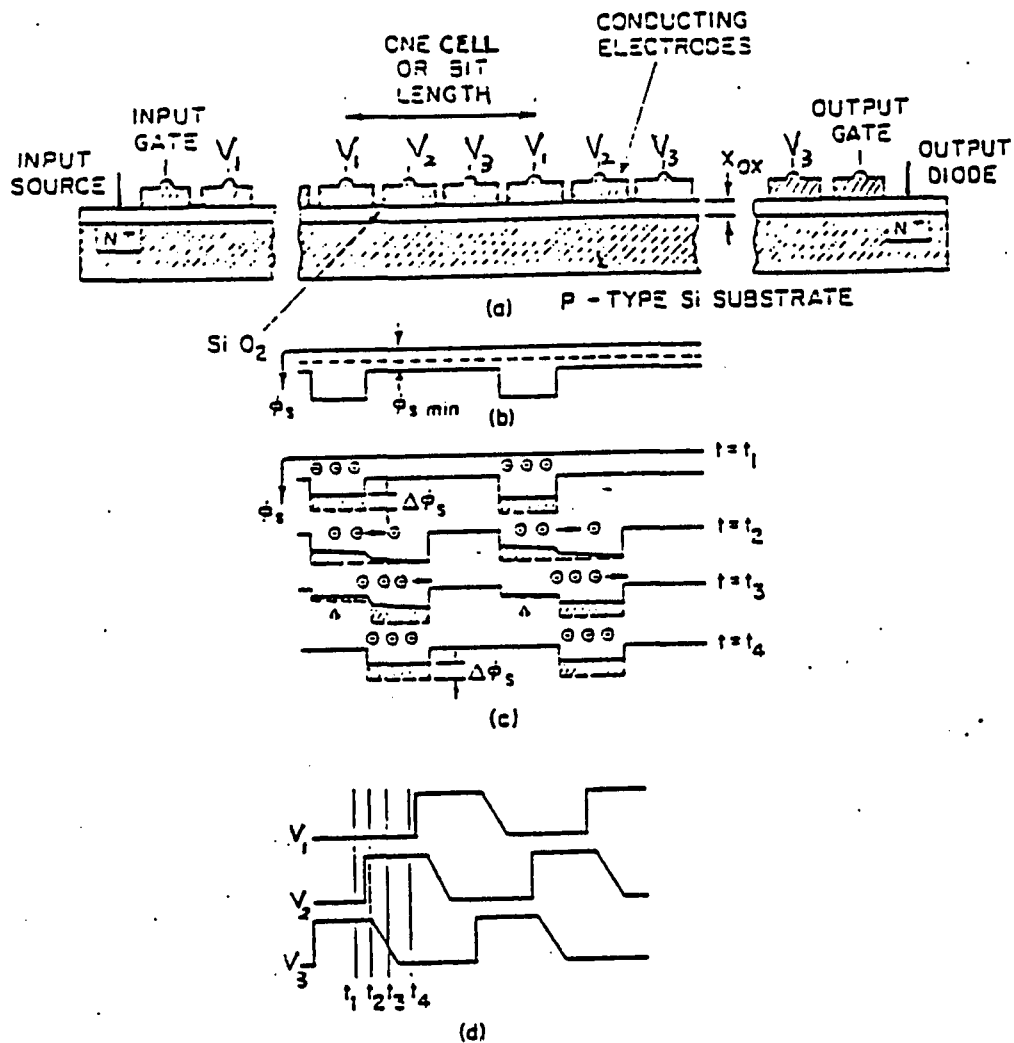


Fig.2.1 Three-phase CCD. (a) Cross-sectional view showing input section, transfer section, and output section. A primitive electrode structure having unprotected gaps is shown for simplicity. (b) Surface-potential profile showing potential wells under the electrodes. (c) Surface-potential profiles showing progression of charge transfer during one clock period. (d) Clocking waveforms used to drive the CCD during transfer.

device via the absorption of photons at the source location. Suppose that a charge configuration representing scene information has been collected in the device as shown in Fig.2.1.c. In a device having a planar oxide and uniform substrate doping, three phases are required for unidirectional charge transfer, i.e., if a barrier is maintained behind the charge packet while a deeper well is formed in front of the packet, then charge will flow into the deeper well. The clocking diagram is shown in Fig.2.1.d. At $t = t_1$, charge resides in the wells under the V_1 electrodes. At $t = t_2$, the potential on V_2 is made positive, forming wells under the V_2 electrodes. Charge will then flow from the V_1 wells into the V_2 wells. At $t = t_3$, the potential on the V_1 electrodes is reduced to a low value and the remaining charge in the V_1 wells will be pushed into the V_2 wells. This sequence repeats with the result that the charge configuration moves from one cell to the next every clock period.

2.1.1 Buried-channel CCD

Two kinds of CCDs are produced. In surface channel CCDs (SCCDs), charge packets are stored very close to the interface between the semiconductor and the overlying insulator. In the other type, bulk or buried CCDs (BCCDs), the charge packets are stored some distance away

from the surface of the semiconductor. The CCD used in the SPOT HRV is of the monolithic linear focal plane buried-channel type. In this section we discuss its characteristics and implementations.

BCCD performance is significantly different from that of a SCCD. First, due to the charge residing further away from the gate than in surface channel devices, the charge carrying capability of the BCCD is less than that of the SCCD. Second, as the charge packet size is increased, the charge distribution spreads mainly toward the semiconductor surface; thus to produce a BCCD with maximum signal handling capability, a steeply graded doping profile near the semiconductor surface is required to prevent the charge coming into contact with the surface. On the other hand, for high-speed applications a strong fringing dielectric field between adjacent electrodes is desirable to aid the transfer of charge from one potential well to the next; this occurs when the channel is located deeper in the bulk. The problem of surface state trapping does not, of course, occur with bulk channel devices (because the signal charge is held away from the Si/SiO₂ interface) and this is one of their major advantages over surface channel devices. However, BCCDs do show trapping effects due to bulk traps. A summary comparison between BCCDs and SCCDs is presented

in Table 2.1.

In addition, two fabrication and packaging technologies are employed to produce CCD arrays, monolithic and hybrid focal plane. A monolithic focal plane is one in which the detector and the CCD are in the same chip. In the hybrid focal plane, photosensing is done with one material (chip) and the CCD readout is done with another chip, normally silicon.

2.2 Optical Imaging with Charge-Coupled Devices (CCDs)

This section describes the design, operation and performance parameters of charged-coupled imaging devices.

2.2.1 Principles of CCD imaging

As an optical imaging device, the CCD analog shift register may be used to collect and read out optically generated signals. The basic structure is illustrated in Fig.2.2 for an n-channel array. An optical system focuses an image (depicted as a single light spot in this case) on the front face of the CCD. Initially, V_1 , is held at a positive clock voltage, thus creating a potential well under each of these electrodes; the other electrodes are held at zero volts or a small resting potential. Photons entering the silicon substrate, either through or between

Table 2.1 Advantages and disadvantages of a BCCD relative to a SCCD

BCCD Advantages

Higher transfer efficiency

Higher frequency operation

Lower intrinsic noise

BCCD Disadvantages

More complex technology

Smaller charge handling capability

More sensitive to thermal generation

Poor linearity

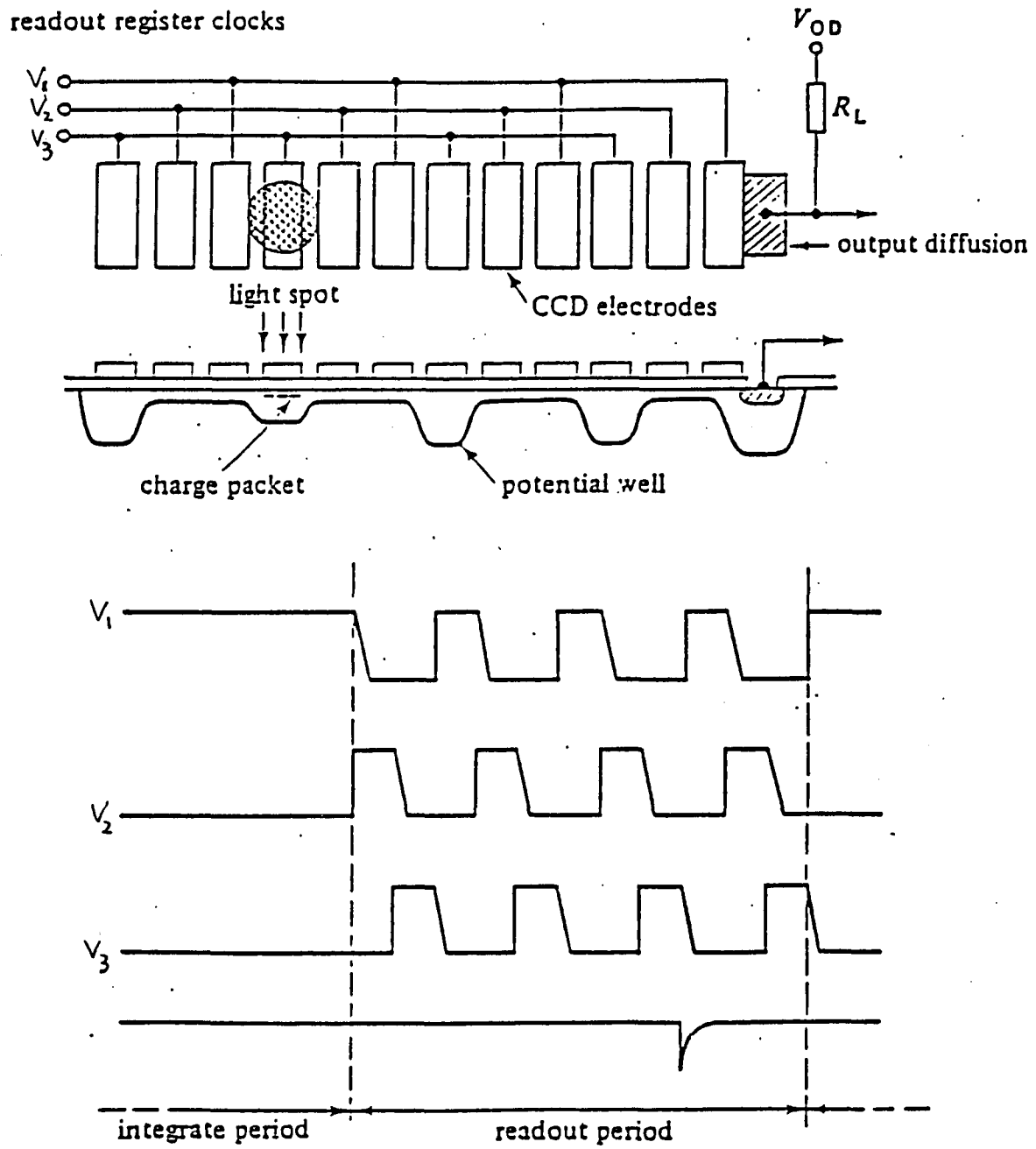


Fig.2.2 Basic principle of CCD imaging

the electrodes (depending on the electrode material), generate electron-hole pairs by the photoelectric effect. The minority carriers (electrons) generated within the depletion regions, or within a minority carrier diffusion length of the depletion regions, are collected under each V_1 electrode. The number of electrons collected under a given electrode within a given period of time, the integration period, is proportional to the local light intensity. At the end of the integration period the charge pattern is read out by clocking the array in a conventional manner, care being taken to ensure that the clocks run long enough to clear out every charge packet. Fig.2.2 shows the single output pulse that would ideally result from imaging a light spot. At the end of the readout period the device is again switched to the integration mode and the cycle is repeated. During the readout period light is, still incident on the array. Consequently, signal charge packets being transferred along the array will pick up additional spurious charge; an effect known as image smear. Image smear can be kept to acceptably low values for most applications by using a sufficiently high clock frequency for readout.

2.2.2 Basic properties of CCD image sensors

We must look at the device characteristics to determine the factors that limit its imaging performance

in terms of dynamic range, sensitivity and resolution.

Dynamic range and Sensitivity

The dynamic range of the CCD, expressed in terms of signal levels within the device, is determined at the upper end by the maximum charge handling capability and at the lower end by the various noise sources present. These signal levels may be converted into equivalent irradiance levels knowing the responsivity of the photosensitive elements. Responsivity describes the generation of signal charge from light energy and is usually expressed in amperes per watt. The dynamic range of a CCD image sensor is expressed as the ratio of the peak signal to r.m.s. noise measured at the output. The dynamic range potentially available with CCD image sensors is high, being on the order of 10^4 (80dB) for both BCCD and SCCD operation. Device sensitivity, i.e., the lowest signal level at which the device can give useful operation, is clearly a function of both the noise level and the responsivity. Noise performance will be discussed in Section 2.3.

Resolution

An important parameter of any image sensor is the spatial resolution that it provides, i.e., the ability to discriminate between closely spaced points in the image.

The modulation transfer function (MTF) describes the performance of a sensor in the spatial frequency domain. Normally, the MTF of a CCD is normalized to unity at zero spatial frequency and falls off at higher spatial frequencies as a result of the transfer inefficiency. More information about transfer inefficiency and derivation of its MTF will be given in Section 2.4.

2.3 Analysis of Noise in CCD Devices

A number of noise sources limit the sensitivity of a focal plane CCD system. There is noise associated with the scene photon flux, noise related to the CCD itself, and noise related to the output preamplifier. For the purpose of categorizing the noise sources, Fig.2.3 depicts the focal-plane array as consisting of three sections.

a) Photon noise

This noise is due to the random fluctuation in the number of photons incident on the detectors and manifests itself as shot noise in the device. Photon noise is approximated by a Poisson process that results in a standard deviation equal to the square root of the mean number of photons.

b) Input noise

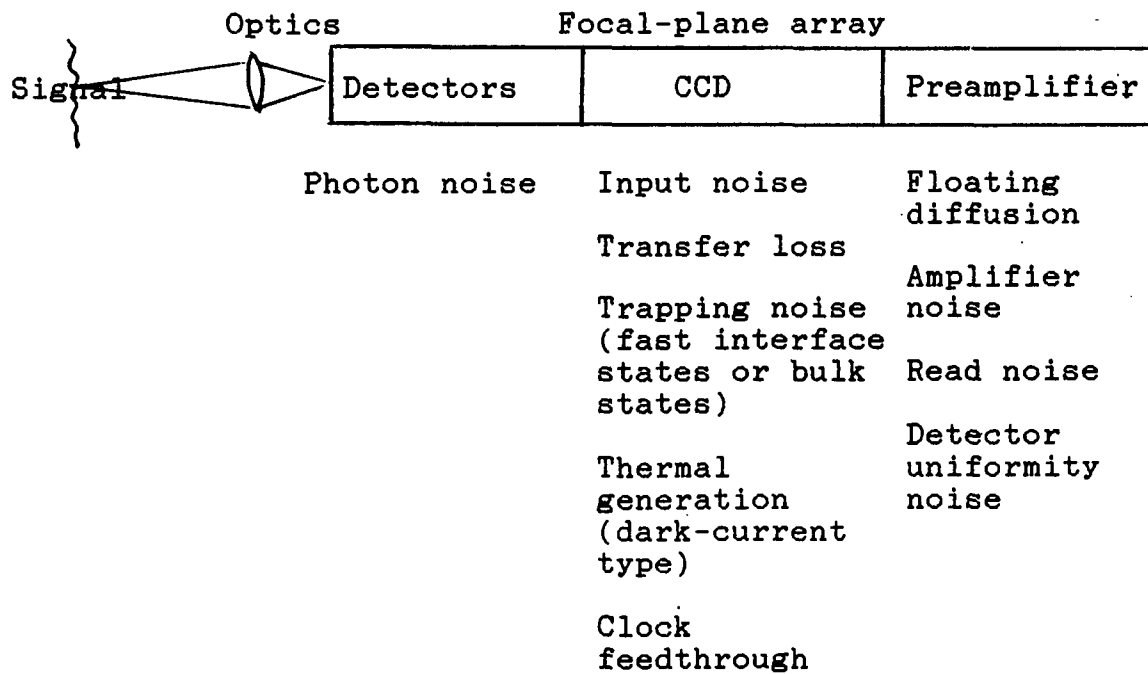


Fig.2.3 Noise sources in a system using a CCD

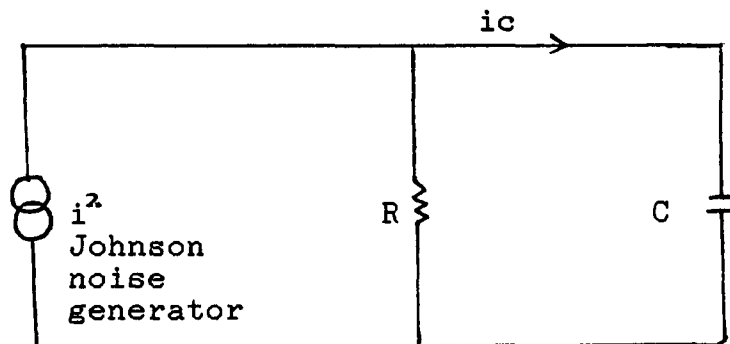


Fig.2.4 Equivalent circuit of input of charge to a potential well

The noise associated with transferring charge into a capacitor is often called KTC noise. This is the thermal noise of a resistor in parallel with a capacitor as shown in Fig.2.4. Input noise in a CCD is the same as KTC noise, and is caused by random injection of charge from a diffusion into a potential well.

c) Transfer noise

This noise describes the random amount of charge lost by a signal upon transfer and the random amount of charge added to a signal upon entering a well.

d) Trapping noise

A noise arising from random trapping emission from interface states or bulk states.

e) Dark-current noise

This noise, often called thermal generation noise, is associated with carriers that are thermally generated to bring the potential well into thermal equilibrium.

f) Clock feedthrough noise

This noise is due to capacitance coupling from the array gates to the output diode. It becomes more important at high frequencies.

g) Floating diffusion reset noise

This is a noise associated with the reset circuit on

the output preamplifier. This noise is the thermal noise of the MOSFET channel resistance in parallel with the floating diffusion capacitance, and is similar to input or KTC noise.

h) Amplifier noise

This noise is associated with a MOSFET of a given transconductance.

i) Read noise

Noise associated with reading the information from the focal-plane array, which is independent of time between reads.

j) Detector uniformity noise

This noise is the variation in the video output for a uniform radiation flux input. It can be caused by spatially varying responsivity or dark-current generation.

Expressions for noise sources associated with focal-plane arrays are in Table 2.2 and their typical values are shown in Table 2.3.

2.4 Charge Transfer Efficiency

Charge transfer efficiency is the primary source of the CCD MTF. Charge transfer is not perfect; some signal

Table 2.2 Expressions for noise sources associated with focal-plane arrays

Type	Expression rms carrier fluctuation	Terms
Photon	$[2GnEAT]^{1/2}$	G=photoconductive gain n=quantum efficiency E=photon irradiance A=pixel area
Input	$[KTCq^{-2}]^{1/2}$	K=Boltzmann's constant T=temperature C=input capacitance q=charge of electron
Transfer noise	$[2eNs]^{1/2}$	e=transfer inefficiency Ns=number of carriers in signal packets
Trapping noise	$[MKTANss\ln 2]^{1/2}$	M=number of gate transfers Nss=density of surface states
Dark current	$[JTA/q]^{1/2}$	J=dark current density
Floating diffusion	$[KTCq^{-2}]^{1/2}$	Co=output capacitance
Preamplifier noise	$[Co8KTf/q^23g]^{1/2}$	f=electrical bandwidth g=transconductance

Table 2.3 Principal noise sources in a typical CCD image sensor

Source	Typical values (r.m.s. carriers)
Photon noise	100 for $N_s = 10^4$ 1000 for $N_s = 10^6$
Background charge generation noise: Dark current	~100
Fast interface state trapping noise	~ 10^3 for SCCD 2000 ~ 10^2 for BCCD transfer
Output amplifier noise	~200

N_s is the number of electron carriers.

charge is left behind after the transfer process. Charge transfer efficiency (CTE) is the ratio of charge transferred to the initial charge present. A second quantity often used in the literature is transfer inefficiency, E , or the ratio of the charge lost to the initial charge packet. Thus

$$E = 1 - \text{CTE} \quad (2.1)$$

Typical values of CTE are on the order of 0.99999 for a good device or an E of 10^{-5} . The effect of a nonunity CTE is to cause the signal packet to be spread to gates that are adjacent to the signal-carrying gate. The charge packets occur in what perhaps were empty wells following the signal charge and therefore blur and reduce definition in the image.

Brodersen et al. (1975) classified three basic types of charge transfer loss mechanisms: fixed loss, proportional loss, and nonlinear loss. This approach lends itself to a mathematical model for transfer loss analysis. Fixed loss is loss of a fixed amount of charge during each transfer, and it is independent of the size of the signal charge. In the case of proportional loss, the E is a constant and is independent of the signal-charge amplitude. In the case of nonlinear loss, E is dependent on signal-charge amplitude.

The effect of a nonunity CTE on an image is to smear the image or reduce the MTF of the CCD array. If a sinusoidal signal is transferred through the array, the modulus is decreased and the phase is shifted as given by (Sequin and Tompsett, 1975).

$$\text{MTF} = \text{EXP}[-nE(1-\text{COS}(2\pi f/f_c))] \quad (2.2)$$

$$\text{PTF} = -n[2\pi f/f_c - \text{SIN}(2\pi f/f_c)] \quad (2.3)$$

where n = number of gates the charge transferred

f_c = spatial frequency cutoff

The MTF and PTF (phase transfer function) are plotted for varying amounts of charge loss, nE , in Fig.2.5. It is desirable to have the largest MTF, and, therefore, to make the total loss nE as small as possible.

2.5 Derivation of MTF and PTF for a CCD

Two derivations of the CCD MTF are given here. The first approach was described by W.B.Joyce and W.J.Betram (1971) and used the wave-equation to obtain the MTF in the frequency domain. The second approach was proposed by C.N.Berglund (1971). He derived the same equation as Joyce and Betram, but via the spatial domain.

2.5.1 Frequency domain approach

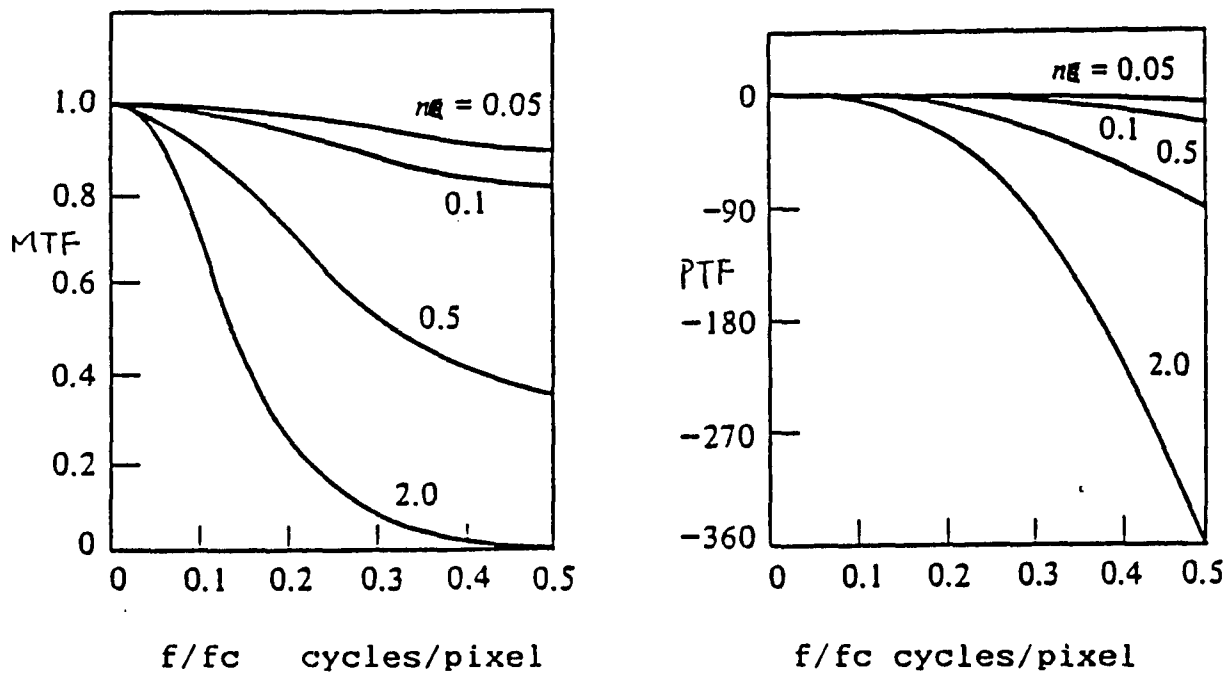


Fig.2.5 MTF and PTF versus relative frequency response for various amounts of loss.

Discrete charge transfer devices like CCD arrays are, to a good approximation, discrete in both space and time. That is, the information-bearing charge is moved in discrete time bursts from one spatially discrete storage station (potential well) to the next along a line of stations. Consider $Q_{x,t}$ the charge in station x at time t , where x and t assume only integer values; i.e., the unit of time is taken as the stepping interval, and the unit of distance is taken as the center-to-center station separation. Perfect charge transfer implies

$$Q_{x,t} = Q_{x-1,t-1} \quad (2.4)$$

and hence unit signal speed.

Real devices are typically characterized by the fraction A of the charge which is successfully advanced per step. If a fraction E fails to advance and remains in its original station, then the process is described by

$$Q_{x,t} = AQ_{x-1,t-1} + EQ_{x,t-1} \quad (2.5)$$

which reduces to eqn.(2.4) in the ideal case of $A=1$ and $E = 0$. In other words, eqn.(2.5) states that the charge in station x at time t , $Q_{x,t}$, is the successfully transferred fraction of the charge in the previous station at the previous time, $AQ_{x-1,t-1}$, plus a fraction E of the charge $Q_{x,t-1}$ in station x at the previous time

which failed to advance. From eqn.(2.5) it follows that a fraction $L=1-A-E$ of the charge is lost per step.

The dispersion relations can be found from the space and time Fourier transforms of eqn.(2.5) or by the separation-of-variables method. Either approach amounts to seeking a running-wave solution of the form

$$\text{Im}\{\text{EXP}[i(\omega t - kx + \phi)]\} \quad |x|, |t| = 0, 1, 2, \dots \quad (2.6)$$

where k and ω may be complex to account for the attenuation, and ϕ is any constant phase factor. Since x takes on only integer values, eqn.(2.6) is not affected by adding multiples of 2π to the real part of k, ω and thus without loss of generality we require $|\text{Re } k| < \pi$. Similarly, since time is discrete, all frequencies outside the fundamental range $|\text{Re } \omega| < \pi$ are redundant. In the theory of sampled-data systems, this is usually expressed by saying that the sampling frequency must be at least twice the maximum frequency to be detected. Substituting eqn. (2.6) into (2.5) yields for the dispersion relation between ω and k

$$\text{EXP}(i\omega) = A\text{EXP}(ik) + E \quad (2.7)$$

Since eqn.(2.7) shows that the dispersion relations are independent of ϕ , we take $\phi = 0$ hereafter.

In the case of image detection, k is real corresponding to a term in the spatial Fourier representation of the initial image. Equation(2.7) reduces to

$$w(k) = w' + iw'' \quad (2.8)$$

Set $E/A = B$

$$w(k) = k - \tan^{-1}(\text{SIN}k / (\text{COS}k + 1/B)) - i(\ln A + 1/2(1+B^2 + 2B\text{COS}k)) \quad (2.9)$$

i.e. the wave is attenuated in time but remains spatially sinusoidal.

In the practical case of small B , eqn.(2.9) is usefully approximated by truncating its expansion in powers of B after the linear term, i.e.

$$w(k) \rightarrow k - B\text{SIN}k - i[\ln A + B\text{COS}k], \quad \text{as } B \rightarrow 0 \quad (2.10)$$

$$\rightarrow k - E\text{SIN}k + i[L + E(1 - \text{COS}k)] \quad (2.11)$$

Eqn.(2.8) to Eqn.(2.9) and Eqn.(2.10) to Eqn.(2.11) are derived in Appendix A.

2.5.2 Spatial domain approach

Fig.2.6 gives a schematic representation of a three-phase register. The charge being transferred is stored on the capacitors C and the rectangles represent the

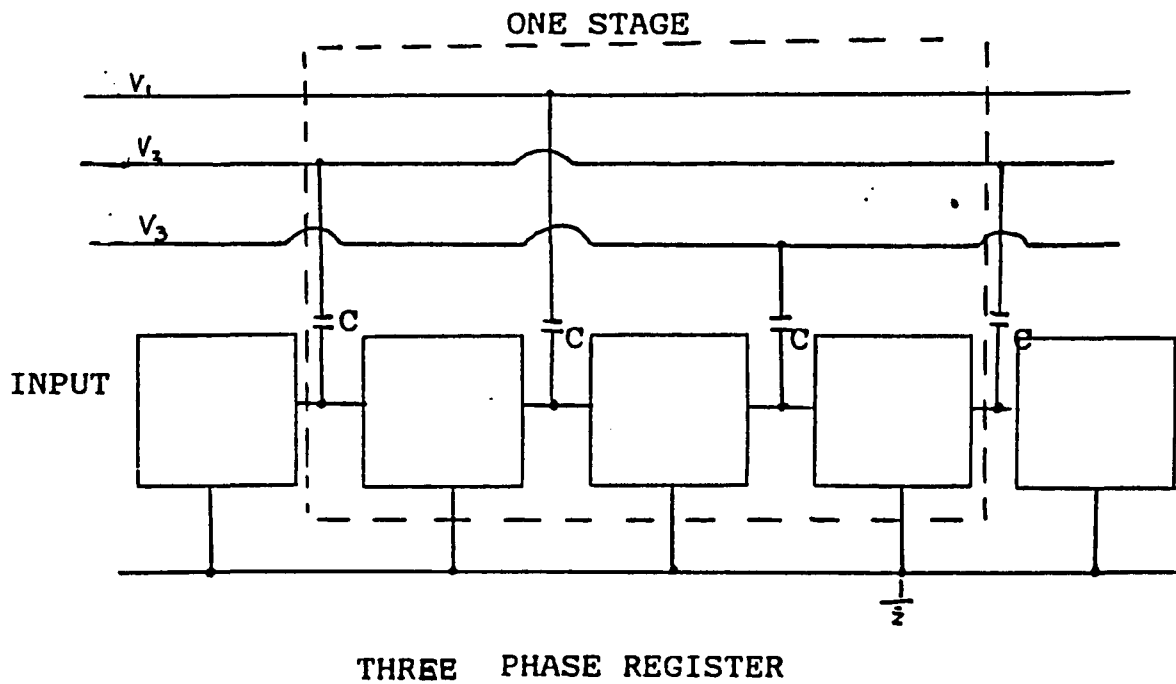


Fig.2.6 Schematic representation of three-phase charge-transfer shift registers.

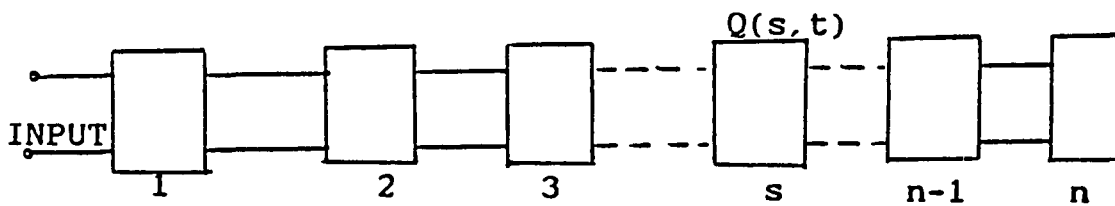


Fig.2.7 Illustration of an n-stage register.

mechanism by which the charge is gated from one capacitor to the next. Directionality is achieved by using appropriate three-phase clock signals V_1 , V_2 , and V_3 for the three-phase register. If the register under consideration uses a p -phase clock, then Fig.2.6 indicates that there must be p capacitors and p gates to transfer the charge for each bit or stage in the register.

During the transfer of charge from one capacitor to the adjacent capacitor, there are two major sources of signal degradation. The first is a fractional loss of charge and the second is incomplete transfer of charge. These effects have been discussed in the previous section on CTE.

Suppose we have an n -stage register with stages labeled one through n as shown in Fig.2.7 operating with a p -phase clock and with some analog input signal. Represent the charge in the s stage as the continuous function of s and t , $Q(s,t)$. Then remembering that there are p transfers per stage, we can assume that the charge left behind and that lost per stage is just p times the value per transfer and write the charge in the $s+1$ stage as

$$Q(s+1,t) = Q(s,t-T_c) + pA[Q(s+1,t-T_c) - Q(s,t-T_c)] - pBQ(s,t-T_c)$$

(2.12)

where T_c = period of clock signal for each stage

A = incomplete transfer parameter

B = fraction of signal charge being lost

After removing the time dependence by changing to the frequency domain eqn.(2.12) becomes

$$Q(s+1,w)=[1-pA-pB]/(1-pA\text{EXP}(-iwT_c))\text{EXP}[-iwT_c]Q(s,w)$$

(2.13)

Given the appropriate boundary conditions eqn. (2.13) can be solved exactly to obtain Q as a function of both position and time. For example, after n stages $Q(n,w)$ is given by

$$Q(n,w)=[1-pA-pB]/(1-pA\text{EXP}(-iwT_c))]^n \text{EXP}[-iwT_cn]Q(0,w)$$

(2.14)

In order to obtain the same form of equation eqn.(2.11), see the derivation in Appendix B.

The linear analysis of charge-transfer illustrates the important effects on performance of nonideal charge transfer. In the absence of incomplete charge transfer and charge loss, the time delay in sending an analog signal through an n -stage register is nT_c as expected and there is no signal attenuation. If there is charge loss

during transfer but transfer is essentially complete, there is only a simple attenuation of the signal varying exponentially with the number of stages and no change in the time delay. However, incomplete charge transfer has two effects. First a frequency-dependent attenuation occurs that depends exponentially on the number of stages and the square of the signal frequency to first order. Second, there is an increase in the time delay through the register that depends on the fraction of charge left behind during transfer.

Chapter 3

THE SPOT SATELLITE SYSTEM AND SYSTEM MODELING

The instruments carried by the American satellites of the TIROS and NIMBUS series in the 1960s, which offered a ground resolution of the order of 1000m, were the first to employ space for earth observation. Meteorological remote sensing continues in the 1980s with the Advanced Very High Resolution Radiometer (AVHRR) sensor. Second generation remote sensing instruments, with resolutions of the order of 30-80m, were developed during the 1970s for the Landsat Multispectral Scanner System (MSS), Thematic Mapper (TM) sensors. The 1980s have seen the introduction of instruments with resolutions of the order of 10m. The first such instrument is the high resolution visible (HRV) camera on the SPOT (Systeme Probatoire d'Observation de la Terre) satellite system, which utilizes CCD array technology as described in Chapter 2. In this chapter the SPOT satellite system is first described with information provided by the French Centre National d'Etudes Spatiales (CNES). Second, a system

model and parameters for this system are studied. After specifying the parameters, comparisons are made to system models for MSS, TM, and AVHRR.

3.1 General Description of SPOT System

The SPOT system, planned and designed by the CNES, is built by French industry in cooperation with Belgium and Sweden. The SPOT system consists of an Earth observation satellite and of earth stations for data reception. The design lifetime of the first SPOT satellite is two years. SPOT-1 was launched on Feb 21st, 1986 and a second satellite is under construction. Two additional satellites are planned to ensure service over a ten year period. SPOT-1 has three spectral bands, 500-590 nm, 610-680nm, and 790-890nm in the visible and near infrared portions of the spectrum, each with a ground resolution of 20 meters, and a 510-750nm panchromatic band, with a ground resolution of 10 meters.

Fig.3.1 shows the nadir viewing mode of SPOT. One of the key features of the SPOT instrument package is the provision of off-nadir viewing, i.e.the instrument can be programmable to "look" to one side or the other of the satellite ground track. This off-nadir viewing capability covers a range of ± 27 degrees relative to nadir. This allows the instrument to view any point within a strip

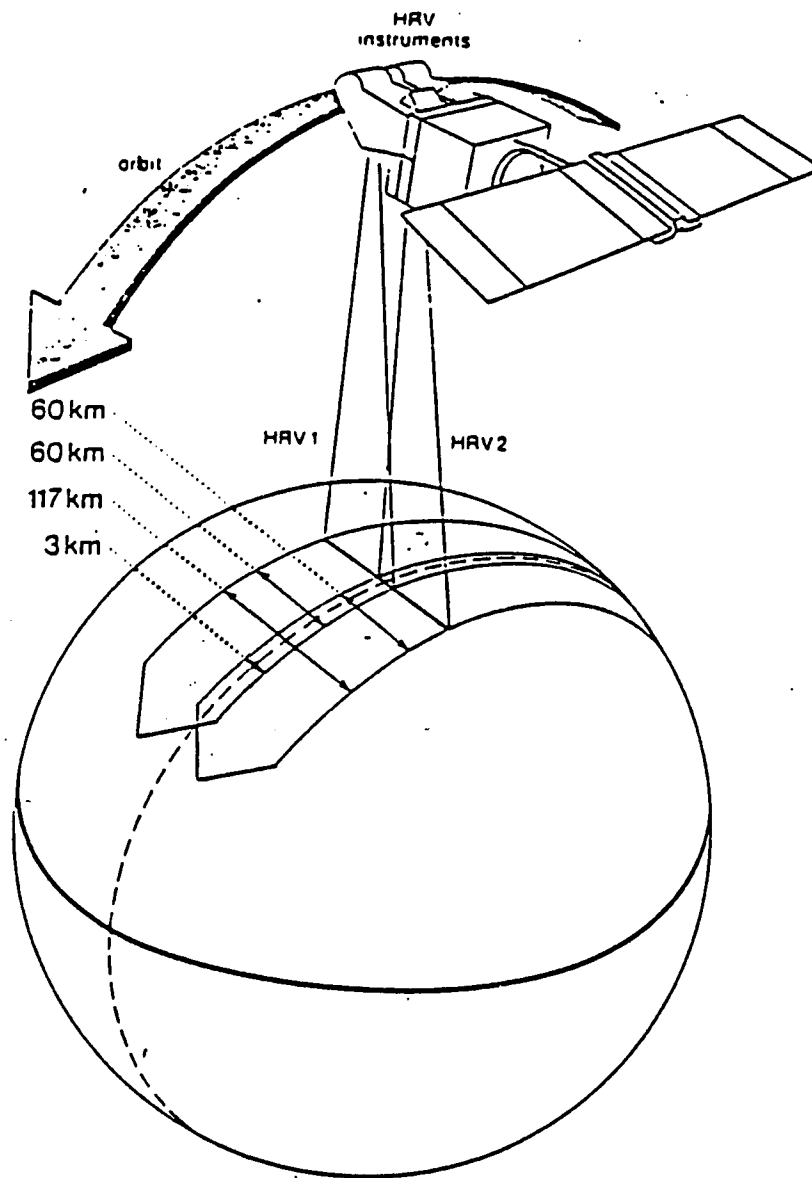


Fig.3.1 Nadir viewing of SPOT

extending 475km to either side of the satellite ground track. The off-nadir viewing capability, along with the high resolution, are two of the most innovative features of the HRV instrument. Another feature of the HRV is the recording of stereoscopic image pairs of a given area during successive satellite passes.

The payload of SPOT-1 consists of two identical HRV imaging instruments, two magnetic-tape data recorders and a telemetry transmitter. The HRV instrument is designed to operate in either panchromatic (Pan) or multispectral (XS) modes. The instrument's sampling grid corresponds to a ground element (pixel) that is 10m X 10m in Pan data and 20m X 20m in XS data.

3.1.1 HRV detection unit

The HRV instrument uses the "push-broom" technique for image generation instead of the "whisk-broom" used in the Landsat systems (Fig.3.2), thus eliminating the need for mechanical scanning. The CCD elements in the linear array are sampled at the appropriate frequency as the satellite moves along its orbit.

Spectral separation of the four channels is done in the focal plane by a beam-splitter assembly. In the panchromatic mode, there is one-to-one correspondence between CCD sensing elements and pixels. In the

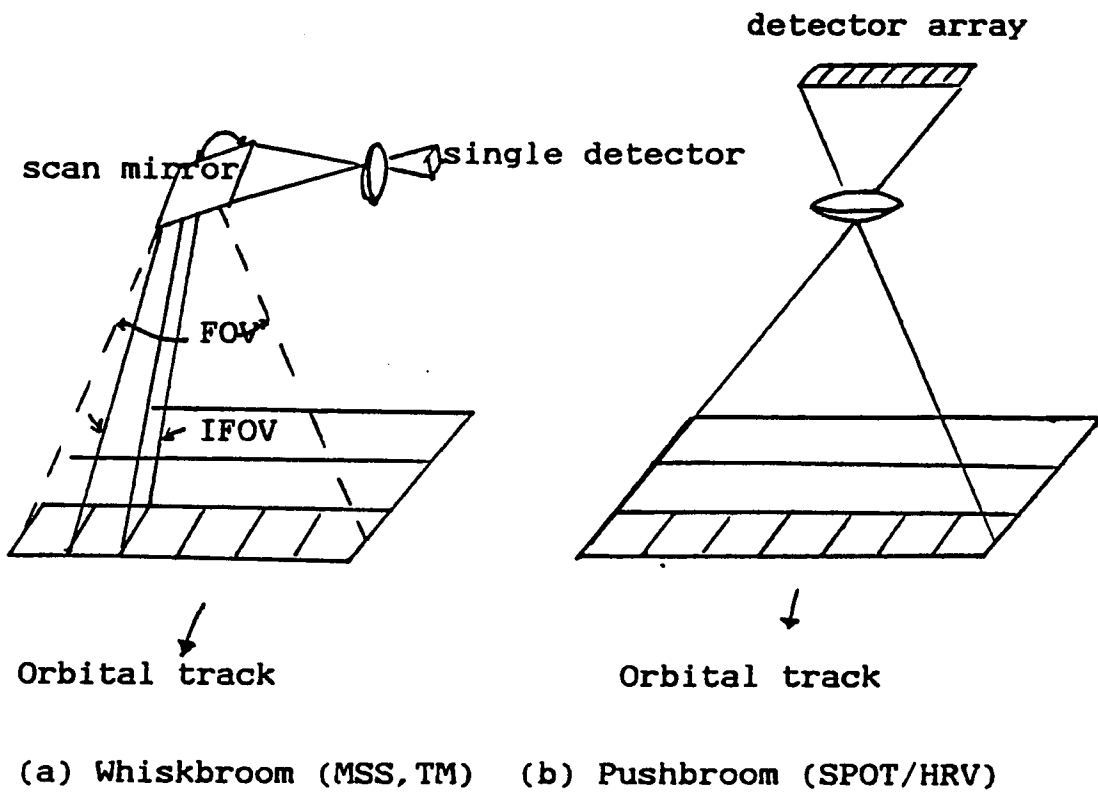


Fig.3.2 Sensor scanning methods

multispectral mode, two CCD elements are used to produce one across-track pixel. A 20m pixel is achieved along-track by doubling the integration time.

3.1.2 The SPOT CCD System (Fairchild Model CCD 122H)

Fairchild model CCD 122H is used in the HRV detection unit of SPOT-1. The following technical information is provided by Fairchild in their CCD catalog (1984).

General description

The CCD 122H units are monolithic 1728 element image sensors. The 1728 sensing elements provide 200-line per inch resolution across an 8-1/2 inch page, which is an international facsimile standard. The photoelement size is 13 micrometers by 13 micrometers, on 13 micrometers centers. Devices are manufactured using Fairchild n-channel isoplanar buried-channel technology.

Structure of a photosensitive element

Each element is made of an n-p photodiode overlaid with silicon dioxide and associated with a MOS capacitor which collects the electrons created by the incident light. The quantity of charge accumulated is proportional to the incident irradiance and to the integration time. The charges are stored on the surface in the MOS capacitor. The photodiode/MOS capacitor arrangement

permits the separation of the photosensitive elements from the analog shift register by 80 micrometers. This reduces diffusion of the photoelectrons towards the analog registers.

The data carried by the readout CCD analog shift registers can be perturbed by the charges created in the photosensitive zone during integration, which can diffuse into the potential wells of the registers. This perturbation, known as crosstalk or lateral sensitivity, increases in the near-infrared and partially accounts for the reduced MTF at longer wavelengths. For long-wavelength radiation, the charges are created deep in the substrate, and thus diffuse easily towards the register.

3.2 SPOT Image Formation System

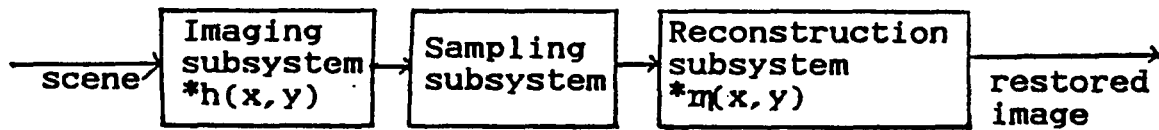
A typical imaging, sampling and reconstruction system is illustrated in Fig.3.3. In this chapter the imaging system will be studied but sampling and reconstruction are put off to the next chapter.

3.2.1 Imaging subsystem

Ignoring noise problems, the degradation, or blurring, process can be represented mathematically as

$$g(x,y) = \iint_{-\infty}^{\infty} h(x,y,x',y')f(x',y')dx'dy' \quad (3.1)$$

where the function $g(x,y)$ represents the image and $f(x,y)$



The spatial co-ordinates (x,y) can be referenced to the scene. (u,v) is the relative position to the sampling grid.

Fig.3.3 Description with explicit sample-scene phase (u,v) . The phase parameters have the range $\pm\frac{1}{2}$ pixel.

is the original scene. The function $h(x,y,x',y')$ represents the degrading source and is called the point spread function (PSF). The PSF of the imaging subsystem must account for all the system processing prior to sampling. In the SPOT system it includes the image-forming optics, scanning aperture, and electronic filter in the across-track direction. In the along-track direction, it includes the image-forming optics, the scanning aperture and integration time. In general, the imaging subsystem acts as a low-pass filter to the spatial frequency components of the input scene, producing an output image which is blurred.

In equation 3.1, the blurring process $h(x,y,x',y')$ has four variables (x,y,x',y') such that it varies with the position of the original image as well as that of the observed image. Such a degradation is spatially variant. These blurred images are more difficult to restore than spatially-invariant blurred images, as the spatial variance is unpredictable. Fortunately, each component in the SPOT imaging subsystem has linear spatially-invariant properties. In such cases, h will be a function of two variables $x-x'$ and $y-y'$.

For a noiseless, linear, shift-invariant system, eqn.3.1 reduces to

$$g(x-u,y-v) = h(x,y)*f(x-u,y-v) \quad (3.2)$$

where (u,v) are the sample-scene phase in (x,y) relative to an arbitrary coordinate origin. The symbol $*$ represents convolution, which is defined as

$$h(x,y)*f(x,y) = \iint_{-\infty}^{\infty} h(x-x',y-y')f(x',y')dx'dy' \quad (3.3)$$

Because of linearity, we can cascade components in series by simple convolution in the spatial domain or multiplication in the frequency domain.

3.3 SPOT Modeling

A Fortran program was written to model the Landsat series MSS and TM as well as the AVHRR system (Schowengerdt and Wood 1985, Schowengerdt and Li 1987). In this program, several system parameters must be specified as derived from the available information for each system. The program assumes separability of the two-dimensional LSF and TF for the whiskbroom systems. This assumption is also valid for the HRV pushbroom system. The software was modified to include modules for the SPOT sensor model.

There are two directions of interest for a pushbroom scanner, across-track and along-track. The imaging system

components in the across-track direction are:

- 1) image-forming optics
- 2) scanning aperture
- 3) electronic filter

In the case of whiskbroom systems, the electronic filter is a separate low pass filter. In the linear CCD of the HKV it is the charge transfer inefficiency modeled as a filter (Chapter 2).

In the along-track direction, there are three components that make up overall imaging subsystem:

- 1) image-forming optics
- 2) scanning aperture
- 3) sample integration

The third component in the along-track direction is different from whiskbroom scanners, which have sample integration in the across-track direction.

In our modeling, each system component is linear shift-invariant (LSI) to fit the model used in Section 3.2.1. Component transfer functions may then be cascaded to form the system TF (STF) or system point spread function (SPSF).

$$\text{STF} = \text{TF}_1 \times \text{TF}_2 \times \dots \quad (3.4)$$

$$\text{SPSF} = \text{PSF}_1 * \text{PSF}_2 * \dots \quad (3.5)$$

For most scanner systems the component LSI behavior is valid up to the sampling subsystem (Fig.3.3). Besides being linear scanner TFs are also separable in the across-track and along-track direction. This separability reduces the system model to a product of two one-dimensional models.

In modeling components in the across-track and along-track directions, the optics and scanning aperture are modeled with the same functions but with different parameters. To find the LSF of each component, we develop the model in the frequency domain and then use the inverse Fourier transform.

3.3.1 Image forming optics

To provide a convenient single number description of an optical system's PSF, the concept of blur circle is often used. The blur circle is given by the diameter of the circle which encloses a specified fraction of energy within the PSF. In this respect, a Gaussian function is often used to find the blur circle (Park, et.al., 1984). In the case of SPOT we used the following model:

$$\text{MTF} = \text{EXP}(-\text{BLUR} \cdot \text{MUP})^2 \quad (3.6)$$

where MUP has units of normalized spatial frequency (f/f_c) or cycles/pixel and f_c is the sampling frequency. BLUR is the parameter value calculated for different bands in both across-track and along-track directions. In the SPOT system, the optics MTF is lower than that of other systems on a normalized frequency scale (Fig.3.4).

3.3.2 Scanning aperture

The scanning aperture in the HRV is not actually an "aperture", but rather the area of the focal plane sensed by each detector. The scanning aperture is nominally square, but may deviate slightly because of manufacturing variations. It defines an angular relation, the instantaneous-field-of-view (IFOV), when divided by the focal length of the optics, f ,

$$\text{IFOV}(\text{radians}) = \text{scan aperture linear dimension}/f \quad (3.7)$$

Because it is an angular quantity, the IFOV may also be projected into the object space as an equal angle. When multiplied by the altitude of the sensor, H , the ground-projected scan aperture linear dimension is also commonly referred to as the IFOV,

$$\text{IFOV}(\text{meters}) = \text{IFOV}(\text{radians}) \cdot H(\text{meters}) \quad (3.8)$$

The model used for the scan aperture is

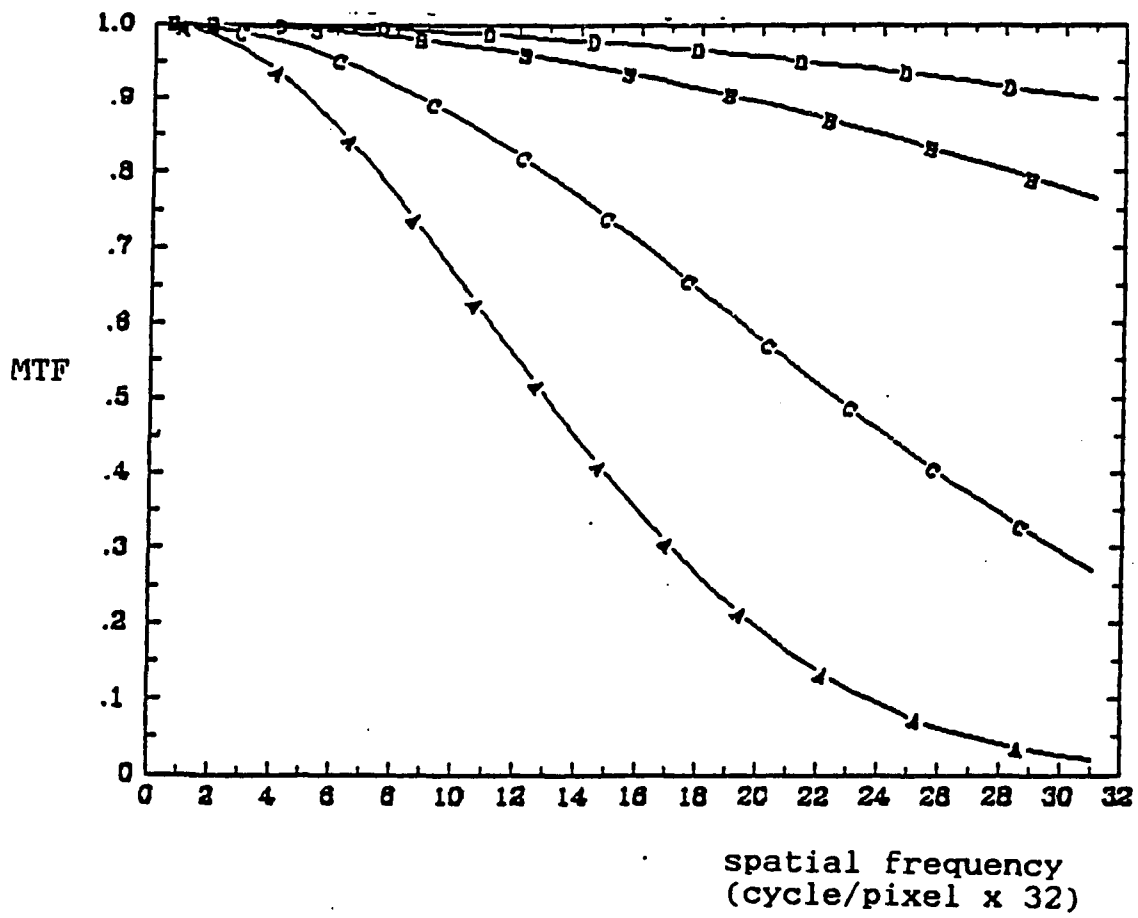


Fig.3.4 Optics MTFs of different systems
A-SPOT B-MSS C-TM D-AVHRR without sampling

$$\text{MTF} = |\text{Sinc}(\text{IFOV} \cdot \text{MUP} \cdot k)| \quad (3.9)$$

where k is a parameter to compensate for variation of the IFOV in system. Different system IFOV MTFs are shown in Fig.3.5 on a normalized frequency scale.

3.3.3 Electronic filters

These components are usually introduced to remove high frequency noise in the scan data or to pre-filter the data and limit its frequency content before the sampling step. In the latter case, the filter serves to reduce the "aliasing" effects in sampled data. The electronic filter is normally a low-pass type of filter, i.e., it passes low frequency components with little modulation reduction and attenuates the high frequency components. This component is the primary source of asymmetry in the SPOT SPSF, as was the case for the MSS, TM, and AVHRR. However, this asymmetry is much less for SPOT.

In SPOT, the CCD transfer function is analogous to the along-scan (cross-track) electronic filters present in whiskbroom scanners, but it is periodic and has a high magnitude throughout the frequency range of interest. CCD devices have a particular transfer function (Beyon and Lamb, 1980; Tompsett, 1972),

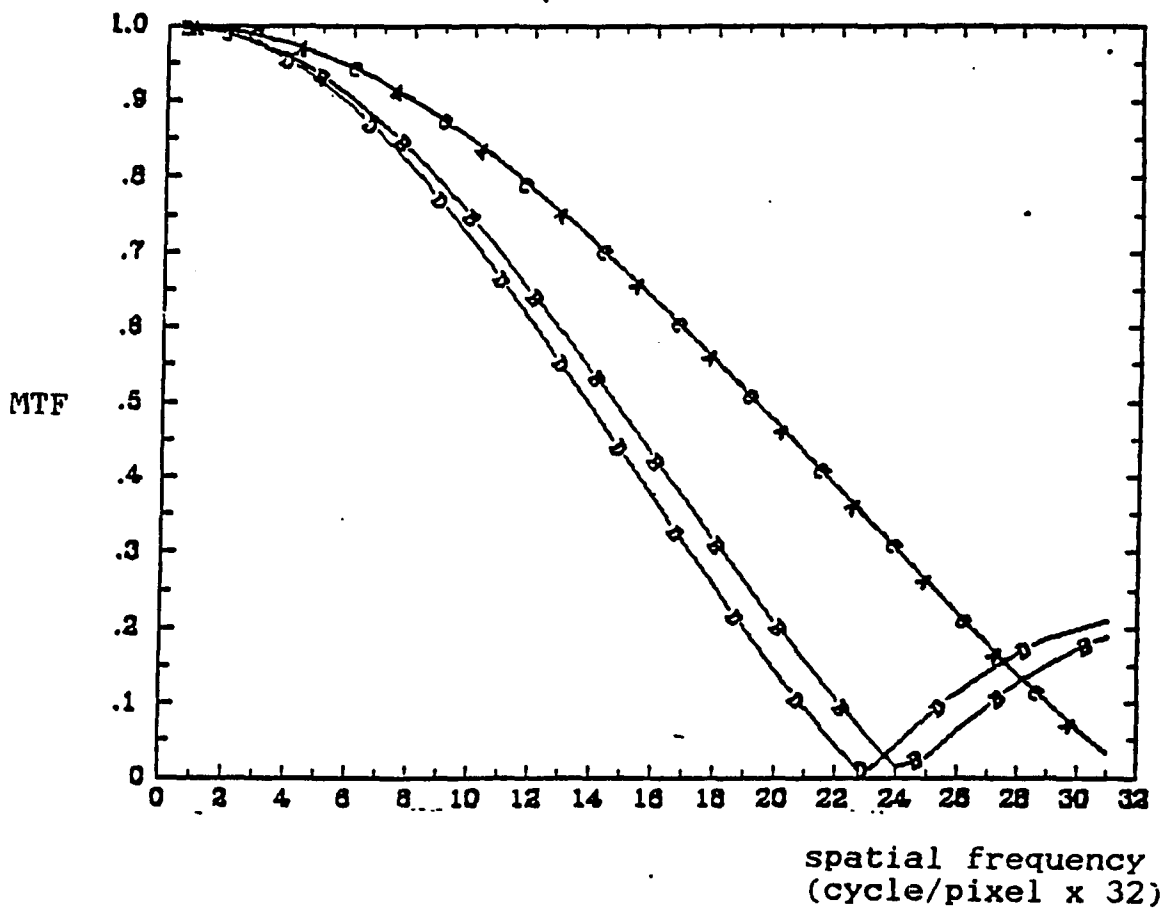


Fig.3.5 IFOV MTFs of different systems
 A-SPOT B-MSS C-TM D-AVHRR without sampling

$$\text{MTF} = \text{EXP}\{-nE[1-\text{COS}(2\pi f/f_c)]\} \quad (3.10)$$

$$\text{PTF} = -n[2\pi f/f_c - \text{SIN}(2\pi f/f_c)] \quad (3.11)$$

where n : total number of detector elements in the CCD array

E : charge transfer inefficiency per element

nE : total charge transfer inefficiency

f_c : sampling frequency

Therefore if nE increases, the CCD TF decreases. Eqn.(3.10) and eqn.(3.11) are shown in Fig.3.6 and Fig.3.7 respectively.

The CCD TF is a periodic function which may lead to "aliasing" at high frequencies. However, the low optics MTF draws down the overall MTF and prevents the aliasing.

3.3.4 Sampling integration

The radiance value at each pixel is not an instantaneous value from the track data in the SPOT case, but represents an integration of the signal over a small, but non-zero time. This integration is equivalent to an additional one-dimensional convolution in the along-track direction between the input signal and the time response of the sample. In a technical paper by Leroy (1987), the integration effect is modeled by a sinc function and has

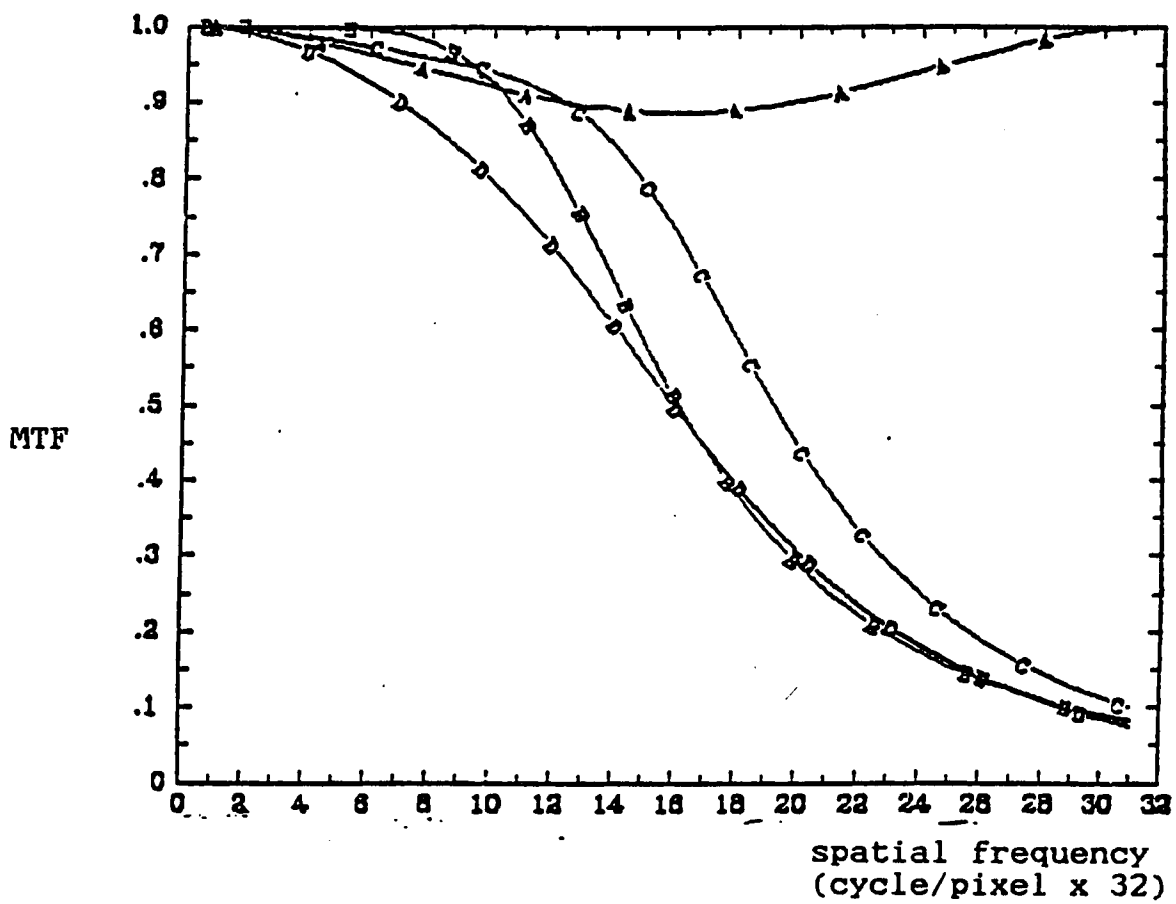


Fig.3.6 Electronic MTFs of different systems
A-SPOT B-MSS C-TM D-AVHRR

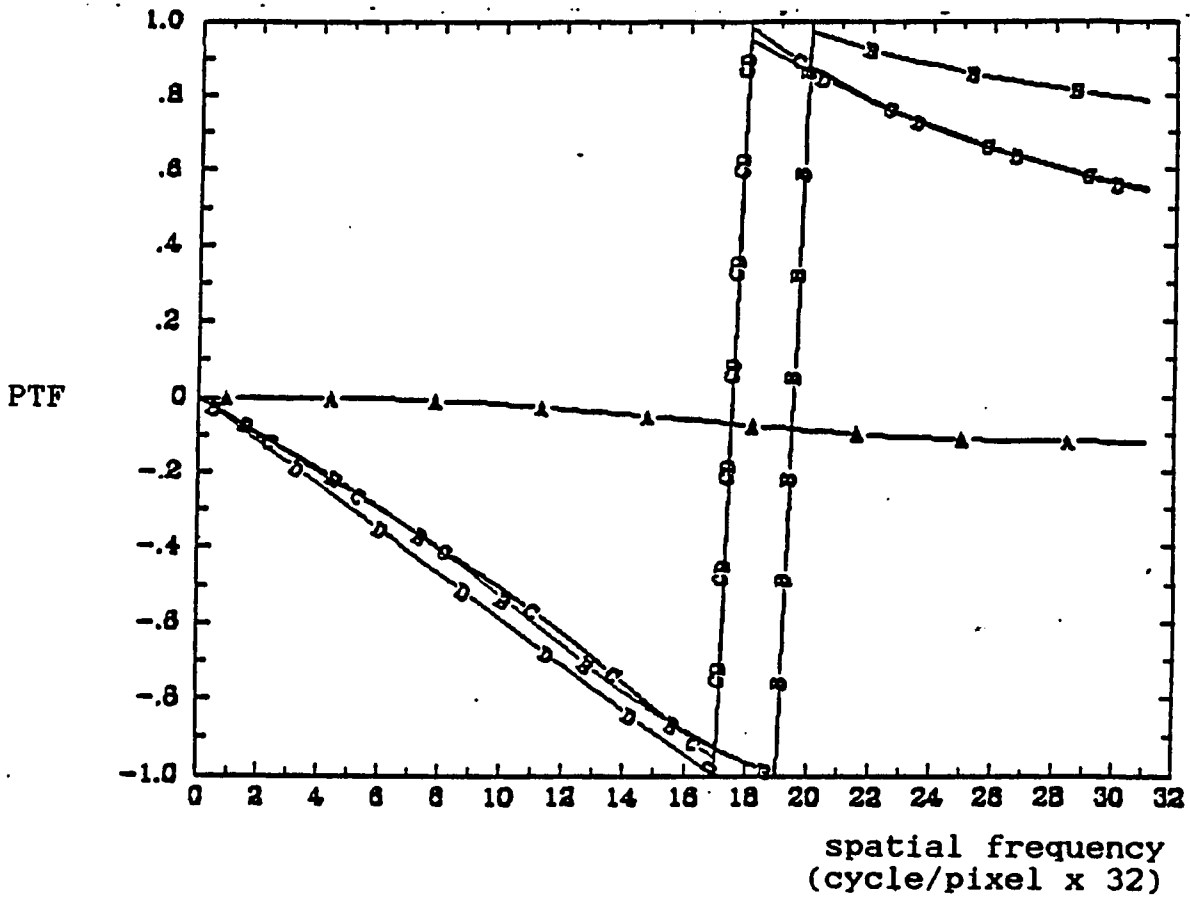


Fig.3.7 Electronic PTFs of different systems
 A-SPOT B-MSS C-TM D-AVHRR

a width similar to the IFOV. Hence, the model used for sample integration is

$$\text{MTF} = |\text{sinc}(\text{IFOV} \cdot \text{MUP})| \quad (3.12)$$

3.4 Panchromatic Band Model

In order to find parameters such as blur, IFOV and nE in our components model, empirical SPOT MTF data in Leroy (1987) is used. We model the along-track direction by adjusting IFOV to fit the detection unit data. As the IT (integration time) is specified in the system design. We are only required to vary the optics MTF to yield the best fit to the experimental data, by changing the parameter 'BLUR' progressively in the optics function. The empirical data measured at $fc/4$, $fc/2$ and $3fc/4$ and separate component functions are shown in Fig.3.8.

By using the same optics function with IFOV in the across-track direction, the CCD TF may be found by adjusting the parameter nE . A best fit is shown in Fig.3.9. The corresponding SLSF in both directions, without sampling effects included, are shown in Fig.3.10 and Fig.3.11.

3.5 Multispectral Band Model

The same approach is applied to the multispectral bands in the across- and along-track directions to model

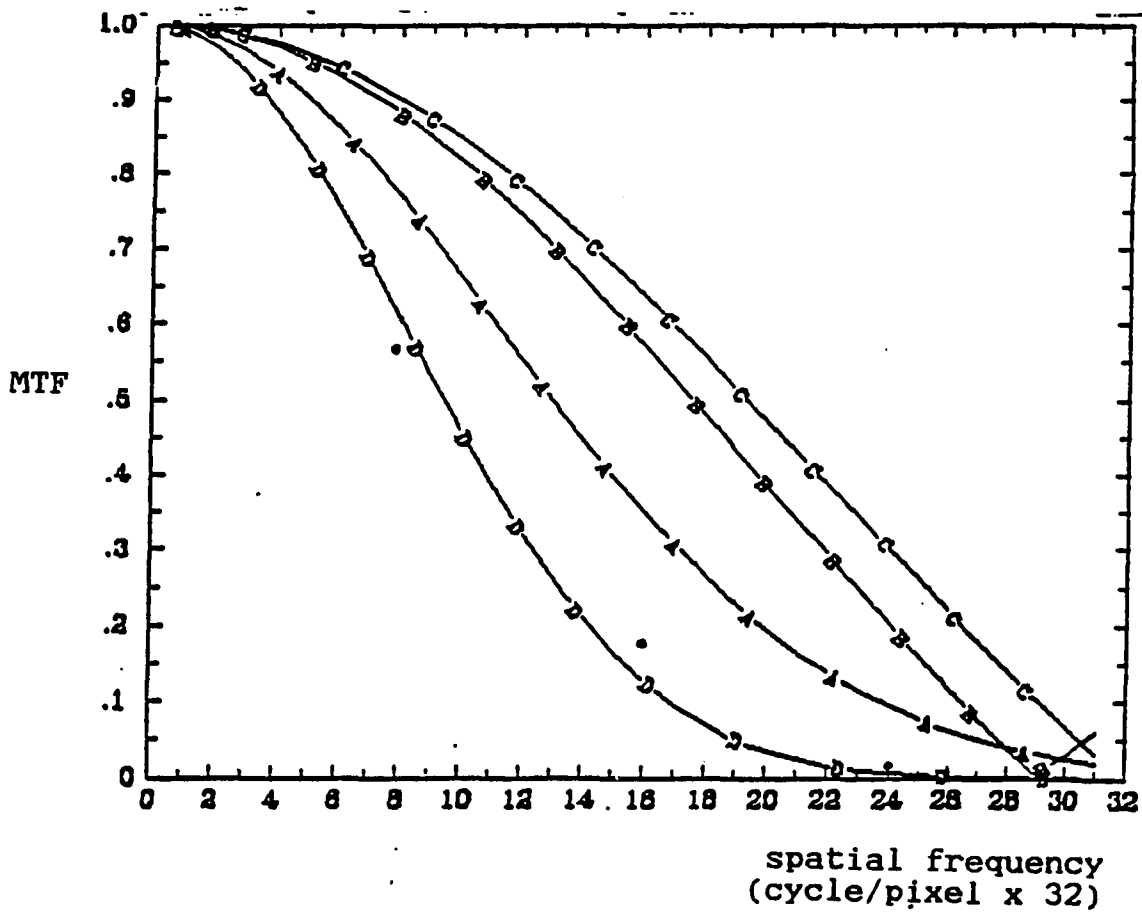


Fig.3.8 Separate components in along-track direction. A-Optics B-IFOV C-IT D-Overall system TF

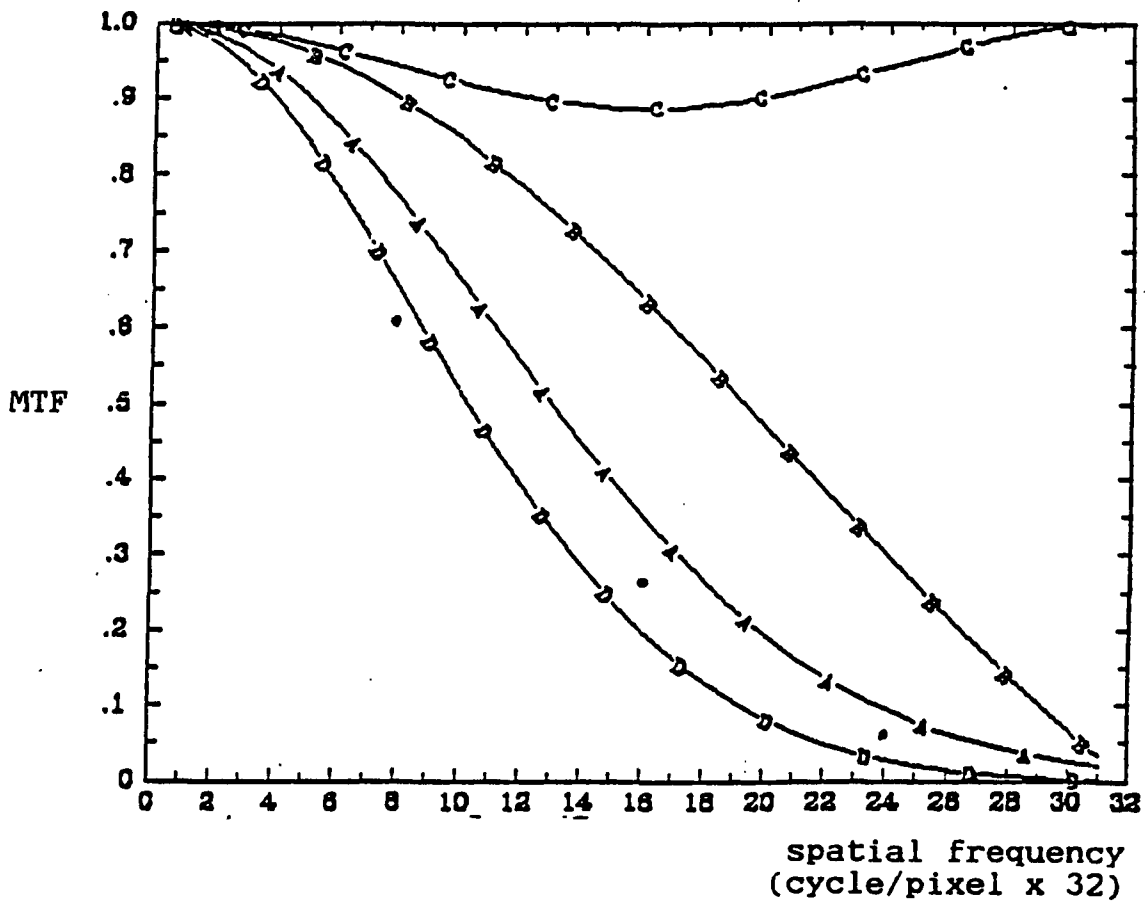


Fig.3.9 Separate components in across-track direction. A-Optics B-IFOV C-CCD TF D-Overall system TF

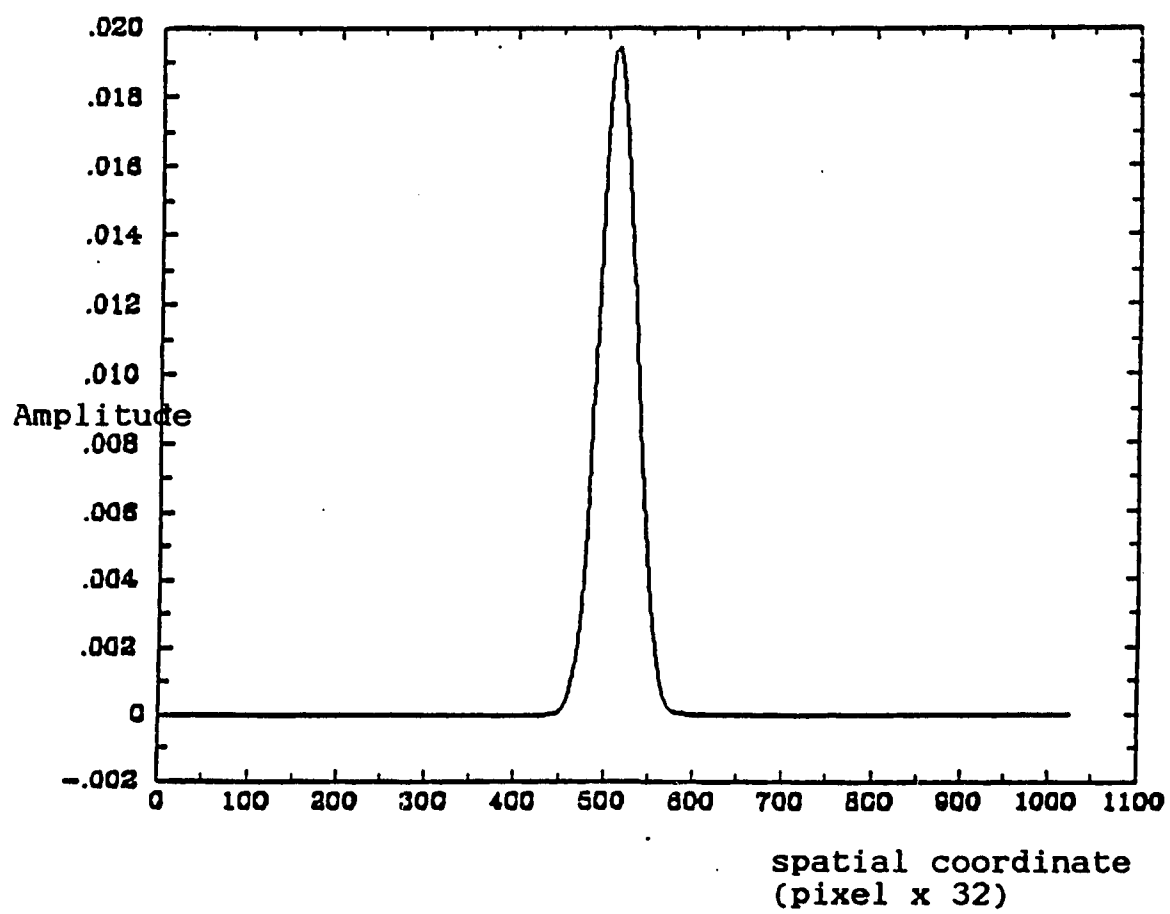


Fig.3.10 System line spread function of SPOT
in along-track direction

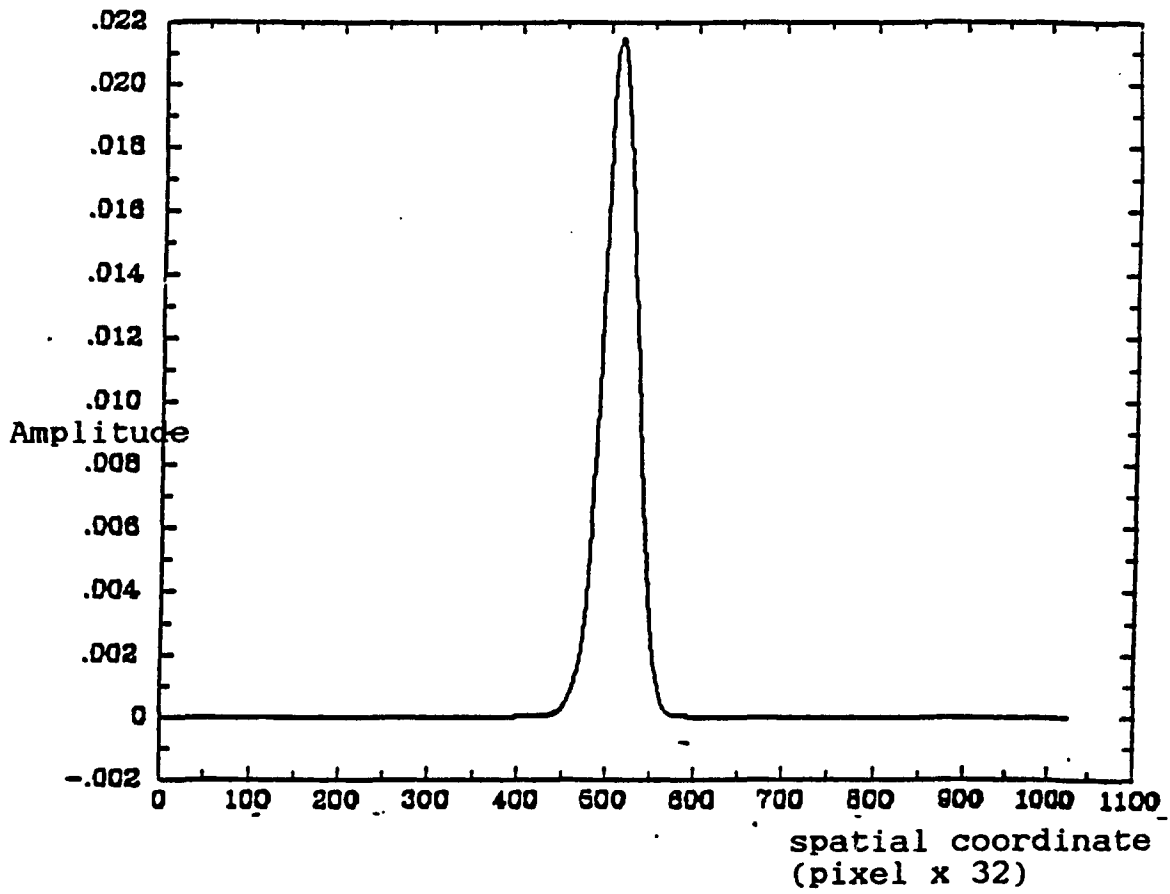
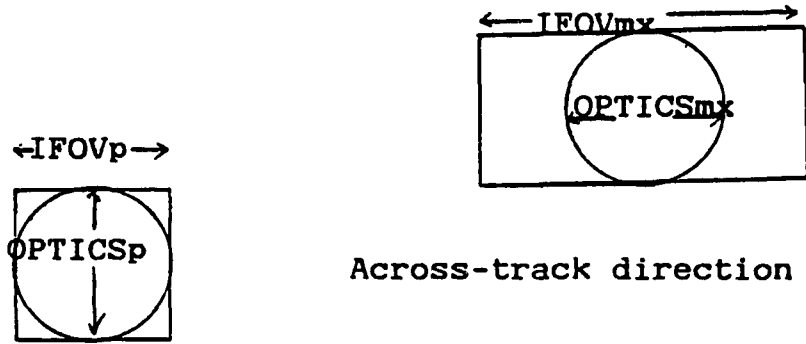


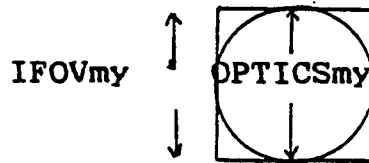
Fig.3.11 System line spread function of SPOT
in across-track direction

the STF. Because of the normalized spatial frequency used in our model, different physical dimensions between panchromatic and multispectral bands must be taken into account. Fig.3.12 illustrates the different dimensions of the optics PSF and IFOV in both across- and along-track directions for the multispectral bands and panchromatic band. Because the multispectral band has 20m/pixel in both across- and along-track directions and panchromatic band has only 10m/pixel. If a periodic scene has frequency $1/w$ cycles/m, it will be normalized to $20/w$ cycles/pixel in the multispectral band, but $10/w$ cycles/pixel in the panchromatic band. Therefore, the same physical dimension can be normalized to two scales. In the along-track direction, the spatial function of the optics PSF and IFOV in multispectral bands are as wide as their counterparts in the panchromatic band, say with width w ; in the spatial frequency, they should have a width of $1/w$. By using the same calculation above, IFOV and optics TF in multispectral band will be stretched out. On the other hand, the spatial function of the across-track IFOV in the multispectral band is twice as wide as that in the panchromatic band. Thus, the TF of the IFOV is kept the same on a normalized scale. The overall modeled functions in the multispectral bands are shown from Fig.3.13 to Fig.3.18 with the overall measured



Across-track direction

Across- and along-track direction



Along-track direction

(a) Panchromatic band

(b) Multispectral band

$$\begin{aligned} \text{IFOVp} &= \text{IFOVmy} = \frac{1}{2} \text{IFOVmx} \\ \text{OPTICSp} &= \text{OPTICSmx} = \text{OPTICSmy} \end{aligned}$$

Fig.3.12 Different dimensions of IFOV and OPTICS between Panchromatic and Multispectral bands

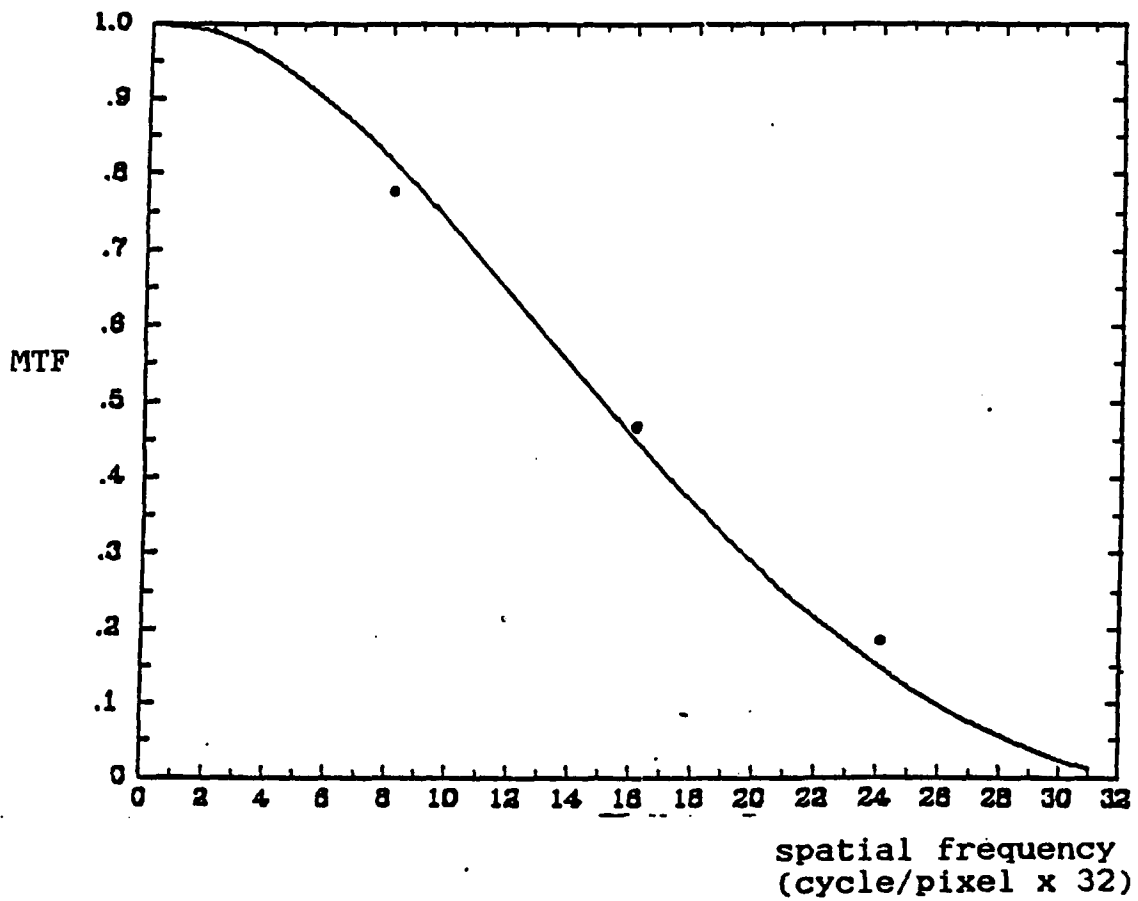


Fig.3.13 Overall system TF in band 1
(across-track direction)

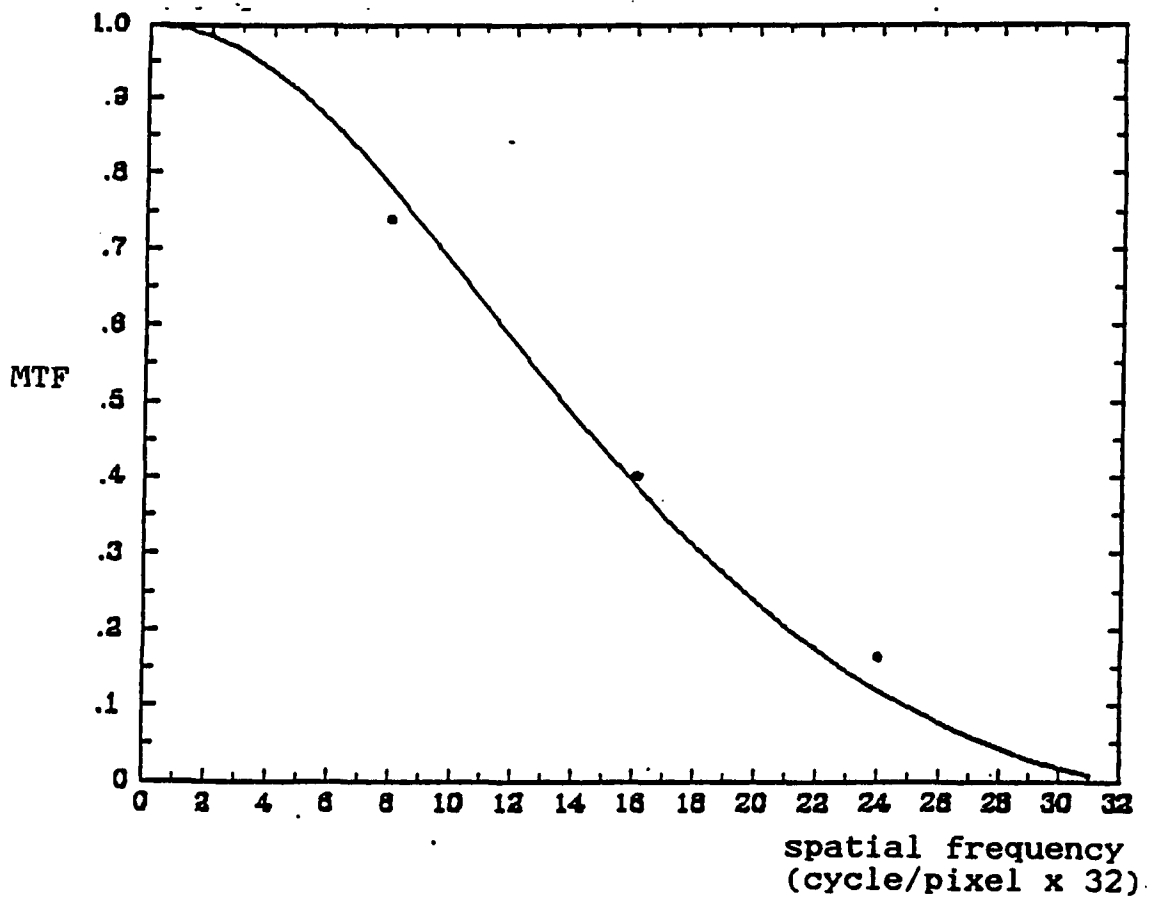


Fig.3.14 Overall system TF in band 2
(across-track direction)

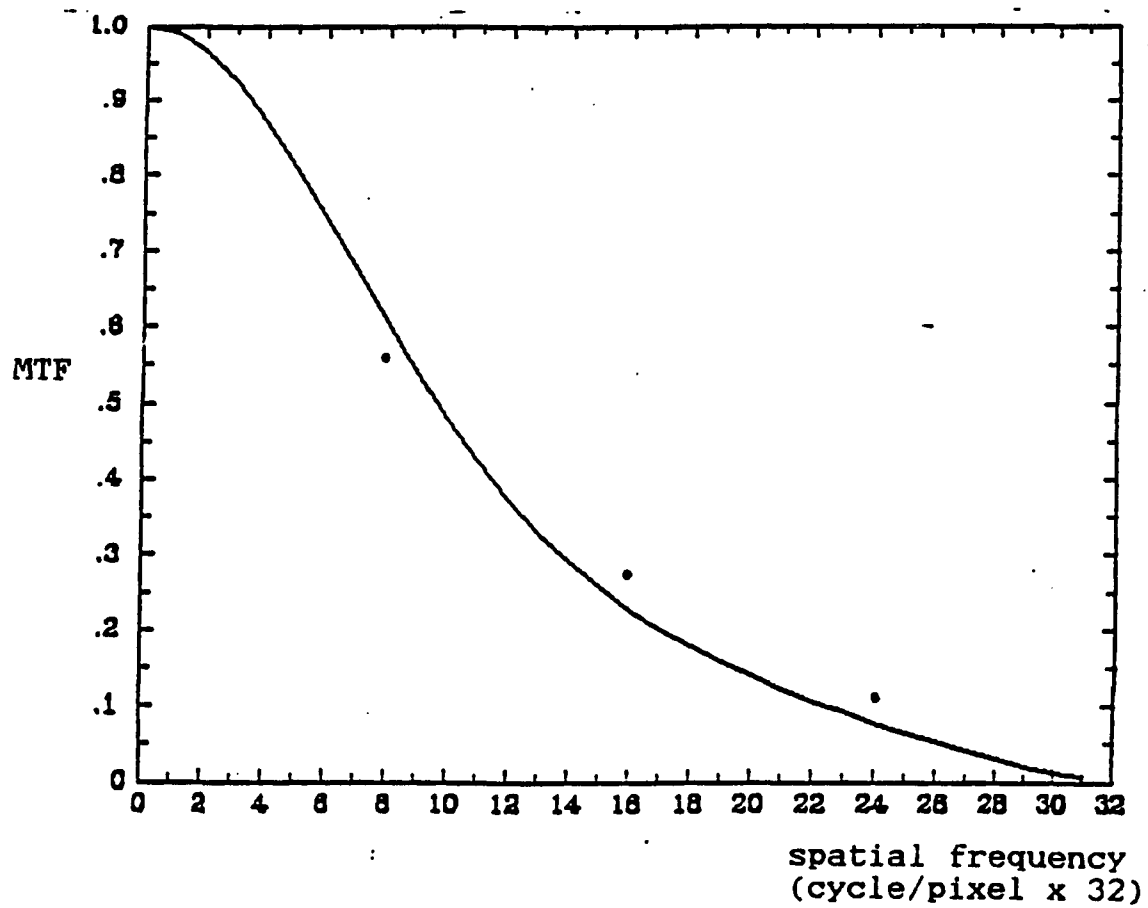


Fig.3.15 Overall system TF in band 3
(across-track direction)

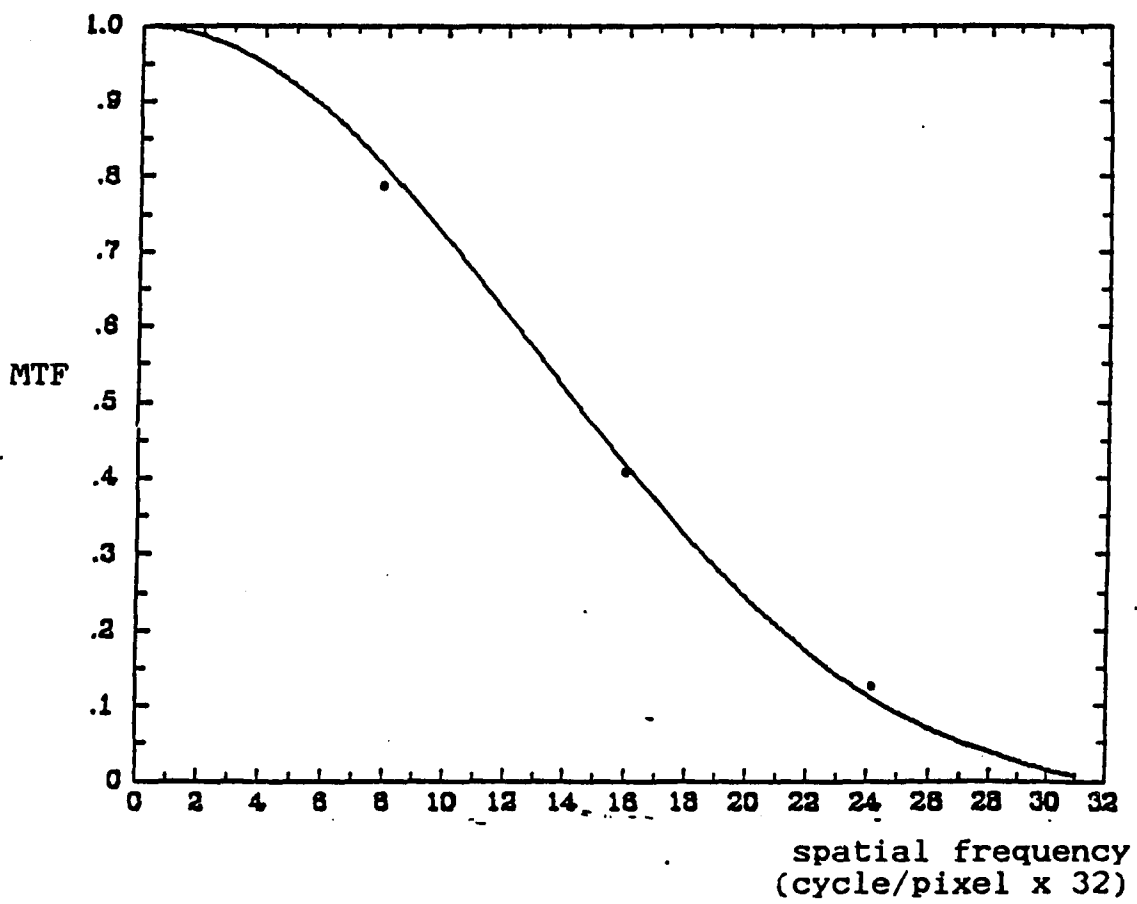


Fig.3.16 Overall system TF in band 1
(along-track direction)

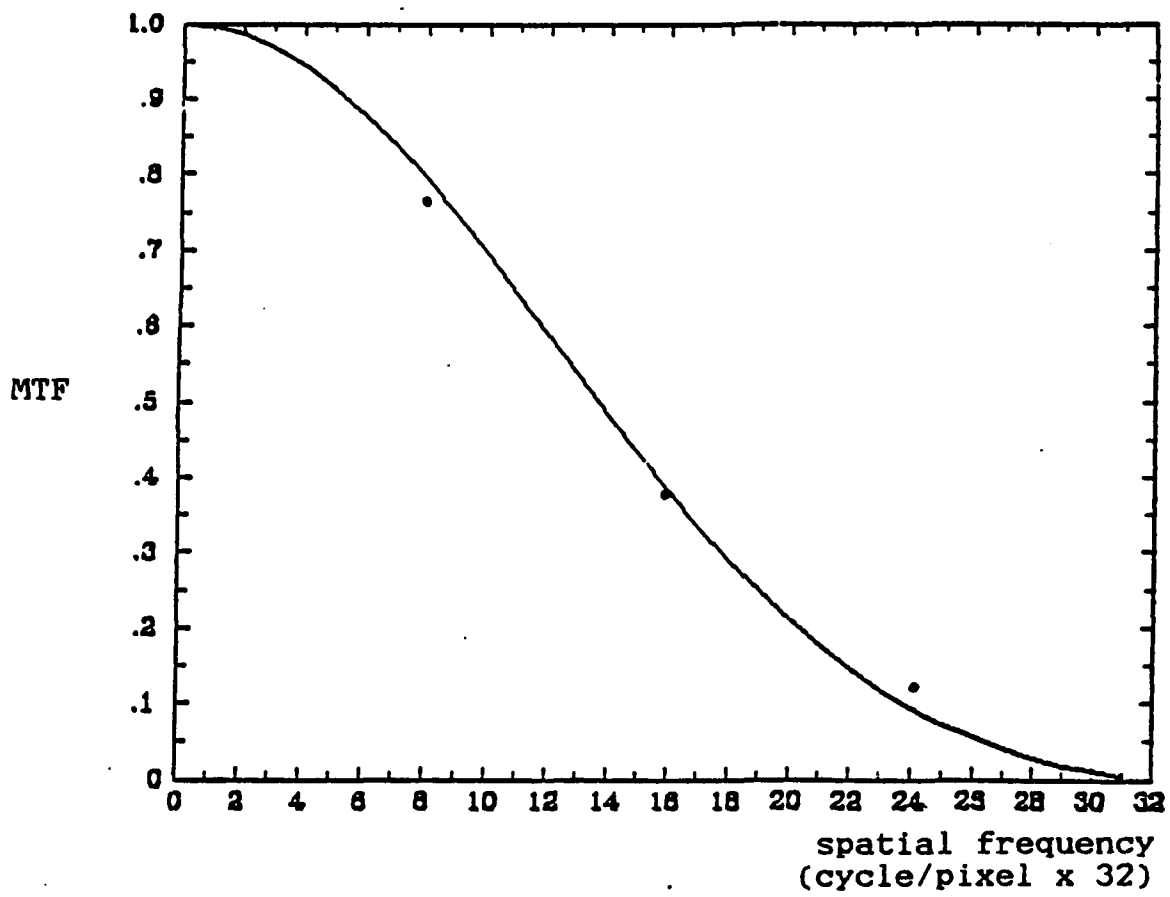


Fig.3.17 Overall system TF in band 2
(along-track direction)

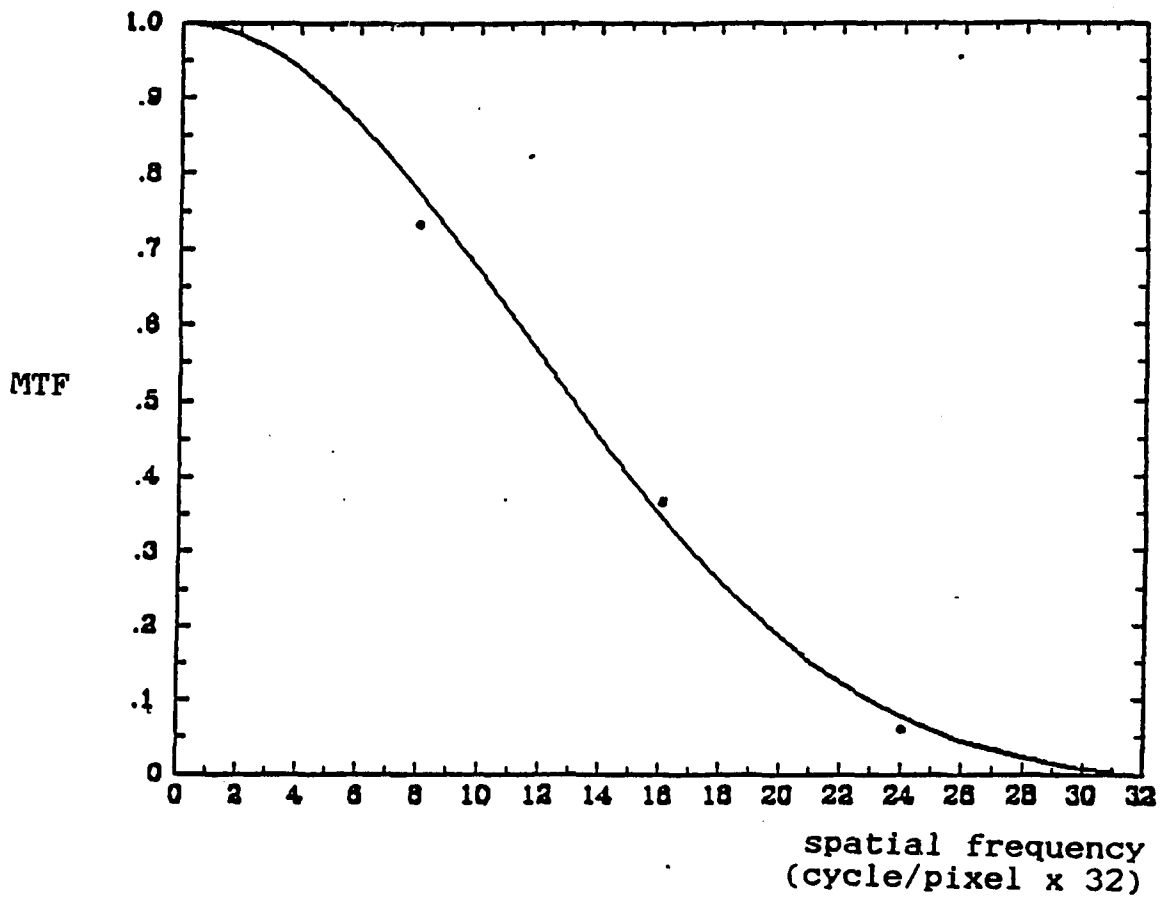


Fig.3.18: Overall system TF in band 3
(along-track direction)

MTF values indicated at $fc/4$, $fc/2$, and $3fc/4$ from Leory (1987).

A comparison of the MTF among TM, MSS, AVHRR and SPOT systems (multispectral band 1) on a normalized frequency scale is shown in Fig.3.19. and Fig.3.20. In the across-track direction, SPOT has the highest overall MTF, resulting from its high electronic filter TF. However, in the along-track direction SPOT has the lowest overall MTF due to the significant effect of integration time.

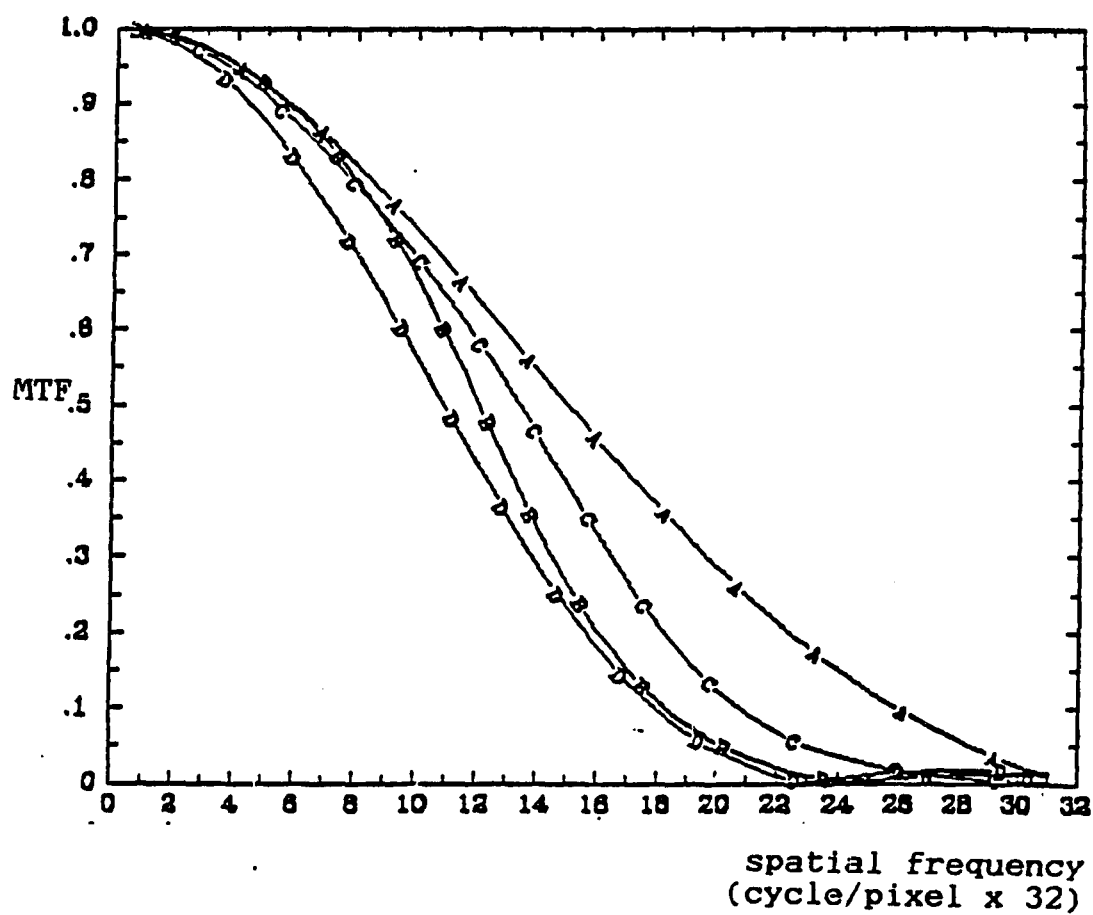


Fig.3.19 Overall system TFs for different systems (across-track direction). A-SPOT B-MSS C-TM D-AVHRR

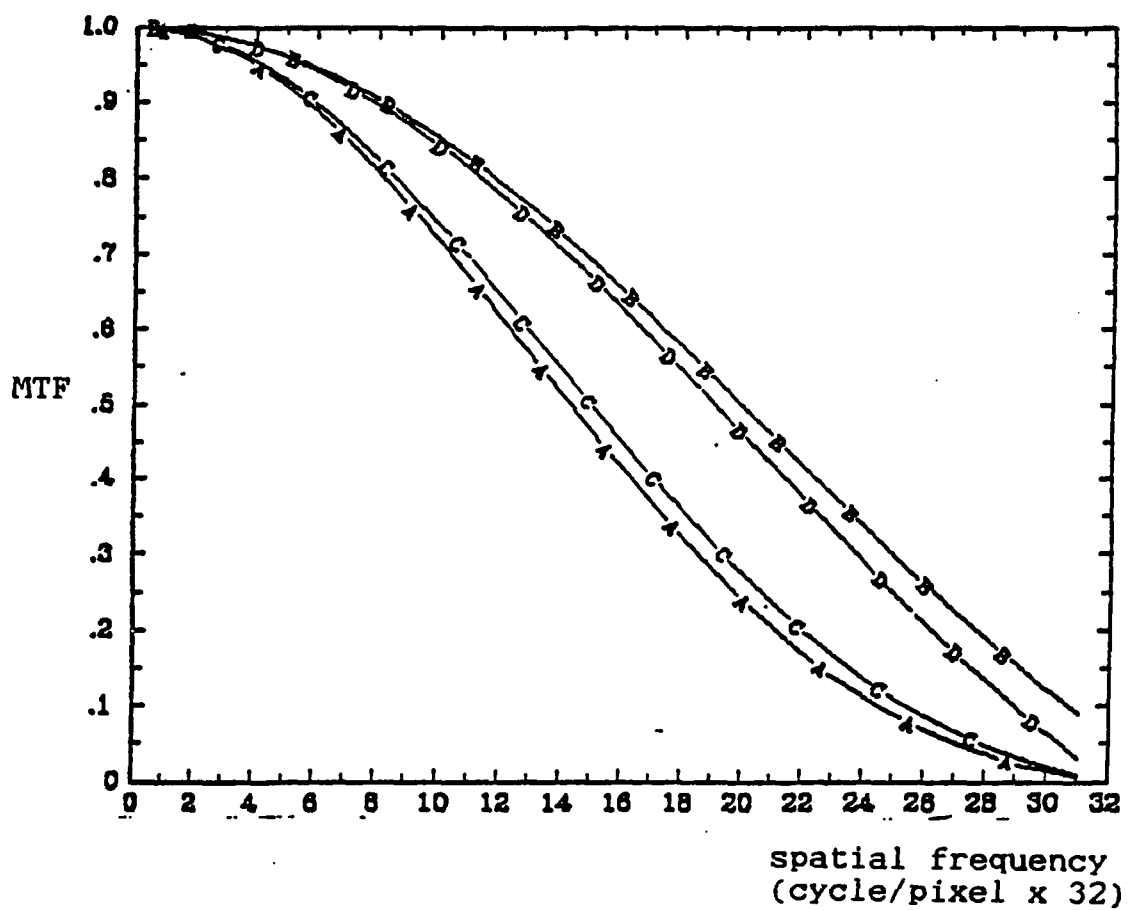


Fig.3.20 Overall system TFs for different systems (along-track direction). A-SPOT B-MSS C-TM D-AVHRR

Chapter 4

IMAGE SAMPLING AND RESTORATION

When a scene is recorded by an imaging device certain degradations are inevitable. These degradations may be caused by a number of sources, including motion blurring, atmospheric interference, imperfect optics and electronic filters, etc. Image restoration is an attempt to correct or compensate for degrading phenomena that blur an image.

4.1 Image Sampling and Restoration Systems

In Chapter 3 a typical imaging, sampling and reconstruction system was illustrated to demonstrate the essential subsystems in image formation and restoration (Fig.3.3). The sampling and restoration subsystem components will be discussed in this chapter.

4.1.1 Sampling subsystem

Typically, the processed image is sampled and digitized for digital transmission or storage prior to image restoration. The continuous image $g(x,y)$ created by the imaging subsystem, enters the sampling subsystem, which is between the continuous output of the imaging subsystem and the discrete input to the restoration subsystem. Mathematically, image sampling is done by

multiplying the output of the imaging subsystem by the two-dimensional comb function

$$\text{comb}(x,y) = \sum_{m=-\infty}^{\infty} \sum_{n=-\infty}^{\infty} \delta(x-m,y-n) \quad (4.1)$$

where the notation indicates that the double sum is over all (positive, zero, and negative) integers m,n , and it is assumed that sampling occurs on an equally-spaced rectangular grid. Fig.4.1 shows the function of eqn.(4.1). The arrow at each corner of the rectangular grid represents a delta function with unit height.

4.1.2 Restoration subsystem

The final output of the system in Fig.3.3 is a continuous restored image $f_m(x,y)$ which is formed by the spatial convolution of the discrete sampled image $g_s(x,y)$ with the restoration function $m(x,y)$. One objective of digital image restoration is to design $m(x,y)$ so that the restored image $f_m(x,y;u,v)$ is a radiometrically accurate reproduction of the original scene $f(x-u,y-v)$.

The relation of sampled image to restored image is

$$f_m(x,y;u,v) = m(x,y)*g_s(x,y;u,v) \quad (4.2)$$

4.2 The Linear Inverse and Wiener Filters

For the continuous optical image, we have

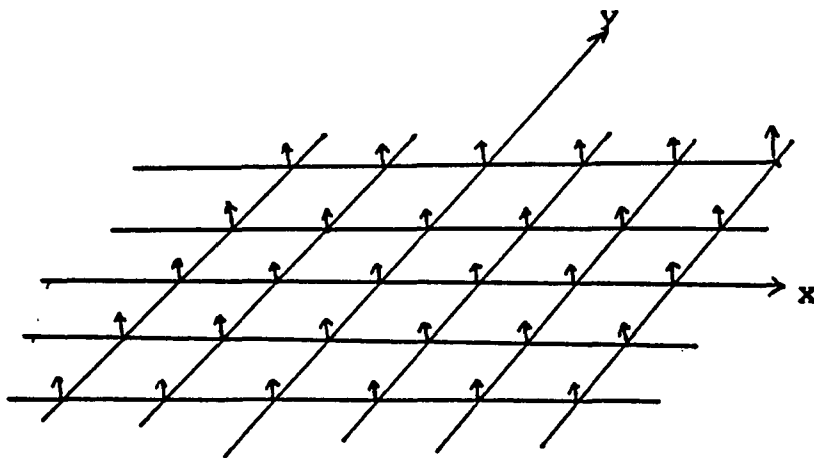


Fig.4.1 A 2-D comb function

$$g(x,y) = h(x,y)*f(x,y) \quad (4.3)$$

Taking the Fourier transform of both sides of eqn.(4.3), we have

$$G(u,v) = H(u,v) \cdot F(u,v) \quad (4.4)$$

where $G, H,$ and F are the Fourier transforms of g, h and f respectively and u, v are the frequency domain coordinates corresponding to x and y . $H(u, v)$ is called the "transfer function", or TF, and describes how well the imaging system transfers modulus and phase information at different spatial frequencies. Remember that for our system modeling, $H(u, v)$ can be modeled in separate directions (across- or along- track). Hence, $H(u, v)$ can be modeled as $H(u)H(v)$. The separability property can be extended to the restoration function if certain requirements are satisfied (Wood, 1986).

If the transfer function $H(u, v)$ were known, for example, from system modeling, then one could in theory, recover $f(x, y)$ exactly by dividing eqn.(4.4) by $H(u, v)$ (ignoring the sampling effect caused by the sampling subsystem) and then taking the inverse Fourier transform, resulting in

$$f(x,y) = F^{-1}\{G(u,v)/H(u,v)\} \quad (4.5)$$

The term $1/H(u,v)$ is called an "inverse filter", which is the Fourier transform of the restoration function without the sampling effect. However, $F(u,v)$ may not be stable in the sense that if $H(u,v)$ is zero, the above expression is undefined. In practice, this restoration method does not work well because it ignores noise in the imaging system. Noise may be introduced in a signal in a number of ways, but in this chapter additive noise is considered, because it is simple to model and leads to the standard Wiener filter. Moreover, for low noise levels, additive noise is a good model for most images. For additive signal-independent noise, the image equation would be

$$g(x,y) = h(x,y)*f(x,y)+n(x,y) \quad (4.6)$$

where $n(x,y)$ represents signal-independent additive noise.

Where such a term is present, the inverse filter becomes

$$f(x,y) = F^{-1}\{G(u,v)/H(u,v)-N(u,v)/H(u,v)\} \quad (4.7)$$

Problems still exist if $H(u,v)$ is very small (usually at high frequencies). Thus, the noise component dominates the restored image at high frequencies. As a result, inverse filtering is not a very effective image

restoration method. A better solution to this problem is Wiener filtering, which takes into account the noise process. Simple zero mean, image independent and additive noise is assumed. The Wiener filtering procedure is based on minimizing the mean square error between the original scene and the restored image (estimated scene)

$$E\{[f(x,y)-f_m(x,y)]^2\} \quad (4.8)$$

where $f_m(x,y)$ is the restored image. In the Wiener filter, the power spectrum of the noise and the scene must be known. This is possible if the image is assumed to belong to a kind of stochastic process that must be at least wide-sense stationary. Generally, the global mean $E[f(x,y)]$ may not give us much information about local contrast (Helstrom, 1966). Therefore, the deviation eqn.4.9. is of interest in our restoration,

$$f_n(x,y) = f(x,y) - E[f(x,y)] \quad (4.9)$$

E denotes an expected value of the original scene radiance. The independent, zero-mean, stationary, stochastic processes $f_n(x,y)$ and $n(x,y)$ are characterized by their spatial covariance functions.

$$R_{f_n}(x,y) = E[f_n(x,y)f_n(x+x',y+y')] \quad (4.10)$$

$$R_n(x,y) = E[n(x,y)n(x+x',y+y')] \quad (4.11)$$

or by the Fourier transforms of these, $S_{fn}(w)$ and $S_n(w)$, which are the spatial spectral densities of the image and noise processes, respectively. Derivation of the Wiener filter was presented by C.W.Helstrom (1966) in a classical approach. The Wiener restoration filter is given by

$$M(u,v) = H^*(u,v) / [|H(u,v)|^2 + S_n(u,v) / S_{fn}(u,v)] \quad (4.12)$$

or

$$M(u,v) = 1/H(u,v) \{ |H(u,v)|^2 / [|H(u,v)|^2 + S_n(u,v) / S_{fn}(u,v)] \}$$

= inverse filter x modifier filter (4.13)

where $S_n(u,v)$ is the power spectrum of the additive noise, $S_{fn}(u,v)$ is the power spectrum of the original scene. $H(u,v)$ denotes the Fourier transform of the imaging system point spread function. $H^*(u,v)$ is the conjugate of $H(u,v)$.

Note the second term in the denominator of eqn.(4.13) is the reciprocal of the signal-to-noise ratio (SNR) at various frequencies. Equation (4.13) solves the inverse filter's infinity and noise amplification problem. When a component of $H(u,v)$ is zero, the second term in the denominator of eqn.(4.13) ensures that the solution does not go to infinity. This term also makes the Wiener

filter an inverse filter when the SNR is high at a specific frequency. At frequencies where the SNR is weak, this term dominates, giving the restoration process protection from noise amplification.

4.2.1 Scene autocorrelation Model

Implementation of the Wiener filter given by eqn.(4.13) requires knowledge of the scene and noise power spectra $S_f(u,v)$ and $S_n(u,v)$. The imaging system transfer function $H(u,v)$ is assumed to be known at this stage. For example, we may derive it by system modeling as in Chapter 3. The measurement and modeling of $S_n(u,v)$ and $S_f(u,v)$ will be discussed below.

Signal autocorrelation model

A simple mathematical model of an image consists of a sequence of rectangular pulses of randomly determined height (corresponding to pixel grey levels) and random duration (corresponding to the size of objects in the image). For such a model it can be shown (Papoulis, 1984) that the corresponding autocovariance function is of the form of a first order Markov model which is given by

$$R(x,y) = \text{var} \exp(-\sqrt{a^2 x^2 + b^2 y^2}) \quad (4.14)$$

The first order Markov function is rotationally symmetric, but not separable. For reasons of

computational efficiency and mathematical tractability the Markov process is often assumed to be separable of the form

$$R(x,y) = \text{var} \text{EXP}(-a|x|-b|y|) \quad (4.15)$$

where $1/a$ and $1/b$ are the data correlation half-widths in the two orthogonal directions used in our restoration modeling and var is the variance of the scene. Transforming the autocovariance to the frequency domain, we have

$$S_{fn}(u,v) = S(u)S(v) = 4ab\text{var} / [(a^2 + (2\pi u)^2)(b^2 + (2\pi v)^2)] \quad (4.16)$$

which is also separable.

4.2.2 Noise power spectrum

A major contributor of noise in CCD imaging systems is random thermal noise (dark-current noise) which adds into the incoming signal. Thermal noise is usually described by a zero-mean Gaussian probability density function with a uniform ("white") power spectrum (Davenport, 1958), so called because the contribution to the variance is the same at any frequency, or "white". In practice, it is sufficient for the noise to be white over the region of interest, from zero frequency up to the folding or Nyquist frequency.

Furthermore, it can be shown (Papoulis, 1984) that the area under the power spectrum of a signal, i.e., its total power, is equal to the variance of the corresponding signal for a zero mean random process. For the noise power spectrum, then, we have assumed white Gaussian noise with a variance of one grey level, which approximates the noise level in SPOT images,

$$S_n(u,v) = \sigma_n^2 = 1. \quad (4.17)$$

4.3 The effect of Sampling

The importance of including the effects of sampling in the system analysis was pointed out by Park, et.al. (1984) in a study of sampling effects for the Landsat MSS imaging system. It was shown that the effect of sampling is to increase the average amount of blurring in the image. Fortunately, the goal of the Wiener filter is to boost those frequencies which correspond to fine detail and have been suppressed by the low pass filtering effect of the system transfer function or sampling effect. The Wiener filter would enhance the detail even more if the sampling effect is included in the system transfer function. However, sampled systems are not shift-invariant, and a different model has to be used to deal with this phenomenon. The output of a sampled system resulting from a point-source input will depend not only

on the intensity of the point-source but also on its location with respect to the sampling grid. This "sample-scene phasing" has an important effect on the derivation of the system's transfer function. The mathematical function describing sampling cannot be simply cascaded with other system element transfer functions to produce an overall system transfer function, because the process of cascading transfer functions depends on the assumption of linearity and shift-invariance of each system component.

One way of dealing with this sampling phenomenon is a stochastic approach (Park, et.al., 1984) in which sampling effects are accounted for by assuming a random distribution of point-sources. This results in an average system TF (ASTF) or in the spatial domain, an average system PSF (ASPSF). These quantities are averaged over all possible sample-scene phases.

The procedure used by Park, et.al., is to derive a shift-variant sampled system point-spread function (SSPSF) of the form

$$\text{SSPSF}(x,y;u,v) = h(x-u,y-v) \sum_{m=-\infty}^{\infty} \sum_{n=-\infty}^{\infty} \delta(x-m,y-n) \quad (4.18)$$

The point spread function, $h(x,y)$, represents a continuous image formation system whose output from a

point-source input depends only on the intensity of the point-source and not on its location in the object plane. The double sum notation is to include the sampling effect and causes the SPSF to lose the overall system shift-invariance properties. The output of a point-source input now depends on its intensity and location.

Parameters u and v locate the point-source with respect to the sampling grid. If u and v are assumed to be random variables having a uniform distribution, which means a point-source is equally likely to be located anywhere with respect to the sampling grid, then an average system point-spread function (ASPSF) can be found (Park, et.al., 1984). The ASPSF has the following form

$$\text{ASPSF}(x,y) = \iint_{-\infty}^{\infty} \text{SPSF}(s,y;u,v) du dv \quad (4.19)$$

The sampling effect has been accounted for in our system modeling with $\text{ASPSF}(x,y)$ substituted for $h(x,y)$ in eqn.(4.6) and $\text{ASTF}(u,v)$ substituted for $H(u,v)$ in the Wiener filter eqn.(4.13).

4.4 Restoration Kernel Window

We desire to use the Wiener filter as the restoration filter but implement it in the spatial domain to allow efficient processing of large images and use of the restoration kernel as a resampling kernel for geometric

correction. Before processing an image spatially, a restoration LSF (RLSF) must be derived by an inverse Fourier transform of the Wiener filter. However, the resulting restoration LSF (RLSF), has sidelobes caused by the abrupt drop of the Wiener filter at 0.5 cycles/pixel, which, if applied directly to an image, would result visually in ringing at object edges and in noise enhancement. Therefore a window is applied to the RLSF so as to minimize the sidelobes without distorting the main lobe. A trade-off exists, as any decrease in the sidelobes, while reducing ringing and noise enhancement, will also reduce the amount of restoration obtainable. Many criteria have been proposed to choose the proper window (L. Wood, 1986). One of these may be maximizing the integrated power ratio of the restoration filter below 0.5 cycles per pixel to that above 0.5 cycles per pixel. This has the effect of minimizing ringing and noise enhancement in the spatial domain while maximizing the restoration achieved.

Windowing is a multiplication in the spatial domain, equivalent to convolution in the frequency domain. If the spatial window is too abrupt, then in the frequency domain the result will have Gibbs phenomenon in which there is significant overshoot or undershoot at high

frequencies. On the other hand, if the window is too smooth, there will be a loss of power at all frequencies resulting in a loss of restoration in the restored image. A reasonable compromise is the Hanning window (F. J. Harris, 1978),

$$w(t) = \begin{cases} 1/2 (1 + \cos \pi t/L) & |t| < L \\ 0 & \text{otherwise} \end{cases} \quad (4.20)$$

where L is the half-width of the window or kernel. A discussion of testing to optimize L is included in the next chapter.

CHAPTER 5

SYSTEM PERFORMANCE TESTING

With a thorough discussion of imaging, sampling and restoration subsystems in previous chapters, this chapter is focused on system performance testing. The impact of variations in parameters on the restoration line spread function (RLSF) are examined here, such as the sensitivity of the RLSF to spatial windowing.

5.1 Frequency Increment and Sampling Interval

In our system simulation, a discrete form of the Wiener filter is derived first. The RLSF of the system is obtained by inverse Fourier transform of the Wiener transfer function (eqn.(4.13)). The RLSF is used to process an image to create a restored image, which should be radiometrically close to the original scene. Thus, in order to have an accurate RLSF for our restoration, the spatial interval should be small and contain most of the information on the RLSF in a discrete form. Basically, the spatial interval is affected by choosing the number of points and frequency interval in the frequency domain. as follows.

We have a sequence of transfer function values $[X_m]$ with N points in one dimension. The inverse discrete Fourier transform (DFT) is used to transfer this ordered sequence of data from the frequency domain to the spatial domain. The formula for the inverse DFT is

$$X_k = 1/N \sum_{m=0}^{N-1} X_m \cdot \text{EXP}[i(2\pi km/N)] \quad ; k = 0, 1, \dots, N-1 \quad (5.1)$$

In general, $[X_k]$ is real which results in the other $N/2$ points of $[X_m]$ with

$$X_{N-m} = X_m^* \quad (5.2)$$

Notation $*$ is the conjugate in this case. Therefore, if $[X_k]$ is real, we may have N points simply by finding the conjugate of the first $N/2+1$ points. This is exactly the situation that we have in our modeling. Thus far, we know N points of complex $[X_m]$ gives N points of real data $[X_k]$. Nothing has been said about the resolution of the sequence $[X_m]$.

If we have 1024 points in the system transfer function, there will be 1024 points in the SLSF. However, this number is misleading. Since the SLSF has a kernel size of four pixels; if the spatial interval is $1/16$ pixel, it will have $1024 - 4 \times 16 = 960$ points equal to zero. Kernel size is defined as the width of non-zero data

values. These zero points do not contribute to the requirement of accuracy. However, if we decrease the spatial interval $1/32$ to $1/64$, non-zero points may increase from 128 to 256 points, thereby increasing the spatial resolution. Even though it is reasonable to have smaller values like $1/32$, $1/64$ or $1/128$ for the spatial interval, they are not used because the frequency increment would be affected. For example, Fig.5.1 shows the SLSF of the SPOT system in the panchromatic band with kernel size equal to 128 points or four pixels with the spatial interval at $1/32$ pixel. If $1/256$ is used, the total number of pixels shown in Fig.5.1 would be equal to $1024/256 = 4$. In other words, the frequency increment will be $1/4$ cycles/pixel on a normalized scale (Fig.5.2). The system TF has the property that it drops to zero after 1 cycle/pixel. Hence, for fixed N, a small spatial increment leads to a large frequency interval. A reasonable compromise value is chosen, which is $1/32$ for frequency and spatial intervals and N of 1024. These values lead to both a reasonably high frequency and spatial resolution.

5.2 Autocorrelation and Power Spectrum of Scene

As we have discussed in Chapter 4, the autocorrelation function is modeled as

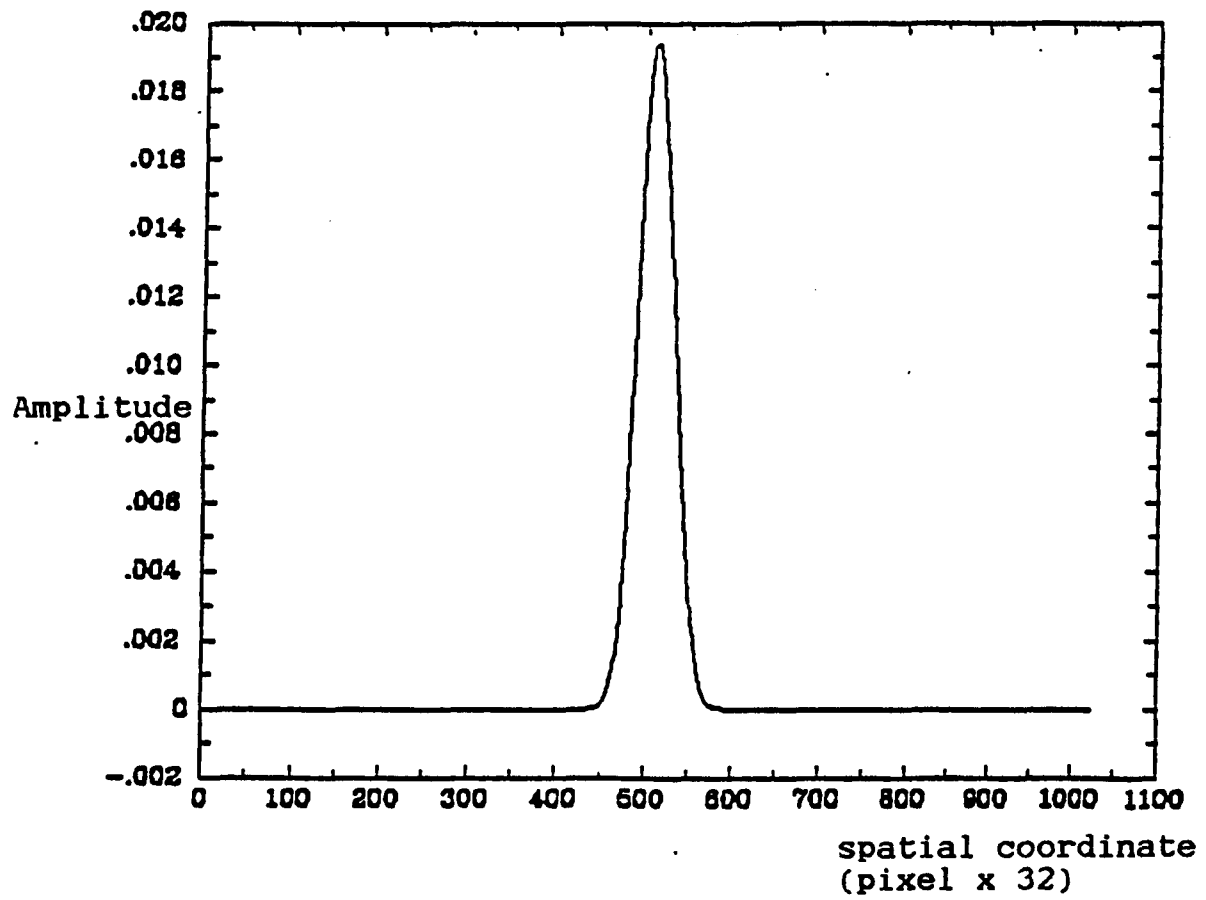
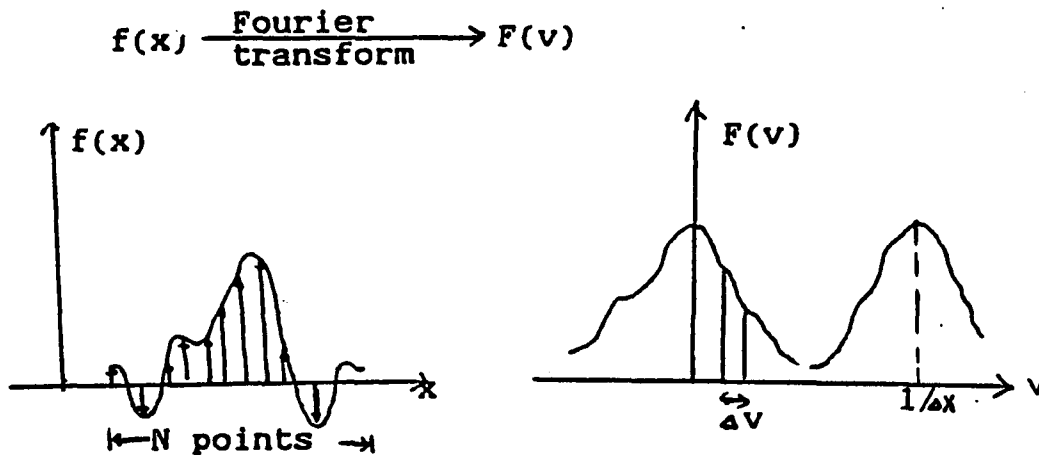


Fig. 5.1 The SLSF (Pan. along-track direction)



Sampling interval = Δx frequency increment = Δv

$$1/N \cdot \Delta x = \Delta v$$

Fig.5.2 Illustration of the relationship between sampling interval and frequency increment of a signal

$$R(x,y) = \text{var} \text{EXP}[-a|x|-b|y|] \quad (5.3)$$

and the power spectrum of a scene, therefore, has the following form

$$S(u,v) = S(u)S(v) = 4ab\text{var} / [(a^2 + (2\pi u)^2)(b^2 + (2\pi v)^2)] \quad (5.4)$$

which is separable. This is put into the Wiener filter transfer function in order to obtain the restoration function. The equation of the Wiener filter is

$$M(u,v) = 1/H(u,v) \{ |H(u,v)|^2 / [|H(u,v)|^2 + S_n(u,v)/S_f(u,v)] \} \quad (5.5)$$

In eqn.(5.5), because the system transfer function $H(u,v)$ and power spectrum of the noise $S_n(u,v)$ are fixed, the remaining parameters are contained in the power spectrum of the scene $S_f(u,v)$. They are the variance of the scene, var , and the half-width of the autocorrelation, $1/a$ or $1/b$. In the following, we will show how to find the half-width of an autocorrelation function of a scene and the sensitivity of the Wiener filter transfer function to variations of these parameters.

5.2.1 Measurement of the autocorrelation function

We calculated an autocorrelation function for a portion of the SPOT Phoenix image (128 pixels by 128

lines) in the panchromatic band. The autocorrelation data in the across track direction is shown in Fig.5.3. By adjusting the parameters a or b in eqn.(5.3), we have a family of exponential functions with different widths. The best fit is done by selecting the value for a or b that results in the minimum square error between the supposed exponential function and the experimental curve. However, this value is the autocorrelation half-width of the image, not the original scene.

By using a stochastic model (Papoulis, 1984), the power spectrum $S_x(u)$ of a stationary input x and power spectrum $S_y(u)$ of the output y are related as

$$S_y(u) = S_x(u) \cdot |H(u)|^2 \quad (5.6)$$

Alternatively, we can express eqn.(5.6) in terms of the respective autocorrelation functions,

$$R_{yy}(T) = R_{xx}(T) * R_{hh}(T) \quad (5.7)$$

where $R_{xx}(T)$, $R_{yy}(T)$ and $R_{hh}(T)$ are the autocorrelation functions of the input, output and impulse responses respectively.

Typically, $R_{yy}(T)$ has the form of a decaying exponential function as we notice in eqn.(5.3). According to the convolution principle, the width of

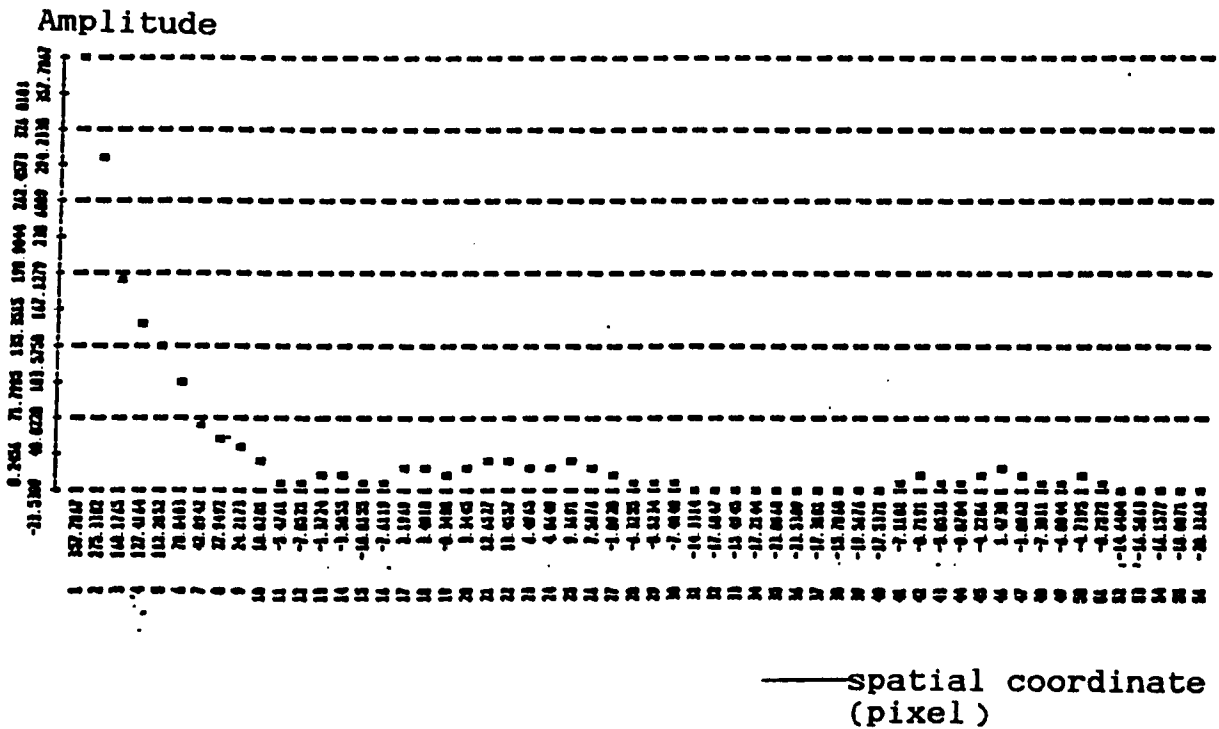


Fig.5.3 The autocorrelation function of a SPOT image (Phoenix)

$R_{yy}(T)$ is the sum of $R_{xx}(T)$ and $R_{hh}(T)$. However, the autocorrelation of the sensor impulse response has a narrow width compared to $R_{xx}(T)$. Therefore, regardless of the shape of $R_{hh}(T)$, $R_{xx}(T)$ is assumed to have a similar form as $R_{yy}(T)$ but with a different half-width, equal to the half-width difference of $R_{yy}(T)$ and $R_{hh}(T)$. Fig.5.4 is the autocorrelation function of the SPOT panchromatic SLSF in the across-track direction, which has a half-width equal to 1.2 pixels. To indicate how the autocorrelation function varies across an image, a 512X512 pixel image was used, divided into 16 areas, each of size 128X128. The half-width of the autocorrelation function of each area was then found and tabulated in Table 5.1. The average image autocorrelation half-width is 4.18 pixels resulting in an average scene half-width of about 3 pixels. Note that the half-width in the image varies from 1.85 to 8.33 pixels.

5.2.2 Effects of parameters on Wiener filter equation

As we have discussed above, the variance and half-width (HW) of the power spectrum of the scene are the only free parameters that have an impact on the Wiener filter. In this section, the effect of changes in the variance and HW of the scene power spectrum on the Wiener filter TF are studied.

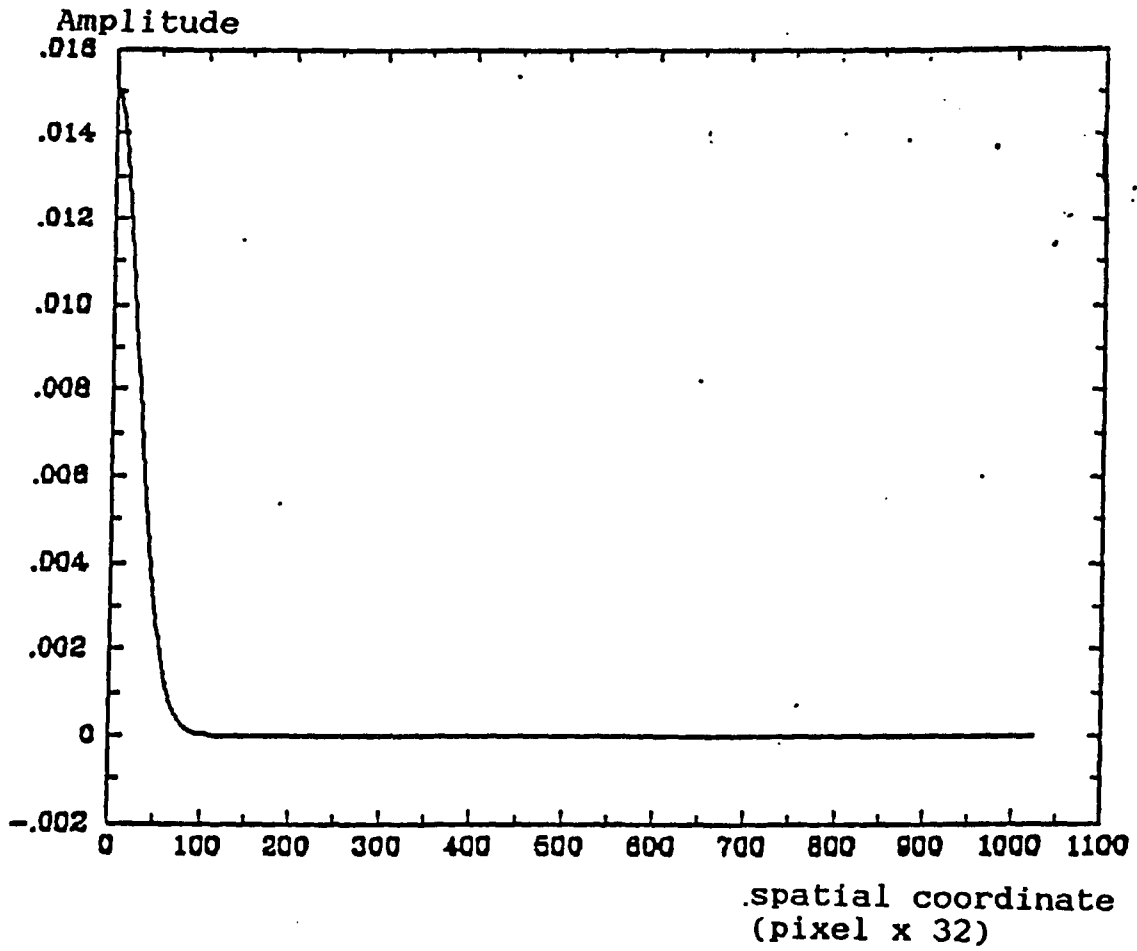


Fig.5.4 The autocorrelation function of SLSF (Pan, across-track direction)

Table 5.1 The variations of the autocorrelation HW across a SPOT image (Phoenix, 512X512). The whole area is divided into sixteen 128X128 segments with starting co-ordinate(pixel,line) shown above.

(1,1) 6.25	(129,1) 2.78	(257,1) 8.33	(385,1) 5.0
(1,129) 3.85	(129,129) 2.27	(257,129) 5.0	(385,129) 6.25
(1,257) 3.13	(129,257) 1.85	(257,257) 1.85	(385,257) 6.25
(1,385) 2.63	(129,385) 3.85	(257,385) 2.63	(385,385) 5.0

Average HW = 4.18 pixels

First, the HW was fixed and the variance was increased from 25 to 625, which is the range that we find in SPOT images. In Fig.5.5 the Wiener filter TF amplitude increases as the variance increases. This phenomenon can be explained by eqn.5.5. As the variance increases, the SNR increases, leading in the limit to the inverse filter as expected. Second, the variance is fixed but this time the HW was changed from one to nine, which is also the range that we found in the Phoenix image. Fig.5.6 shows that if the HW increases, the Wiener filter TF decreases. Therefore, if an image has a low autocorrelation HW and high variance power spectrum, the Wiener filter TF would be nearly the inverse filter and the RLSF will enhance high frequencies components in the image.

5.3 Windowing

The expected Wiener filter TF has the form shown in Figs.5.5, 5.6 from zero to half of the sampling frequency (0.5 cycles/pixel). Beyond 0.5 cycles/pixel, it has zero response so that aliasing does not appear. However, due to this abrupt cut-off, the restored line spread function (RLSF) will have oscillations (Gibb's phenomenon) as shown in Fig.5.7, which would induce some artifacts in the restored image.

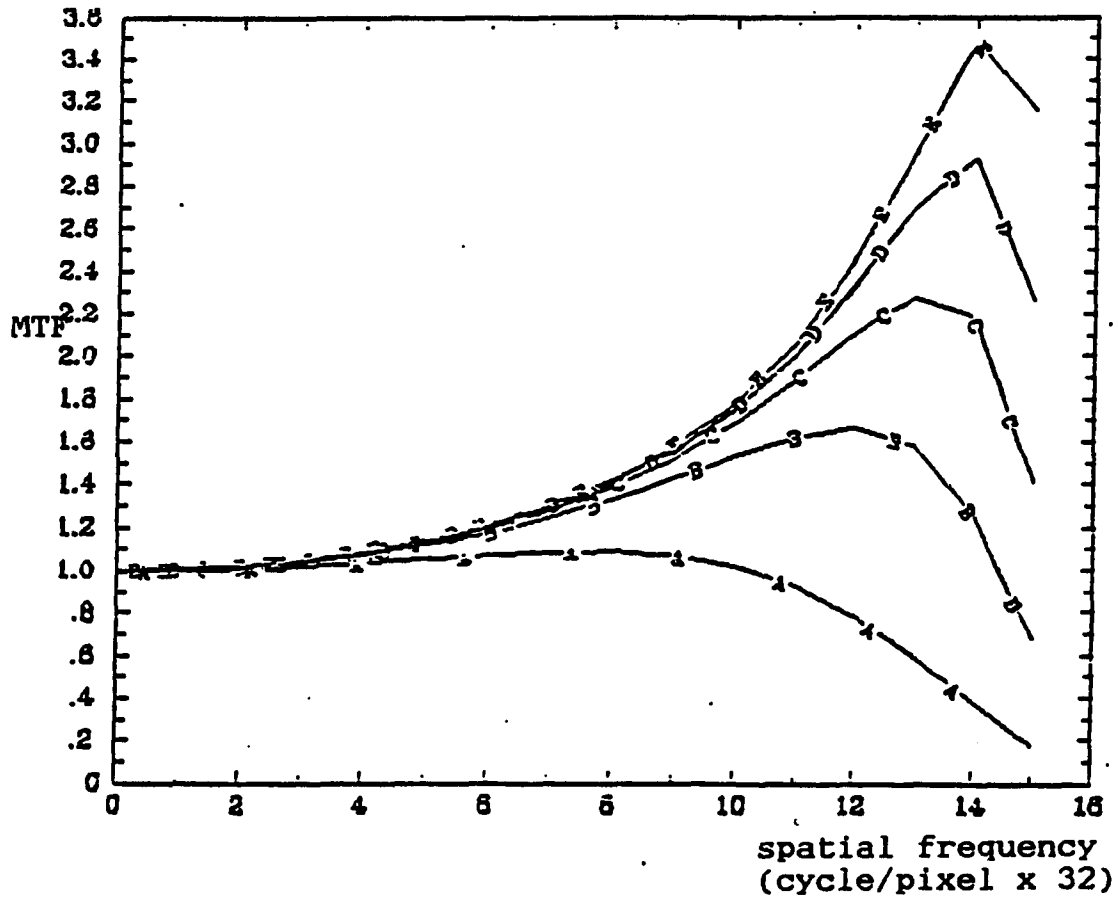


Fig.5.5 The changes of restoration TF caused by the variations of the variance. A-variance = 25, B-variance = 100, C-variance = 225, D-variance = 400, E-variance = 625.

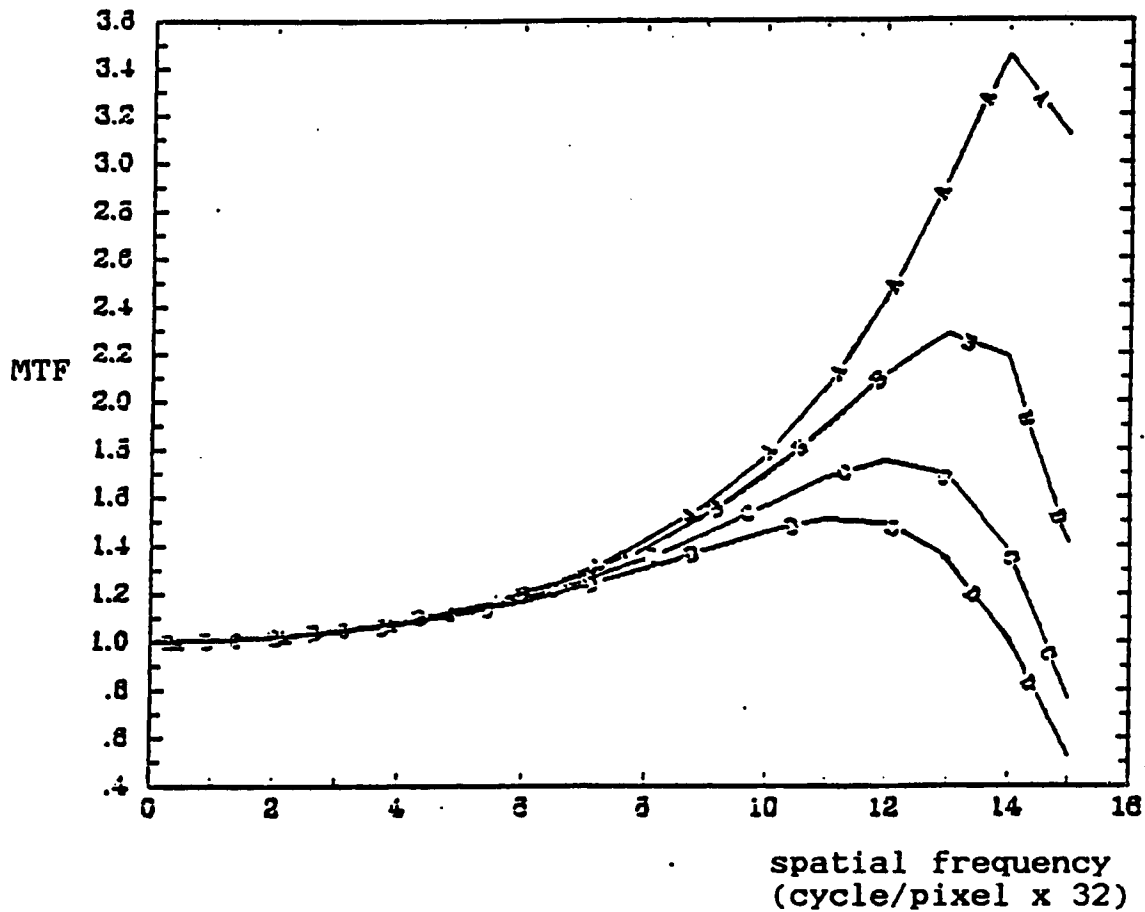


Fig.5.6 The changes of restoration TF caused by the variations of the HW of the autocorrelation function. A-HW = 1, B-HW = 3, C-HW = 6, D-HW = 9.

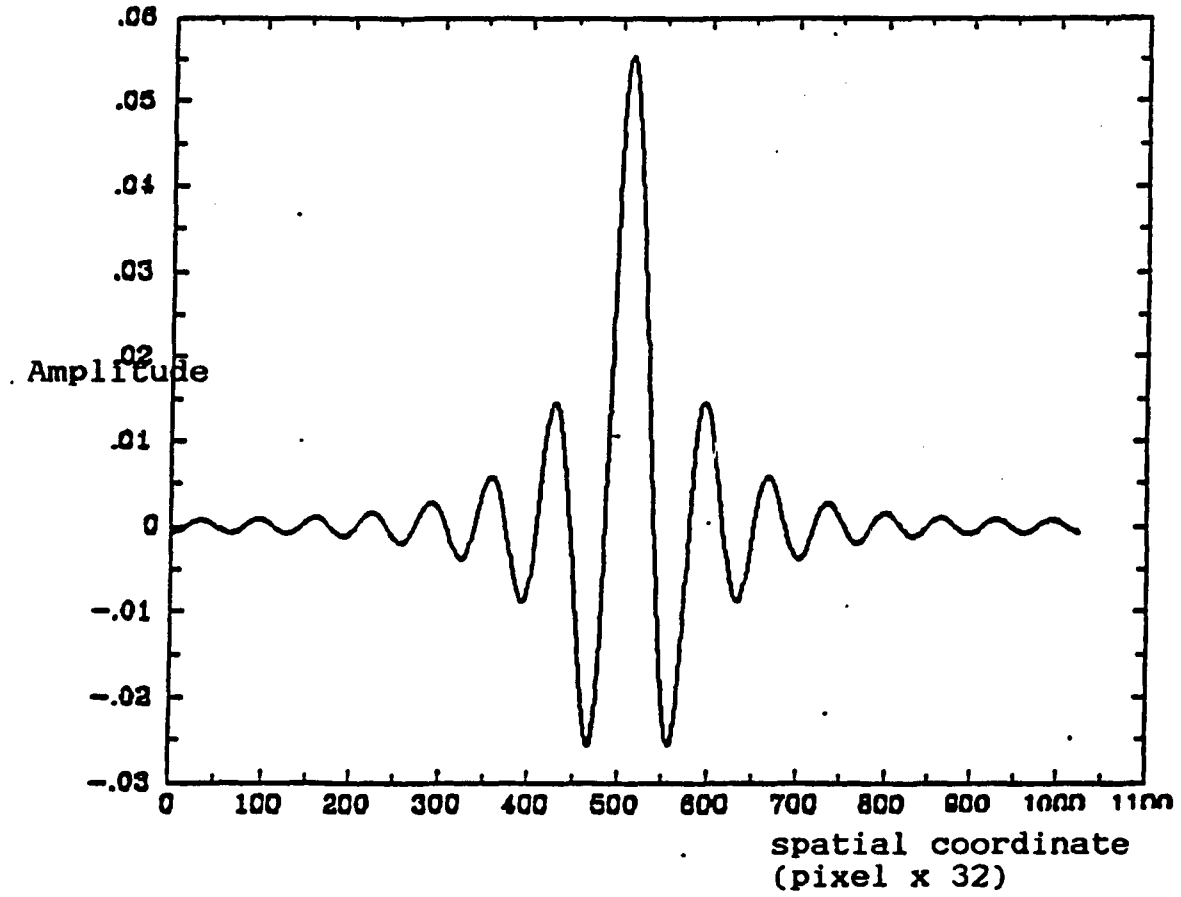


Fig. 5.7 The RLSF (Pan, along-track direction) without windowing

Therefore, a spatial window multiplied with the RLSF is used to smooth the Wiener filter. However, the smearing effect of windowing on the Wiener transfer function results in added high frequency information above 0.5 cycles/pixel. This drawback requires us to select the window carefully. There are several criteria to help us choose the best performance window. One is to smooth the abrupt drop at 0.5 cycles/pixel as well as reduce the added on high frequency components. A Hanning window, which has the following form

$$w(t) = \begin{cases} 1/2 (1 + \cos(2\pi t/L)) & |t| < L \\ 0 & \text{otherwise} \end{cases} \quad (5.8)$$

where L is the half-width of window, is a common choice (L. Wood, 1986). A method of finding the best value of L is to find the power above and below 0.5 cycles/pixel for different values of L , using an edge image as a simulation. Fig.5.8 shows the Wiener filter TF after windowing and Table 5.2 shows the change in power obtained by varying the kernel size. Delta is the slope of the restored edge, which remains fairly constant above a kernel size of six or seven pixels.

5.4 Edge Simulation and Resampling

Sometimes, the sampling phases in conversion of a continuous to discrete image must be considered. For

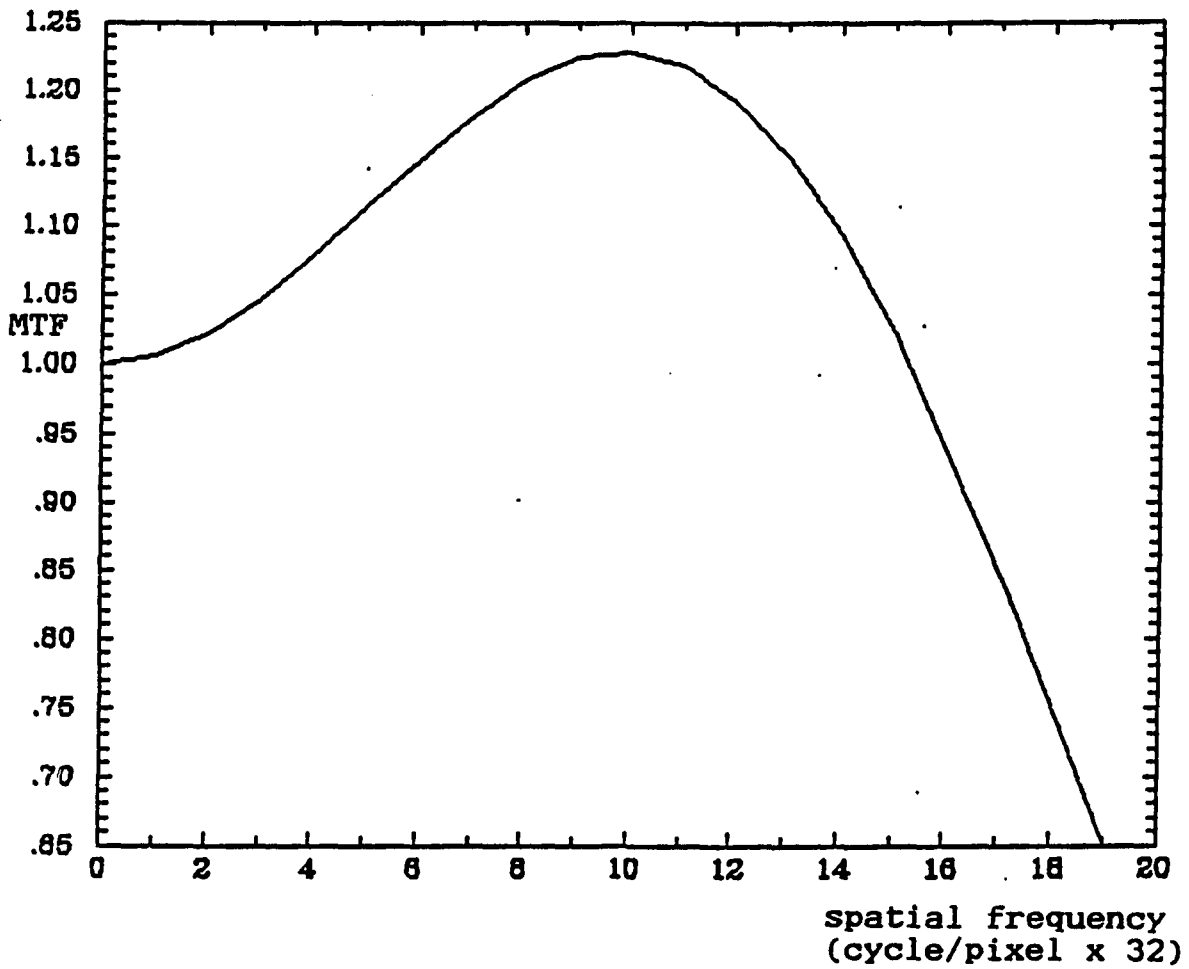


Fig.5.8 The restoration TF with windowing (Pan, along-track direction)

Table 5.2 The changes in power of the restoration TF by varying the kernel size of window.

Kernel size of window	power below 0.5 cyc/pix (a)	power above 0.5 cyc/pix (b)	b/(a+b)	delta
3	14.34	6.76	0.32	-
5	17.93	5.4	0.23	0.09
7	25.08	5.37	0.176	0.054
9	26.9	4.4	0.141	0.035
11	28.68	3.73	0.115	0.025
13	29.53	3.16	0.097	0.018

delta is the decrement in column 4.

instance, taking pictures of the same earth scene from a satellite at different times will introduce different phases. The phase will always be within $\pm 1/2$ pixel. In other cases, the sampling phases are introduced in pixel resampling or interpolation for compensation of geometric distortions. If an image is required to be reduced by a factor of four, the digitized image must be subsampled every four points. In this subsampling, several questions are raised. Which pixel do we start subsampling first? Does it have any effect on the restored image by varying phase sampling? To what extent does it effect the restored image? Those questions are addressed by the following experiment using edge image simulation.

The procedure for image simulation is explained in the block diagram in Fig.5.9. First, a scene must have certain features that are helpful for our analysis. We choose a scene with high contrast in GL and high spatial frequency content. A scene suiting our requirement is one-dimensional edge, 1×1024 points, with GL of 50 and 90. The edge is located at the center of the array, (Fig.5.10). Even though the scene is discrete, we would say it is continuous in the sense that it has high resolution, i.e. Δx is small relative to the SPOT LSF. A SPOT panchromatic band system line spread function (SLSF)

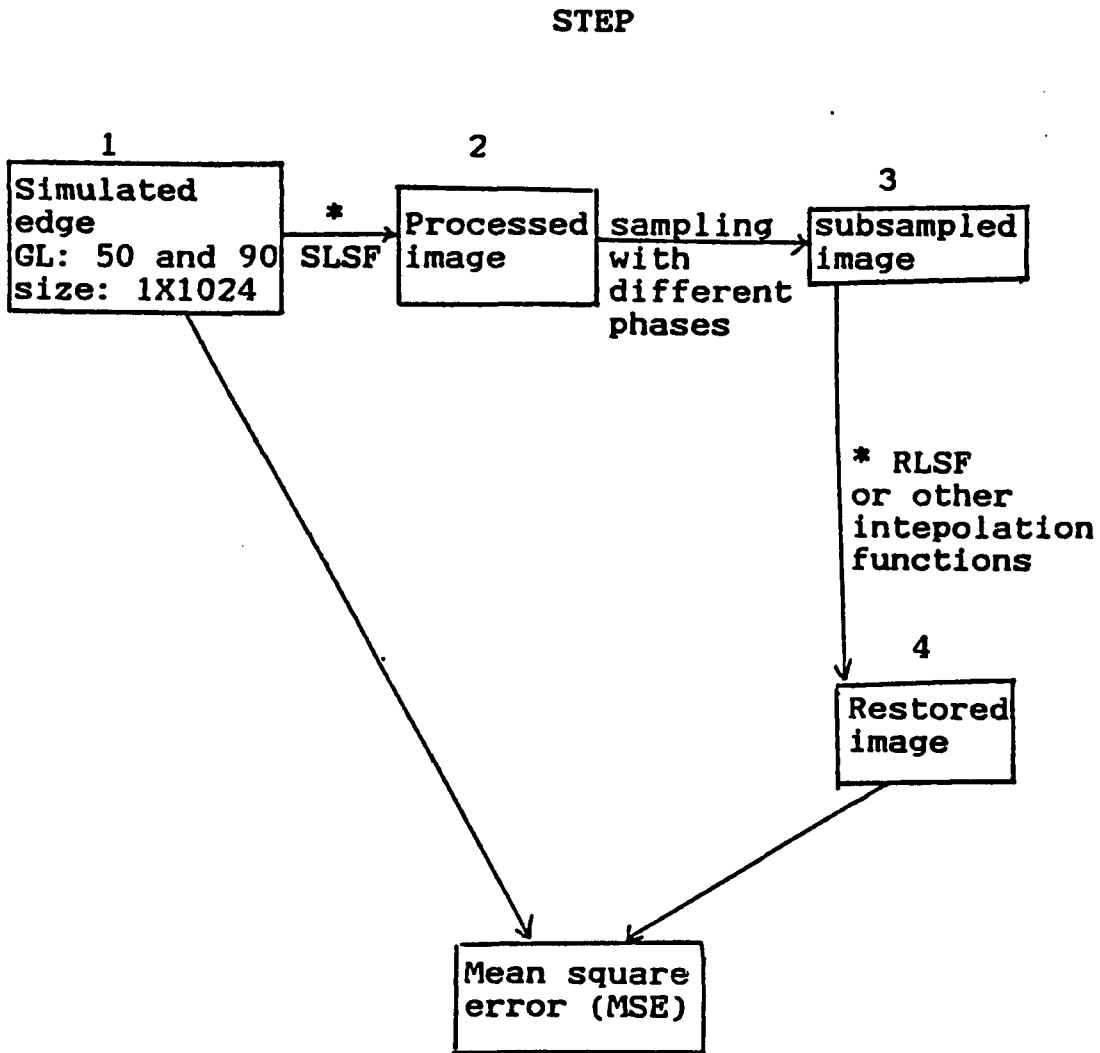


Fig.5.9. The procedures for image simulation

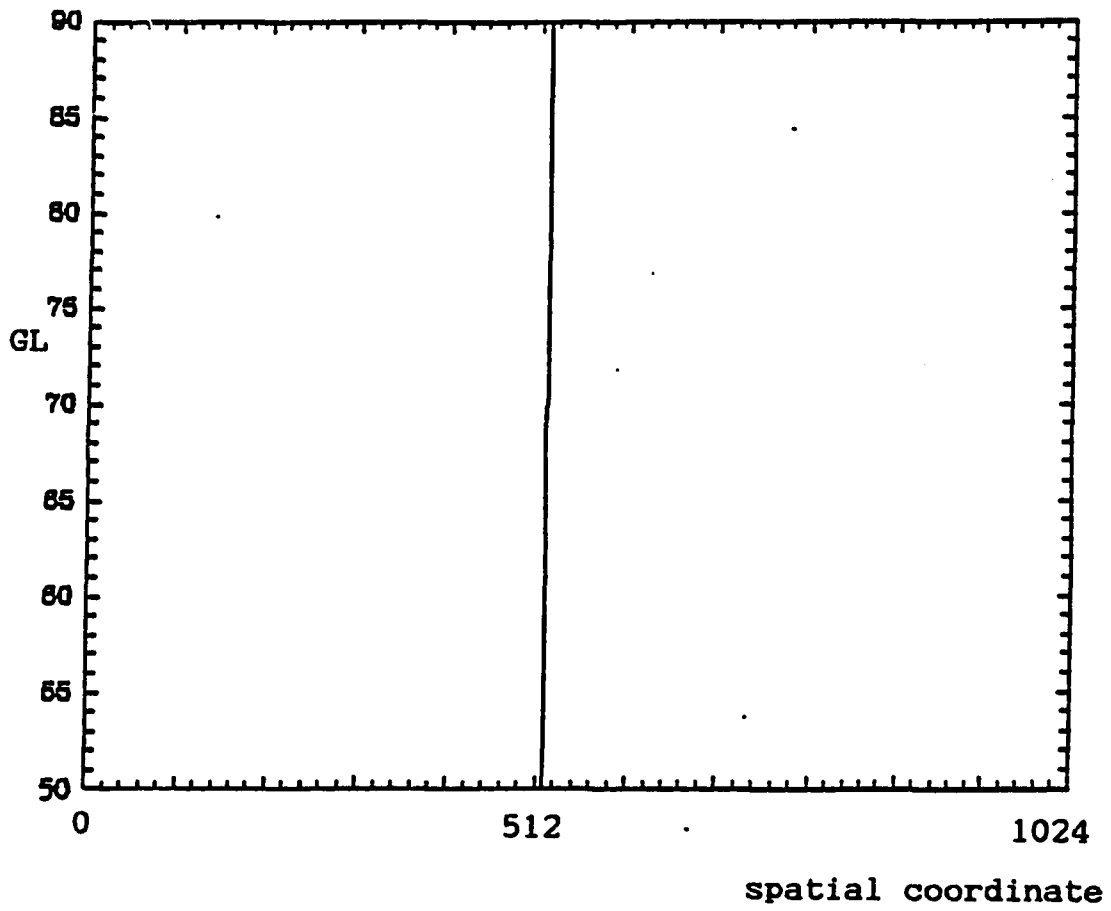


Fig.5.10 The scene with size 1x1024, edge at center

(Fig.5.11) is then convolved with the edge to produce a simulated SPOT image (Fig.5.12). Note the length of the result is reduced, because the data at the two ends are affected by the convolution border effect.

Thus far, the processed image is still a continuous function in the sense explained above. It approximates the optical SPOT image projected on the detectors. The image is then subsampled by a factor of four. In other words, the processed image is sampled at every fourth point. This image approximates the digital SPOT image. Note it is different for different locations, i.e. phases, between the sampled pixels and the original edge.

Resampling is done by applying an interpolation or restoration function to the digital image to interpolate the points between each pixel. The interpolation functions may be used to remove geometric distortion (Fig.5.13). Currently, the bicubic or bilinear functions are commonly used for interpolation (Schowengerdt, 1983) (Fig.5.14). The resampled edge image using the bicubic as the interpolation function, for one particular sample-scene phase is shown in Fig.5.15.

In order to see how the resampled image deviates from the original image, the mean square error between them is found. Due to the phase of the pixel sampling (Step 3,

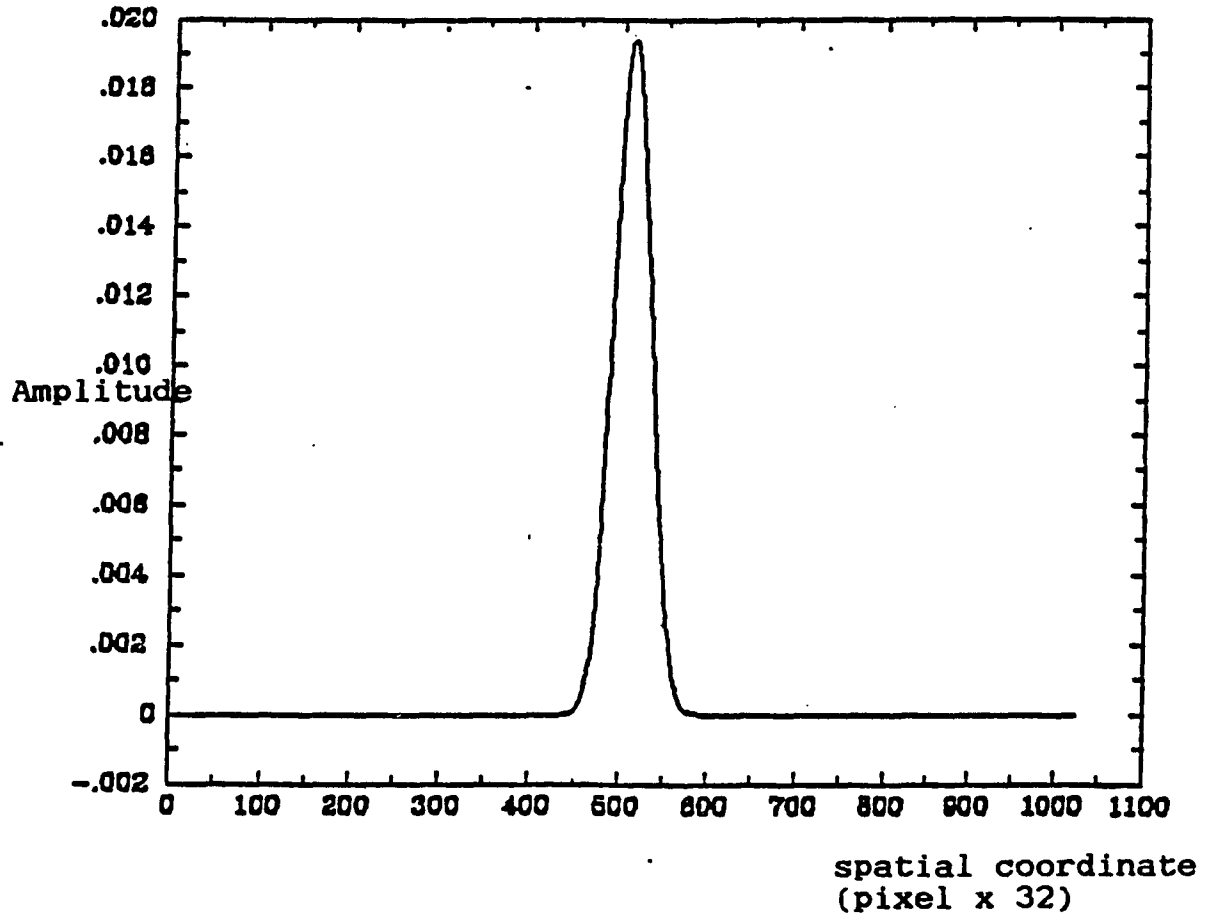


Fig.5.11: The SLSF (Pan, along-track direction)

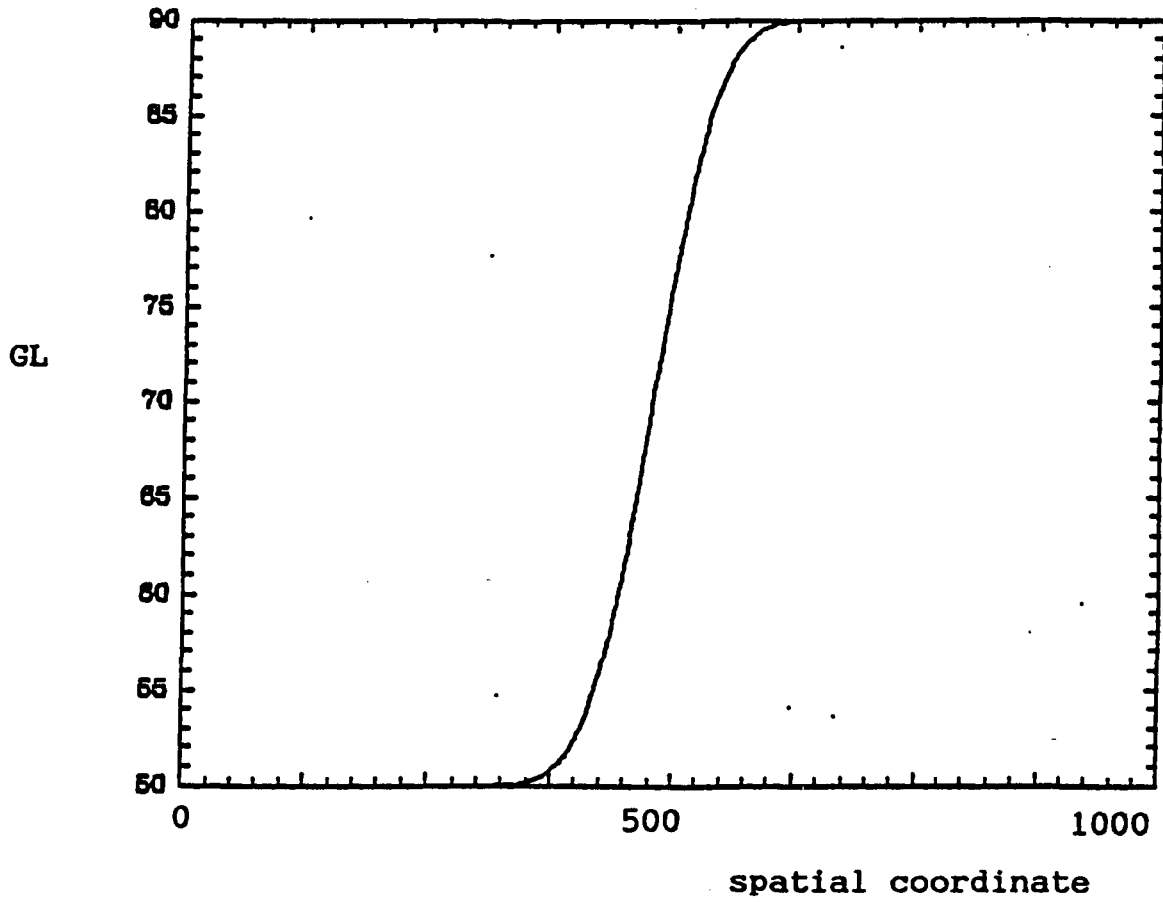


Fig.5.12 The processed image with size 1X896

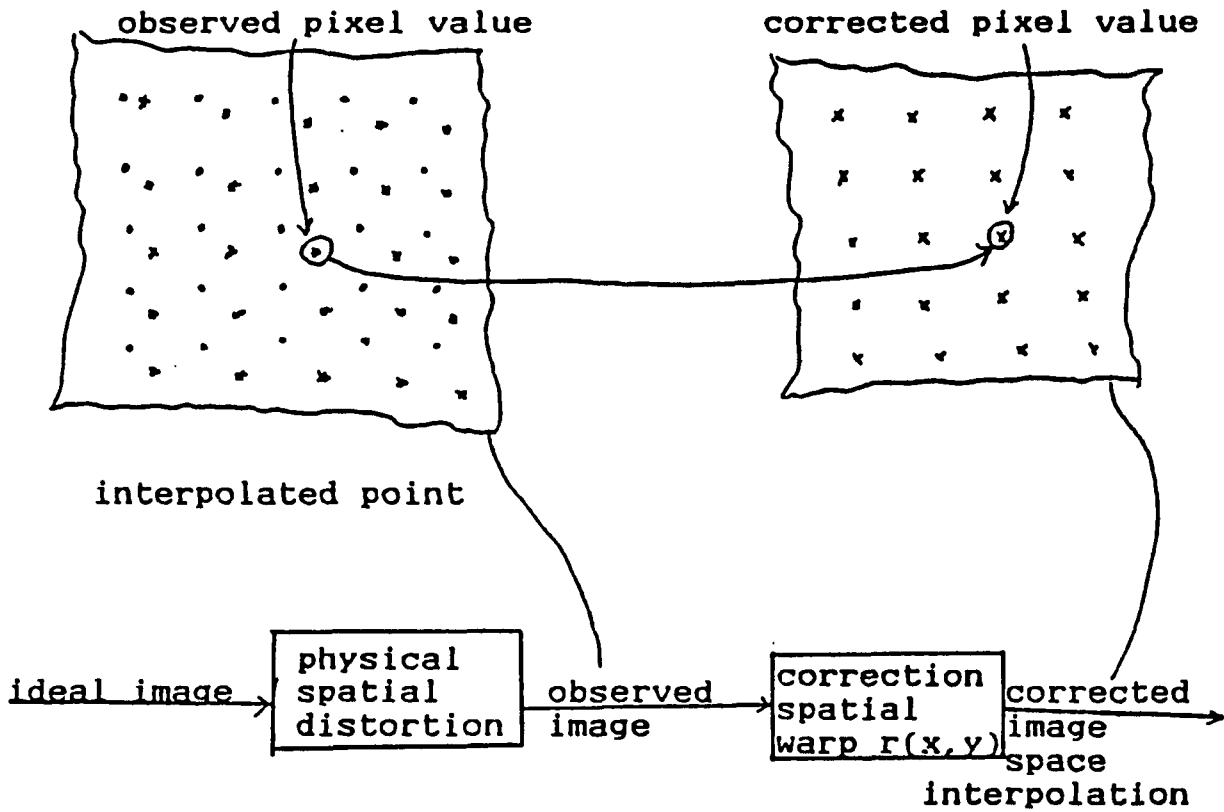


Fig.5.13 The correction of a distorted image by an interpolation function $r(x,y)$

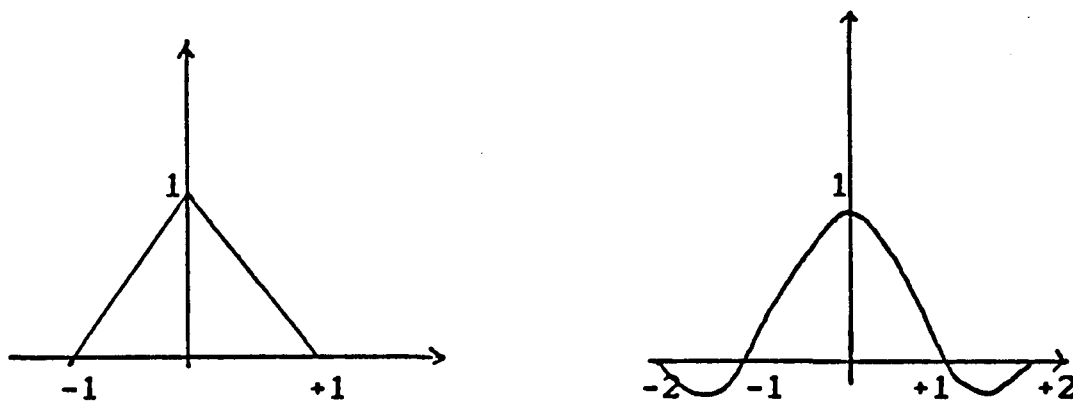


Fig.5.14 Functions of (a) bilinear and (b) bicubic resampling

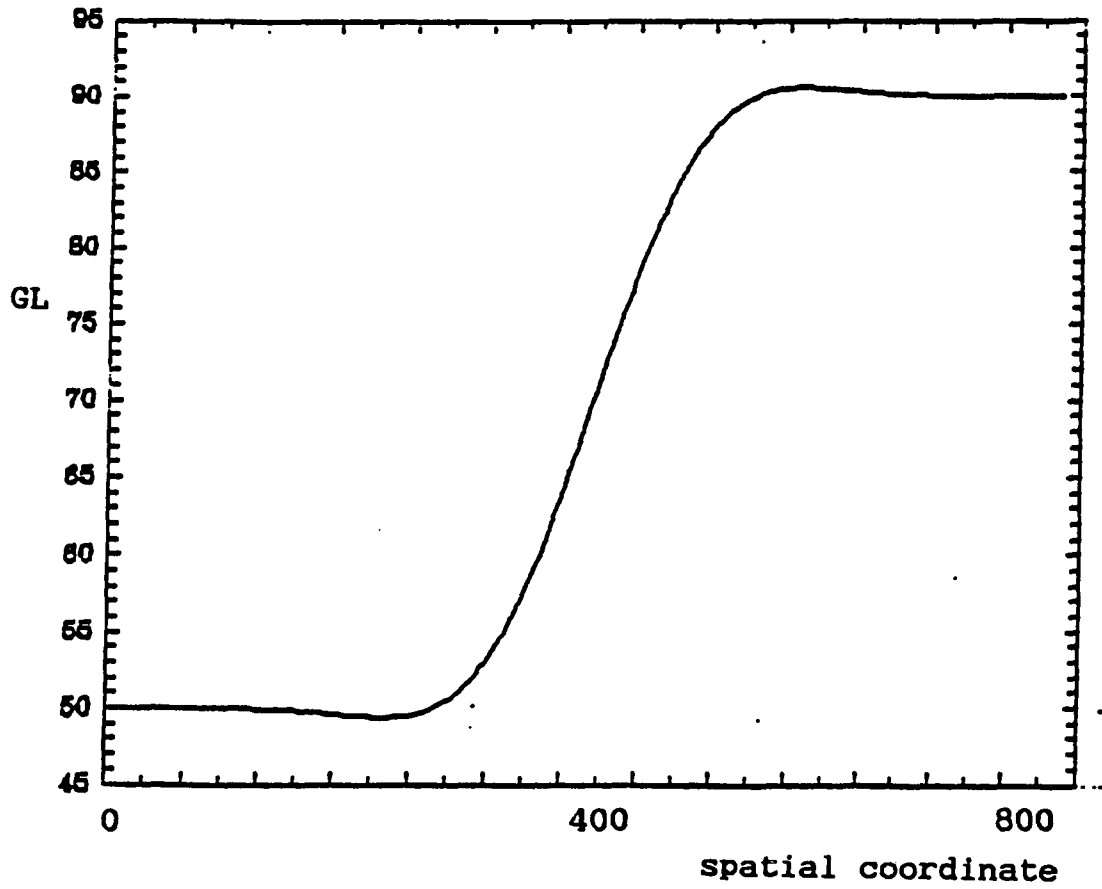


Fig.5.15 The resampled edge by using the resampling function PCC ($\alpha = -1$)

Fig.5.9) the resampled image has a phase shift with respect to the original image. Therefore, the MSE should account for this shift. In our case, a mean value of GL is defined, at 70. In the resampled image, we locate the point which gives us the value closest to 70, and compare this location to the center of the original 512 image to obtain a shift value. This shift value ranges from 2 to 33 in our testing. After adjusting the restored image to align with the original, the MSE is calculated.

Fig.5.16 shows the change in MSE as a function of alpha in the parametric cubic interpolation function (Park and Schowengerdt, 1983). The family of parametric cubic equations has the following form (Park and Schowengerdt, 1983)

$$m(x) = \begin{cases} (\alpha+2)|x|^3 - (\alpha+3)|x|^2 + 1 & |x| < 1 \\ \alpha|x|^3 - 5\alpha|x|^2 + 8\alpha|x| - 4\alpha & 1 < |x| < 2 \\ 0 & \text{otherwise} \end{cases} \quad (5.9)$$

In Fig.5.17 we have the MSE of three different interpolation functions (cubic alpha=-0.5, cubic alpha=-1. and SPOT along-track RLSF) with SPOT along-track SLSFs applied to the edge. We have the minimum MSE halfway between pixels (the 16th point) and the RLSF results in the lowest value compared to cubic resampling. Their

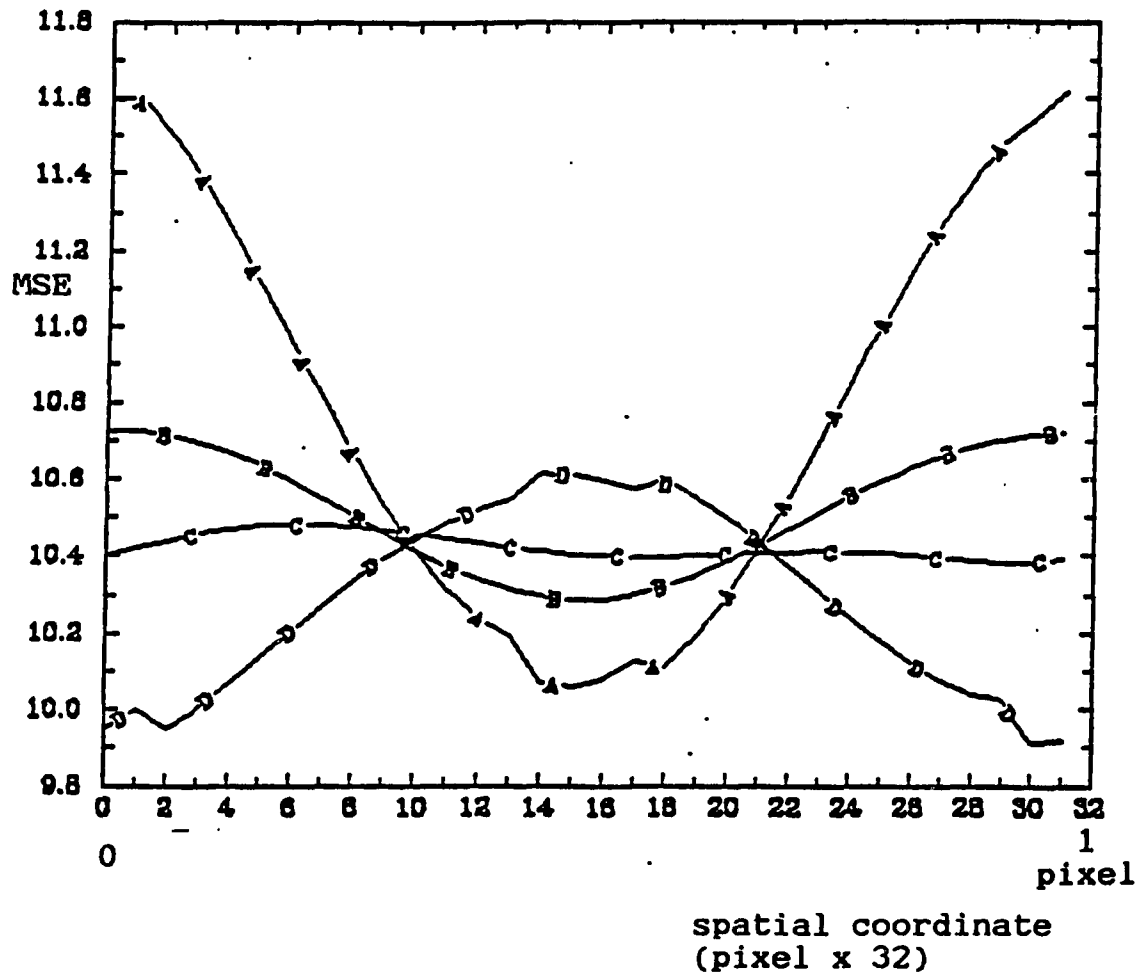


Fig.5.16. The changes of the MSE by varying alpha in PCC
 A-alpha--0.5, B-alpha--0.75, C-alpha--0.85,
 D-alpha--1.

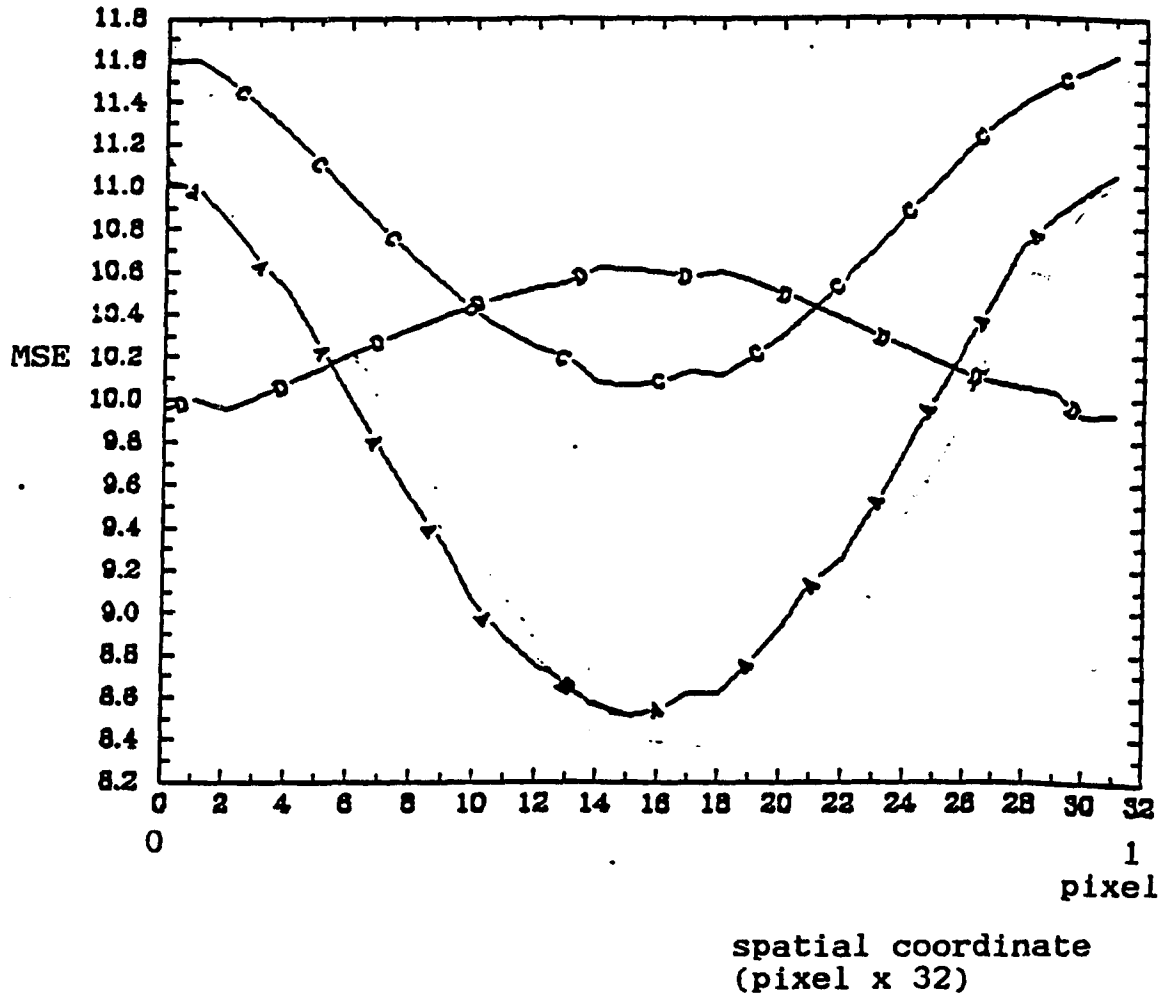


Fig.5.17. The changes the MSE by using different resampling functions
 A-Pan along-track RLSF, C-alpha--0.5, D-alpha--1.

responses to an edge are shown in Fig.5.18, done by convolution of each function with the original edge. The restoration functions (C and D) result in a sharper edge with greater GL overshoot on either side than for the cubic functions.

5.5 Image Testing

In this section, a 128X128 image is selected from the SPOT Phoenix image in the panchromatic band for testing the performance of resampling functions. In order to verify the Wiener filter used in our restoration, we employ the power spectrum (PS) of images before and after processing.

First, a 128X128 image is resampled to a 512X512 image by three interpolation functions, bicubic ($\alpha = -0.5, -1.0$) and the RLSF of the system. Second, four 128X128 images are produced by subsampling the 512X512 resampled image at every fourth point. The subsampling phase is different in each of these four subsampled images. In the restoration processing, a border effect is inevitable. Hence, if the PS is calculated for these four subsampled images, those pixels on the borders should be avoided. Three experiments were done with the PS of these subsampled images.

First, we divided the PS of the restored image, which

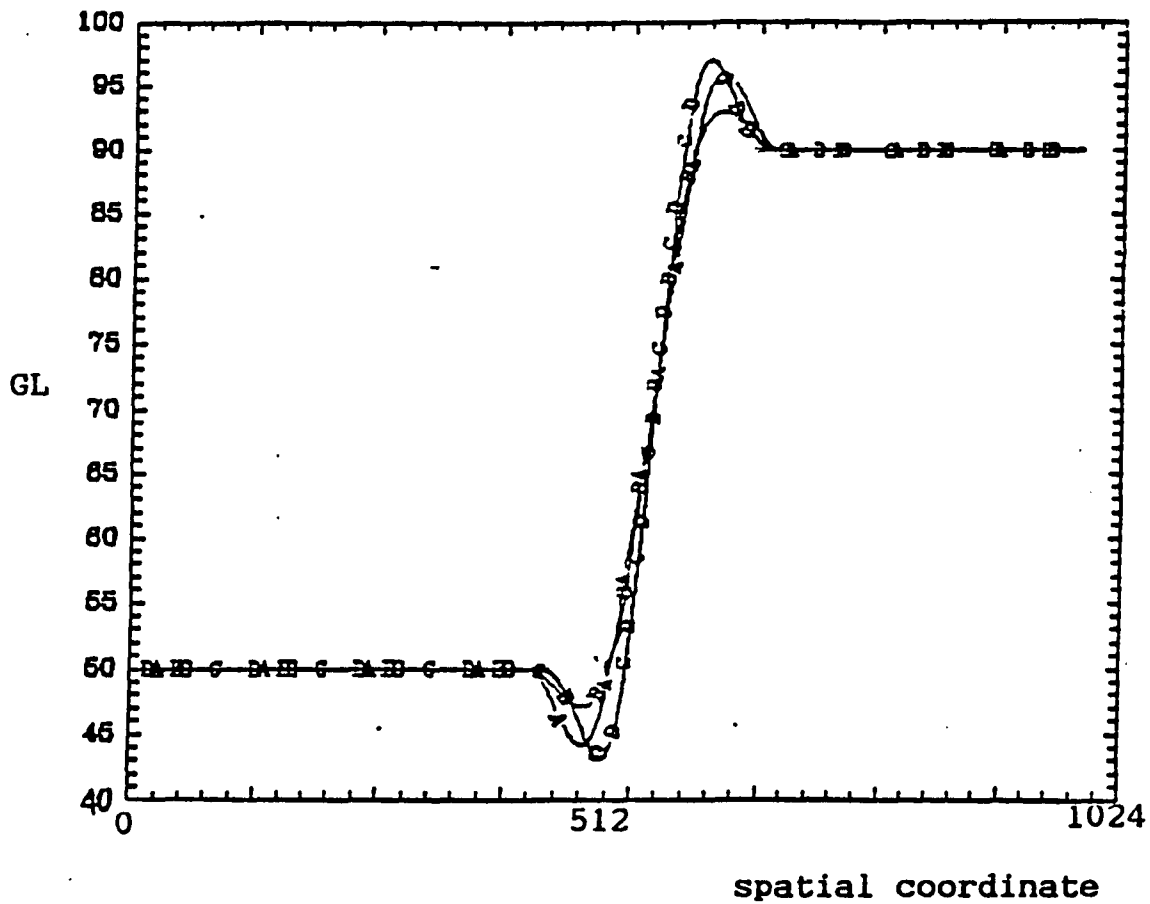


Fig.5.18 The edge responses of different resampling functions
 A- $\alpha=-1$, B- $\alpha=-0.5$, C-Pan across-track RLSF, D-Pan along-track direction

is resampled by the RLSF, by the PS of the original image. Second, the PS of the restored image at mid-pixel phase (0.5) is divided by the PS of the restored image at zero phase. Third, the PS of the restored image at mid-pixel phase was divided by the PS of the resampled by PCC ($\alpha = -1$) at mid-pixel phase. Because the division of the PS results in the square of an effective TF, the square root of each ratio is calculated.

The PS can be interpreted in two methods. First, we display the PS of the first experiment on screen and inspect its brightness (Fig.5.19). If we will see the brightness from center to the lower right corner, it goes up from the center and drops down around the corner. It looks like the Wiener filter TF. The brightness level is shown at the bottom of Fig.5.19. Second, a program was used to find the PS average over out to a radius 0.5 cycle/pixel (Fig.5.20 to Fig.5.22). These results show us that the first case is like an inverse filter TF, which means the RLSF enhances high frequencies in the image. In other words, the RLSF gives a higher contrast image for visual inspection. The second case is a low pass TF, therefore, the RLSF enhancement is less between pixels than at the pixels. Lastly, the third case is a high boost TF. It shows that the RLSF provides more

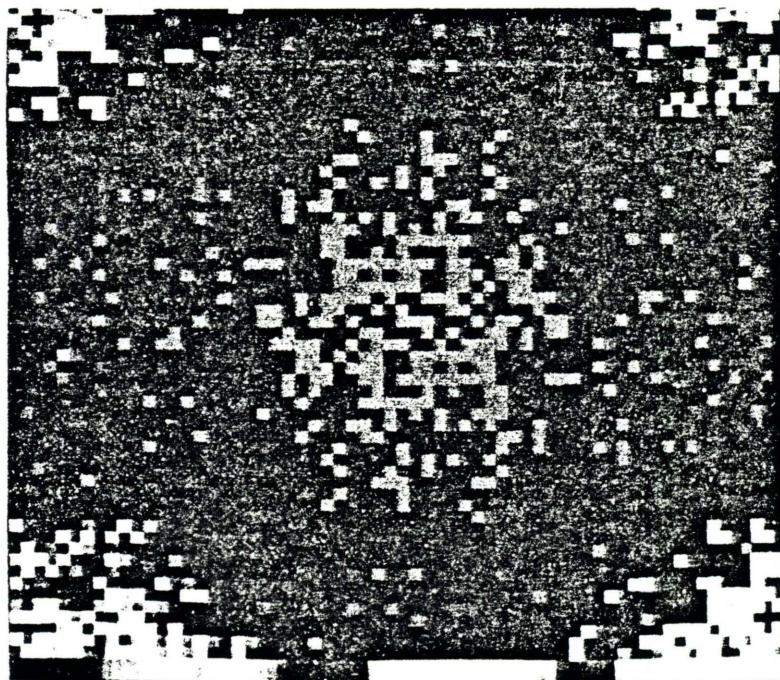


Fig.5.19 Display the first case result .

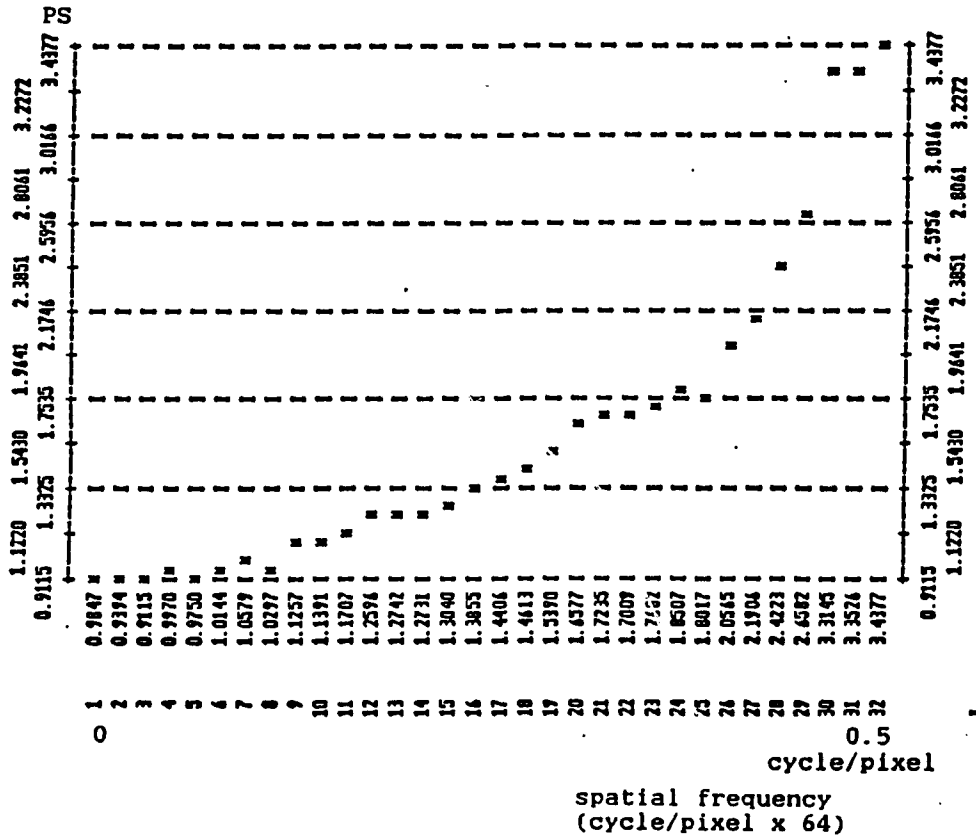


Fig.5.20. The result from the first case is averaged within 0.5 cycle/pixel

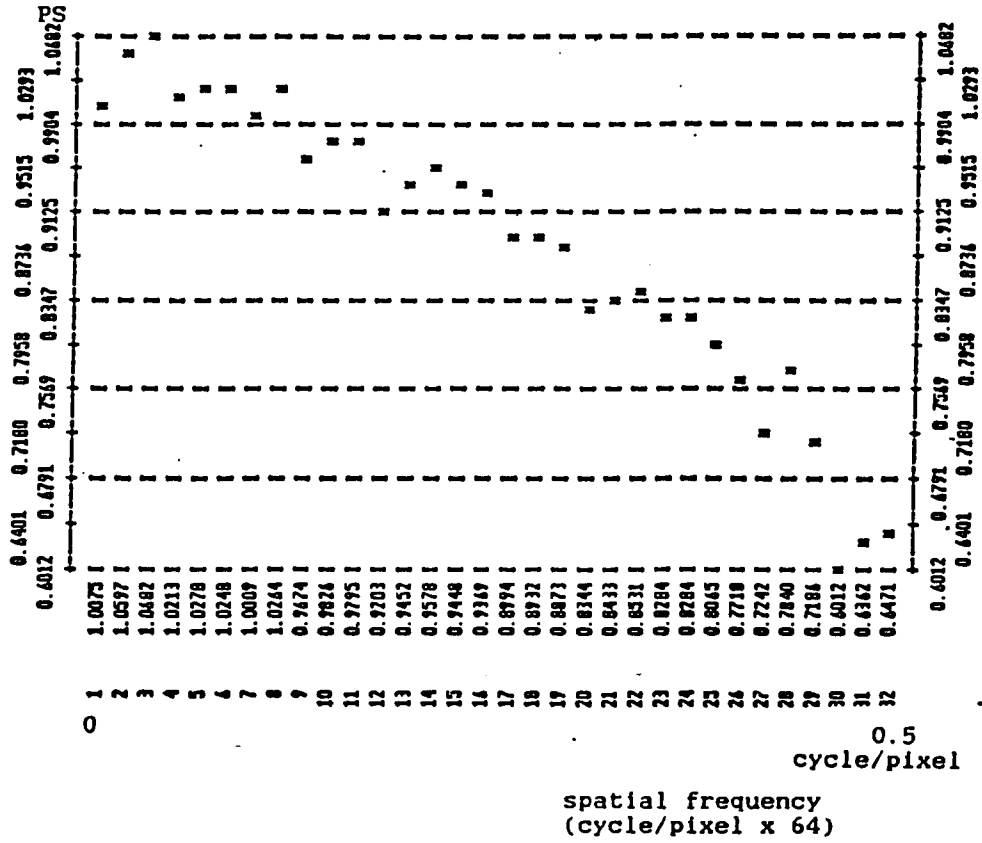
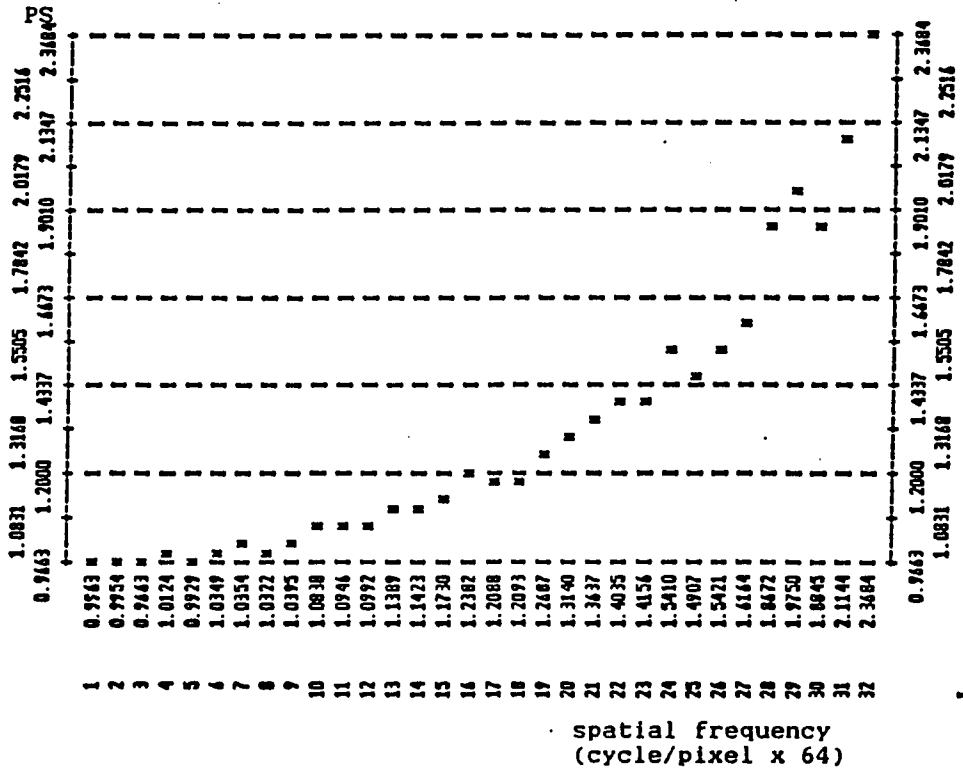


Fig.5.21 The result from the second case is averaged within 0.5 cycle/pixel



enhancement than PCC does. This verifies RLSF has a better performance in image enhancement in our system than other resampling functions.

Chapter 6

SUMMARY AND CONCLUSIONS

In the previous chapters, SPOT system and restoration models, as well as several tests on parameters in the restoration TF, have been described. We started modeling the system by using the data from Leroy (1987) to obtain the optics, IFOV, IT, and CCD TFs. Similar components exist in the Landsat (MSS, TM) and AVHRR satellite imaging systems. However, in the SPOT system, the CCD is a new type of electronic component and the integration time (IT) is a significant factor in the along-track direction.

The CCD TF has a special characteristic that can be differentiated from other systems' electronic filter TFs. Its modulus function is high in amplitude and periodic in 1 cycle/pixel. In addition, its phase function is likely to be linear. Even though the CCD TF has an uncommonly high TF, it is counteracted by the relatively low optics TF. In comparison with the system TF of whiskbroom systems in the across-track direction, we see that the SPOT system TF is the highest because of its high CCD TF (Fig.3.21). On the hand, if the overall system TF from each system is compared in the along-track direction, the

SPOT system TF is the lowest, because the integration time (IT) blurs the overall system TF.

The sampling effect is included in our model, which is done by averaging the overall system TF for all sample-scene phases from zero to one cycle/pixel. This results in a lower overall system TF. The averaged system TF is then used in the Wiener filter TF to obtain a restoration line spread function (RLSF). However, there are parameters in the Wiener filter TF that should also be determined. For instance, the half-width (HW) of the scene autocorrelation function and the variance of the scene must be found.

In order to see how changes in HW and variance affect the Wiener filter TF, we varied the HW and variance progressively. Increasing the variance results in increasing magnitude of the Wiener filter TF. If the variance increases enough, the Wiener filter acts like an inverse filter. Contrarily, increasing the HW of the autocorrelation function leads to a lower Wiener filter TF. Besides these two tests, we also included the edge image simulation, window type and size selection and verification of restoration TF by inspection of the image power spectrum (PS).

The edge image simulation showed how the sampling

phase affects the restored image. First of all, we create a 1×1024 image with an edge located at point 512. A system line spread function (SLSF) was applied on the edge scene to obtain a blurred image, which was then subsampled to every fourth point at different phases. After that, a resampling or interpolation function was applied to each subsampled image to enlarge it by a factor of four. Finally, a mean square error (MSE) was found between the resampled images and the original scene at each phase. It turns out that the lowest MSE is at the middle phase of sampling.

Before deriving the restoration line spread function (RLSF), a window function is applied to the RLSF. The window is used to soften the abrupt drop of the Wiener filter TF, and thereby eliminate oscillations (Gibb's phenomenon) in the spatial domain. In order to keep most of the information in the restored image unchanged, we have a criterion to select the windowing function and its size, namely to keep most power below 0.5 cycle/pixel and minimize power above 0.5 cycle/pixel. The Hanning window with kernel size of six pixels was selected.

Lastly, a SPOT image was used to test the Wiener filter after windowing and compare the performance of different interpolation or resampling functions at

different sampling phases. We first enlarged the scene by a factor of four by applying the SPOT RLSF or other interpolation functions. The enlarged image was then sampled at every fourth point in different phases and the PS calculated. We studied three cases. First, the PS of the restored image at phase zero (no shift from original) is divided by the PS of the original scene. The result should be the square of the Wiener filter TF with windowing. Second, the PS of the restored image at phase two (one half pixel shift) is divided by the PS of the restored image at phase zero. Third, the PS of the restored image at phase two is divided by the PS of the resampled image (PCC with $\alpha = -1$). These results showed us that the second case is a low pass TF and the third case is a high boost TF.

APPENDIX A

MTF and PTF DERIVATIONS OF CCD
IN FREQUENCY DOMAIN

Eqn.(2.7) to Eqn.(2.9) and Eqn.(2.10) to Eqn.(2.11)
can be derived in the following steps.

$$\begin{aligned}
 \text{EXP}(iw) &= \text{AEXP}(ik) + E \\
 &= \text{AEXP}(ik)[1 + (E/A)\text{EXP}(-ik)] && \text{set } E/A = B \\
 &= \text{EXP}(\ln A + ik)\text{EXP}(-ik)[\text{EXP}(ik) + B] \\
 &= \text{EXP}(\ln A + ik)\text{EXP}(-ik)(B + \text{COS}k + i\text{SIN}k) \\
 &= \text{EXP}(\ln A + ik)\text{EXP}(-ik)\text{REXP}(ic)
 \end{aligned}$$

set $B + \text{COS}k + i\text{SIN}k$ to polar form

$$\begin{aligned}
 R &= [(B + \text{COS}k)^2 + \text{SIN}^2 k]^{1/2} = [1 + B^2 + 2B\text{COS}k]^{1/2} \\
 c &= \tan^{-1}[\text{SIN}k / (B + \text{COS}k)]
 \end{aligned}$$

$$\begin{aligned}
 \text{EXP}(iw) &= \text{EXP}(\ln A + ik + \ln R)\text{EXP}(i(c - k)) \\
 &= \text{EXP}(\ln A + ik + 1/2 \ln(1 + B^2 + 2B\text{COS}k))\text{EXP}(i(c - k))
 \end{aligned}$$

$$\begin{aligned}
 iw &= \ln A + ik + 1/2 \ln(1 + B^2 + 2B\text{COS}k) \\
 &\quad - i(\tan^{-1}(\text{SIN}k / (B + \text{COS}k)))
 \end{aligned}$$

because $k - c = \tan^{-1}(\text{SIN}k / (\text{COS}k + B))$ using the identity

$$k = \tan^{-1}(\text{SIN}k / (B + \text{COS}k)) + \tan^{-1}(\text{SIN}k / (B^{-1} + \text{COS}k))$$

$$\begin{aligned}
 w &= (k - \tan^{-1}(\text{SIN}k / (B^{-1} + \text{COS}k))) \\
 &\quad - i[\ln A + 1/2 \ln(1 + B^2 + 2B\text{COS}k)]
 \end{aligned}$$

if $B \rightarrow 0$

$$w \rightarrow k - \tan^{-1}(B\text{SIN}k) - i[\ln A + 1/2 \ln(1 + 2B\text{COS}k)]$$

$$= k - \tan(BSINk) - i[\ln A + 1/2(2BCOSk - 4B^2COS^2k + \dots)]$$

$$\ln(1+x) = x - x^2/2 + x^3/3 - \dots \quad \text{provided that } x \text{ is small}$$

$$w = k - \tan(BSINk) - i(\ln A + BCOSk)$$

$$\tan^4(BSINk) \rightarrow BSINk$$

$$\rightarrow k - BSINk - i[\ln A + BCOSk] \quad \text{if } E, L \rightarrow 0, A \rightarrow 1$$

$$\rightarrow k - ESINk - i[\ln(1-E-L) + ECOSk]$$

$$= k - ESINk - i[-E-L + ECOSk]$$

$$= k - ESINk + i[L + E(1-COSk)]$$

$$= k - ESINk + iE(1-COSk)$$

$$k = 2\pi f / fc \quad |Rek| < \pi \quad \Rightarrow |f| < fc/2$$

APPENDIX B

MTF AND PTF DERIVATIONS OF CCD
IN SPATIAL DOMAIN

To obtain eqn.(2.11) from eqn.(2.14), it is derived in the following steps.

$$\begin{aligned}
 & [(1-pA)/(1-pA\text{EXP}(-iwTc))]^n \text{EXP}(-iwTcn) \quad wTc=2 f/fc=V \\
 & \quad pA = E \quad \text{and} \quad \text{if } B = 0 \\
 & = [(1-E)/(1-E\text{EXP}(-iV))]^n \text{EXP}(-iVn) \\
 & = [(1-E)/(1-E(\text{COSV}-i\text{SINV}))]^n \text{EXP}(-iVn) \\
 & = [(1-E)/(1-ECOSV+Ei\text{SINV})]^n \text{EXP}(-iVn) \\
 & \quad \text{set } (1-ECOSV+Ei\text{SINV}) \text{ in polar form } (R,c) \\
 & = (1-E)^n * R^n \text{EXP}(-inc) \text{EXP}(-iVn) \\
 & = [(1-E)/R]^n \text{EXP}(-in(c+V)) \\
 & = [(1-2E+E^2)/(1+E^2-2ECOSV)]^{n/2} \text{EXP}(-in(c+V)) \\
 & = \text{EXP}[n/2\ln((1-2E+E^2)/(1+E^2-2ECOSV))] \text{EXP}(-in(c+V)) \\
 & \rightarrow \text{EXP}[n/2\ln((1-2E)/(1-2ECOSV))] \text{EXP}(-in(c+V)) \\
 & = \text{EXP}(n/2\ln(1-2E)-n/2\ln(1-2ECOSV)) \text{EXP}(-in(V+ \\
 & \quad \tan^{-1}(E\text{SINV}))) \\
 & \text{because } c = \tan^{-1}(E*\text{SINV}/(1-ECOSV)) \text{ as } E \rightarrow 0 \\
 & \quad c \sim \tan^{-1}(\text{SINV}/(1/E-\text{COSV})) \sim \tan^{-1}(E\text{SINV}) \\
 & \quad \text{if } E \rightarrow 0 \\
 & = \text{EXP}(n/2(-2E)-n/2(-2ECOSV)) \text{EXP}(-in(V+E\text{SINV})) \\
 & = \text{EXP}-(nE-nECOSV) \text{EXP}(-in(V+E\text{SINV}))
 \end{aligned}$$

$$= \text{EXP}(-nE(1-\text{COSV}))\text{EXP}(-in(V+\text{ESINV}))$$

REFERENCES

- Andrews, H.C., "Digital image restoration: A survey", IEEE computer, Vol.7, pp.36-45 (1974).
- Andrews, H.C., A.G. Tescher and R.P. Kruger, "Image processing by digital computer", IEEE spectrum, pp.20-32 (1972).
- Barbe, D.F., "Advanced infrared focal plane array concepts", Electro-optical systems design, pp.50-57 (1977).
- Berglund, C.N., "Analog performance limitations of charge-transfer dynamic shift registers", IEEE journal of solid-state circuits, Vol. sc-6, No.6, pp.391-395 (1971).
- Cannon, T.M., H.J. Trusell and B.R. Hunt, "Comparison of image restoration methods", Applied optics, Vol.17, No.21 (1978).
- Courtois, M. and G. Weill, "The SPOT satellite system", Vol.97 of progress in Astronautics and Aeronautics series (1987).
- Forman, M.L., "Spectral interpolation: zero fill or convolution", Applied optics, Vol.16, No.11 (1977).
- Frieden, B.R., "Optical transfer of the three-dimensional object", Optical sciences technical report 13, U.A. (1967).
- Frieden, B.R., "Maximum attainable MTF for rotationally symmetric lens systems", Optical sciences technical report 29, U.A. (1968).
- Frieden, B.R., "A Fourier theory of statistical image formation", Optical sciences technical report 22, U.A. (1968).

Frieden, B.R., "Optimum, non-linear processing on noisy images", Optical sciences technical report 23, U.A. (1968).

Harris, F.J., "On the use of windows for harmonic analysis with the discrete Fourier transform", Proceeding of the IEEE, Vol.66, No.1 (1978).

Huck, F.O., C.L. Fales, N. Halyo, R.W. Samms and K. Stacy, "Image gathering and processing: information and fidelity", J. optics. Soc. Am. A, Vol.2, No.10 (1985).

Hummel, R.A. and B. Kimia and S.W. Zucker, "Deblurring Gaussian blur", Computer vision, graphics, and image processing, No.38, pp.66-80 (1987).

Hunt, B.R. and H.C. Andrews, "Digital image restoration", Prentice-Hall, Inc. (1977).

Hunt, B.R., "Nonstationary statistical image models and their application to image data compression", Computer graphics and image processing, 12, pp.173-186 (1980).

Johnson, J.E., H.M. Blur and F.J. Janza, "Manual of remote sensing volume 1", American society of photogrammetry, Falls church, Virginia (1975).

Joyce, W.B. and W.J. Bertram, "Linearized dispersion relation and Green's function for discrete-charge-transfer devices with incomplete transfer", American telephone and telegraph company, Bell system technical journal, Vol.50, No.6 (1971).

Kesler, M.P. and T.S. Lomheim, "Spectral response nonuniformity analysis of charge-coupled imagers", Applied optics, Vol.25, No.20 (1986).

King, D., "The new generation of image sensors", Photonics spectra, pp.119-124 (1987).

Leroy, M., G.Begni and M.Dinguirard, "SPOT radiometric resolution performance evaluation: Preliminary results" (1987).

Mord, A.J., N.H. Endsley, E. Ramberg and H.J. Reitsema, "Electronic image alignment: implementation and applications to imaging system design", Optical engineering, Vol.24, No.3 (1985).

Norwood, V.T., "Balance between resolution and signal-to-noise ratio in scanner design for earth resources systems", Proceedings of the society of photo-optical instrumentation engineers, Vol.51, pp.37-42 (1974).

Oppenheim, A.V., "The importance of phase in signals", Proceedings of the IEEE, Vol.69, No.5 (1981).

Orfanidis, S., "Optimum signal processing and introduction", Macmillan publishing company (1985).

Papoulis, A., "Probability, random variables, and stochastic processes", McGraw-Hill book company (1984).

Pratt, W.K., "Digital image processing", A Wiley-interscience publication (1978).

Schowengerdt, R.A. and S.K. Park, "Image reconstruction by parametric cubic convolution", Computer vision, graphics, and image processing, 23, pp.258-272 (1982).

Schowengerdt, R.A. and S.K. Park, "Image sampling, reconstruction, and the effect of sample-scene phasing", Applied optics, Vol.21, pp.3142 (1982).

Schowengerdt, R.A., S.K. Park, and R. Gray, "Topics in the two dimensional sampling and reconstruction of images", International journal of remote sensing, Vol.5, No.2, pp.334-347 (1984).

Schowengerdt, R.A., S.K. Park, and M. Kaczynski, "Modulation-transfer-function analysis for sampled image systems", Applied optics, Vol.23, No.15 (1984).

Schowengerdt, R.A., "Techniques for image processing and classification in remote sensing", Academic press, Inc. (1983).

Schowengerdt, R.A. and L. Wood, "Image deconvolution/resampling capability" (1985).

Schowengerdt, R.A. and W.M. Li, "AVHRR image deconvolution/resampling capability" (1987).

Sequin, C.H. and M.F. Tompsett, "Charge transfer device", Bell telephone laboratories, Murray Hill, New Jersey (1975).

Shlien, S., "Geometric correction, registration, and resampling of Landsat imagery", Presented at the remote sensing science and technology symposium (1977).

Simard, R., "SPOT panchromatic-multispectral composite image simulation", Sixteenth international symposium on remote sensing of environment, Buenos Aires, Argentina (1982).

Slater, P.N. and L.R. Baker, "Earth orbital electro-optical multiband camera: image sensor report", Optical sciences center technical report 52, U.A. (1970).

Slater .P.N., "The use of MTF in the specification and first-order design of electro-optical and photographic imaging and radiometric systems", Optica Acta (4), pp.277-290 (1979).

Slater .P.N., "Remote sensing optics and optical systems", Addison-Wesley, Reading, MA (1980).

Srinivasam, R., "Image restoration techniques", Digital design (1986).

Stearns, S.D. and R.A. David, "Signal processing algorithms", Prentice-Hall, Inc. (1988).

Thunen, J.G., "Signal processing in the presence of signal-dependent noise", Optical sciences technical report 65, U.A. (1971).

Veil C., "SPOT and remote sensing applications for arid land semi-arid lands", International symposium on remote sensing of environment, First Thematic conference, Cairo, Egypt (1982).